ABSTRACT

Title of dissertation: ARCHITECTURE-ELECTRONIC PROPERTY RELATIONS ACROSS MOLECULAR SEMICONDUCTOR INTERFACES

Yinying Wei, Doctor of Philosophy, 2010

Dissertation directed by: Professor Janice E. Reutt-Robey
Department of Chemistry and Biochemistry

Multicomponent organic films have increasing applications in photovoltaic technologies and other electronic devices. These applications depend strongly on the structural and electronic properties of the heterojunctions. This thesis reports a detailed investigation of these important aspects, such as structure control and structural-electronic correlation in molecular film heterojunctions, for two selected "donor-acceptor" model systems (TiOPc-C_{60} and TiOPc-C_{70}) using STM/STS.

The UHV-STM studies were started on a single component system, TiOPc deposited on Ag(111). Along with increasing deposition flux, TiOPc selectively forms three distinct ordered monolayer structures, namely honeycomb phase, hexagonal phase, and a misfit dislocation triangular network. Localized electrostatic intermolecular interactions can be utilized to stabilize kinetically accessible structures and cause different phase structures formed on surface. Molecular packing models for these phases are proposed based on STM measurements.

By choosing different TiOPc monolayer phases as template for sequential C_{60} deposition, low-dimensional monolayer TiOPc-C_{60} interfaces have been prepared on Ag(111) and characterized with STM/STS. Thermally stable honeycomb and metastable hexagonal TiOPc templates rearrange upon C_{60} deposition to yield several

binary film structures in the monolayer regime. These structures include phase-segregated TiOPc and C_{60} domains and co-crystalline $TiOPc_{(2)}C_{60(1)}$ honeycomb network formed through a dynamic process balanced by intermolecular and molecular-substrate interactions. The least stable TiOPc phase, the dislocation network, turns out to be the most robust template for sequential C_{60} growth by forming nanophase-segregated TiOPc-C_{60} on the scale of 10 nm.

The variations of C_{60} energy gap across the heterointerface created by depositing C_{60} on hexagonal TiOPc are evaluated with STS. Energy level shift on TiOPc-C_{60} co-crystal domain boundary is identified. This energy shift is correlated to an electron transport barrier from donor material (TiOPc) to acceptor (C_{60}) in practical OPV cells.

C_{70}-TiOPc heterostructures are characterized and compared with those of C_{60}. C_{70} present a greater variety of molecular configurations and related properties than those of C_{60} because of the ellipsoid shape with lower symmetry and higher dipole polarizability. C_{70} deposited on TiOPc honeycomb phase shows completely different growth mode from that of C_{60}. The TiOPc honeycomb structure, functionalized as a dipole buffer layer, plays a substantial role on sequential C_{70} growth up to the fourth layer. Simple geometric effect and dipole-induced dipole interactions are considered to rationalize the intriguing C_{70} growth mode. The structural model for each layer is proposed.

By employing fullerenes (C_{60} or C_{70}) and TiOPc thin films as model system, I investigated the controlled formation of donor-acceptor molecular film architecture, measured the orientation and separation of donor-acceptor molecules along the

domain boundaries, and correlated the structural information with the electronic structural information. These systematical works shed light on the optimization of molecular electronic devices from a fundamental microscopic perspective.

ARCHITECTURE-ELECTRONIC PROPERTY RELATIONS ACROSS MOLECULAR SEMICONDUCTOR INTERFACES

by

Yinying Wei

Dissertation submitted to the Faculty of the Graduate School of the
University of Maryland, College Park in partial fulfillment
of the requirements for the degree of
Doctor of Philosophy
2010

Advisory Committee:

Professor Janice E. Reutt-Robey, Chair
Professor Theodore L. Einstein
Professor Amy Mullin
Professor Yu-Huang Wang
Professor John D. Weeks

Acknowledgements

First and foremost, I would like to thank my advisor, Prof. Janice Reutt-Robey. Her instruction, encouragement, and support during my graduate study give me great impetus to carry out my research. Her availability and willingness to discuss any problem, idea, and result are greatly appreciated. It is a pleasure to be her student.

I wish to thank my former chemistry teachers Ms. Qi Wang and Mr. Yiming Jiang for inspiring my curiosity and initiating my enthusiasm in chemistry.

I would like to thank Dr. Bill Cullen for all the helps and suggestions on maintaining my instruments and sharing his expertise on SPM measurements. I am thankful to my friends and coworkers in University of Maryland: Dr. Wei Jin, Mr. Qiang Liu, Dr. Levan Tskipuri, Dr. Veda Bharath, Ms. Qian Shao, Ms. Lifang Ma, and Mr. Wentao Song. I would also thank Ms. Kristen Burson who made the final stage of my research project possible.

I am grateful to my committee members, Prof. Amy Mullin, Prof. John Weeks, Prof. Ted Einstein, and Prof. Yu-Huang Wang, for their helps to make me finish my graduate study in University of Maryland.

I want to express thank to my silence friend Awu for its patience and bearing my punches to release my stress.

Last, but not least, I want to thank my parents, Xinguo Wei and Aifang Zhu for their understanding, support, and love through my life, my husband, Bo Xu, whose consideration, encouragement, and devotion company me all the time.

Table of Contents

List of Tables

List of Figures

Abbreviations

2-D	two dimensional
2PPES	two photon photoemission spectroscopy
3-D	three dimensional
ACA	acridine carboxylic acid
AFM	atomic force microscopy
AnCA	anthracene carboxylic acid
CuPc	copper phthalocyanine
D	Debye
DFT	density functional theory
EA	electron affinity
EFM	electrostatic force microscopy
eV	electron volts
HOMO	highest occupied molecular orbital
HOPG	highly ordered pyrolytic graphite
IP	ionization potential
IPES	inverse photoelectron spectroscopy
ITO	indium tin oxide
LDOS	local density of states
LEED	low energy electron diffraction
LUMO	lowest unoccupied molecular orbital
MFM	magnetic force microscopy
ML	monolayer
MPc	metal phthalocyanine
NN	nearest neighbor
OLED	organic light-emitting diode
OMBE	organic molecular beam epitaxy
OPV	organic photovoltaic
OTFT	organic thin film transistor
PCBM	phenyl-C_{61}-butyric acid methyl ester
QCM	quartz crystal microbalance
RT-STM	room temperature scanning tunneling microscopy
SnPc	tin phthalocyanine
SKPM	scanning kelvin probe microscopy
STM	scanning tunneling microscopy
STS	scanning tunneling spectroscopy
TiOPc	titanyl phthalocyanine
TPD	temperature programmed desorption
Trans-BCaTBPP	15-bis(4-carboxyphenyl)-10,20-bis(3,5-di-t-butylphenyl) porphyrin
UHV	ultrahigh vacuum
UPS	ultraviolet photoemission spectroscopy
XRD	X-ray diffraction
$ZnPcCl_8$	chlorine zinc phthalocyanine

Chapter 1 Introduction

1.1 Motivation

Sustainable energy and environment are among the biggest challenges humanity faces in this century. Solar energy has long been recognized for its tremendous potential to provide a renewable source of clean, readily available energy. However, widespread introduction of photovoltaic (PV) technologies requires improvements in the efficiency-to-cost ratio of available technologies. Organic solar cells have attracted considerable interest as potential cost-efficient alternatives to conventional silicon solar cells. The best efficiency of current organic/polymeric devices[1-3] and dye-sensitized oxide nanocrystalline solar cells[4] reaches a range of 6%-10%[5-9], which is still far away from the expected up-bound of about 20%. The motivation of my research reported in this thesis is in support of next generation organic photovoltaic (OPV) materials.

The power conversion efficiency of OPV has increased a lot since the introduction of donor-acceptor heterojunctions that serve to dissociate strongly bound photo-generated excitons[5]. However, further improvements are impeded by an incomplete understanding of the electronic-morphology relationship on the nanoscale. It has become evident that the performance of the same material can exhibit a wide range of variation depending on the films' nanoscale morphology (molecular packing, domain alignment, and lateral and vertical phase separation) induced by different preparation conditions[10-12]. Organic molecular films contain a combination of ordered and disordered regions, grain boundaries, heterogeneous interfaces, localized traps, and

phase-separated domains. These features impact charge generation, transport, recombination, injection, extraction, and trapping at sub- 100 nm length scales[10,12-14].

The basic processes happening in a donor-acceptor organic heterojunction are described as following[5]:

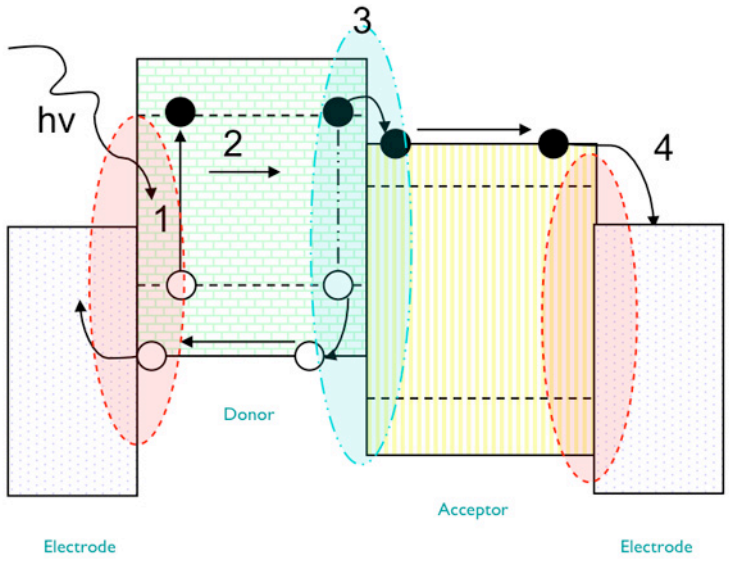

Figure 1.1 Schematic illustration of the four key steps in the generation of photocurrent from incident light in OPV cell: (1) photo absorption and exciton formation, (2) exciton diffusion to the donor-acceptor interface, (3) exciton dissociation and separation, driven by the HOMO-LUMO offset, and (4) carrier collection at the electrode.

In Step 1, the organic material absorbs light and generates excitons (electron-hole pairs), with binding energies ranging from 0.1 to 1.2 eV[15,16]. Efficient dissociation of the strongly bound excitons requires either a strong applied electric field ($E>10^6$ V/cm) or donor-acceptor heterojunctions[14], where the dissociation is driven by the offset between the HOMO and LUMO levels along the donor-acceptor interface. The photo-generated strongly bound excitons must subsequently diffuse towards the donor-acceptor interface (Step 2 in Fig. 1.1). Step 3 is exciton dissociation, taking place exclusively at the organic heterojunction and resulting in electron transfer to the

acceptor materials (and hole transfer to the donor materials). Finally, the generated free electrical carriers are transported toward the respective electrodes through organic-metal interfaces and contribute to an electrical current in the external circuit, as described in Step 4.

Several aspects are of general interest. Microscopically, the organic-organic (green shade) and organic-metal (red shade) interfaces are important for OPV working performance. Energy levels should be aligned for effective exciton dissociation, and molecular architectures on these interfaces should be optimized for charge transfer. Some orientations may be favorable for this process and some may be unfavorable (Fig. 1.2b and 1.2c, respectively). Also, it is expected to achieve maximized interfacial areas between the donor acceptor domains, as shown in Fig. 1.2a. Finally, the length (or width) of donor (acceptor) domains should be of the magnitude of the exciton diffusion length, which is 10~15 nm for molecular semiconductor excitons[5,15,17,18].

Researchers have applied a wide range of structural probes, from atomic force microscopy (AFM) to X-ray scattering, to characterize structural variations in OPV films. However, there is an urgent need for high-resolution measurements that correlate electronic properties directly with local film morphology at the molecular level. The goals of this thesis are to study the following issues at the organic-organic interface and organic-metal interface:

(1) The mechanism by which nano-phase structures form and evolve in vacuum deposited films.

(2) The molecular arrangement along donor-acceptor interfaces, and the geometric stacking that favors charge transfer.

(3) Energy level alignment along the donor-acceptor interface.

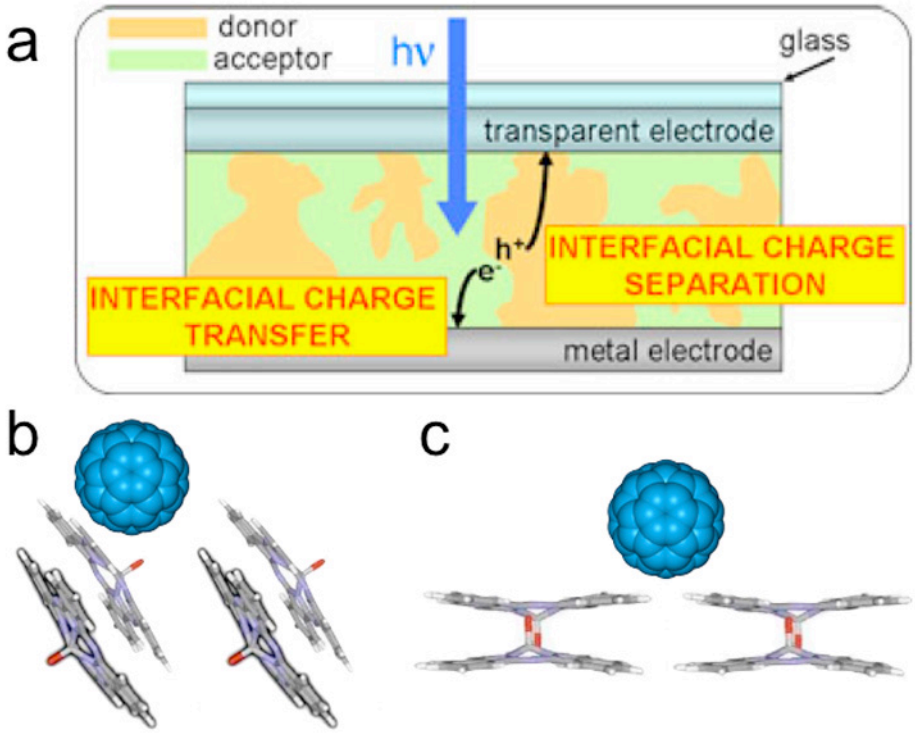

Figure 1.2 Schematic illustrations of (a) bulk heterojunctions with high donor-acceptor interfacial area for organic solar cell and (b, c) oriented molecular architectures along TiOPc/C_{60} interface.

1.2 Organic Molecular Adsorption on Solid Surface

1.2.1 Fundamental Aspects of Molecular Thin Film Growth

The process of molecular adsorption on solid surfaces is more complex than that of elemental systems due to molecular distinct shapes and anisotropic intermolecular interactions. Moreover, molecules are flexible and can undergo conformation changes when brought into contact with a substrate. In addition, polymorphism is a general phenomenon for organic bulk crystals[16]. The energy difference between different

polymorphs is usually very small compared to the cohesive energy of organic crystals. Parallel situations are present for organic molecules adsorbed on solid surface, different phase structures with similar lattice energies are usually observed for a given molecule[19,20].

Molecular self-assembly is the preparation of materials with prescribed structures based on the controlled assembly of molecular components interconnected mainly by non-covalent bonding[21]. Through this fabrication method, well-defined low dimensional structures can be formed on surfaces. Many examples of one- and two-dimensional molecular self assembly structures on substrates, with hydrogen bonding[22-29], dipole-dipole interaction[30], donor-acceptor interaction[31-34], van der Waal interaction[35,36], or even coordinative interaction[37-44], have recently been reported.

(1) Thermal dynamics vs. kinetics in adsorption

The process by which molecules deposited on substrates evolve towards nanometer scale structures is inherently a non-equilibrium phenomenon[45]. The growth process is governed by a competition between kinetic and thermodynamics control. Surface diffusion is generally considered as a thermally activated process. Thus, a diffusion barrier needs to be surmounted when the adsorbate moves from one stable adsorption site to another. Supposing molecules are deposited onto the surface at a rate of F (flux), the diffusivity D is defined as the mean square distance traveled by an adsorbate per unit time upon deposition. The ratio of D/F determines the average distance that an adsorbate has to travel to meet another adsorbate, either for nucleation of a new aggregate or attachment to a formed island. A high D/F ratio indicates quasi equilibrium growth, during which the adsorbate has enough time to

explore the potential surface to reach a minimum energy configuration. On the other hand, a low D/F ratio corresponds to a kinetically determined growth. A high D/F ratio is typically preferred in epitaxial growth as growth under slow thermodynamic control translates to long-range ordered structures. As a practical matter, low temperature experiments with low D/F ratio must be controlled to study kinetic factors as well dynamic barriers in pattern growth.

(2) Miscibility in binary system

The miscibility of two components is generally temperature dependent. For a 2-D binary molecular system, we may suppose it resembles the phase diagram of a 2-D binary liquid system. We try to understand the binary molecular structures supported on a solid surface with thermodynamic functions. The Helmholtz potential F_{sys} is a convenient thermodynamic state function to study constant T and V problems.

$$F_{sys}=U_{sys}-S_{sys}T \qquad (1.1)$$

Here S represents the total entropy of the system, and U represents the total internal energy. The competition between entropy and energy finally determines the phase structure of the binary system. Suppose we have N_a A molecules and N_b B molecules, and $N_a+N_b=N$ remains constant. We define

$$c = \frac{N_b}{N_a + N_b} \qquad (1.2)$$

as the fraction of molecule B. When F_m as a function of c has two local minima, the two molecular species will segregate into two stable phases, as shown in Fig. 1.3b.

In practice, by considering only the internal energy contributions, we can use U_m to get a sense whether the binary phase would segregate or an intermixed structure

possibly emerges. The total energy of all molecules on the surface can be represented as:

$$U_m(c) = \frac{N \times z}{2}[(1-c)^2 U_{aa} + 2c(1-c)U_{ab} + c^2 U_{bb}] \qquad (1.3)$$

Here, N is defined as the total number of molecules in the system, $N = N_a + N_b$, and z corresponds to the number of nearest neighbors. U_{aa} is the intermolecular interaction between nearest neighboring A, so does U_{bb}. U_{ab} defines the interaction between nearest neighboring A and B. Only when U_m is concave function of c (negative mixing energy, $U_{ab} < \frac{U_{aa} + U_{bb}}{2}$), F_m would have two minima, i.e. phase segregation of the two molecular species happens.

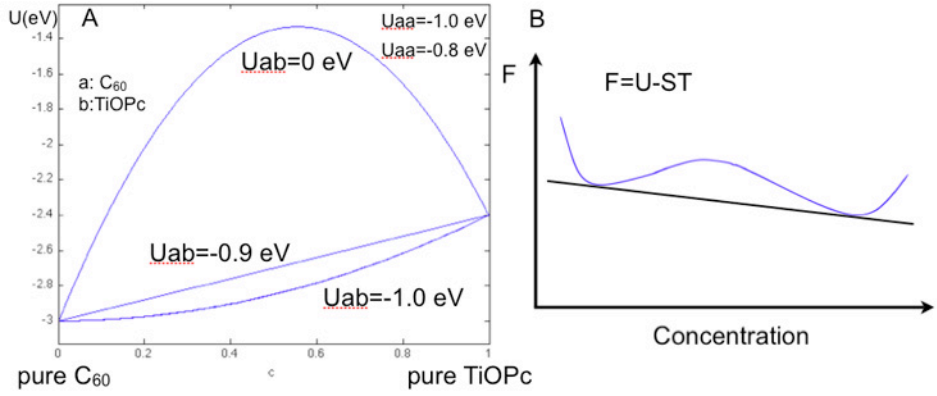

Figure 1.3 (a) The average total energy of C_{60}/TiOPc molecular system as function of concentration c (three U_{ab} values are assumed). c=0 represents pure C_{60}, and c=1 represents pure TiOPc. (b) General phase segregated diagram of total free energy of a binary system as function of c, with two local minima.

Using C_{60} and Titanyl Phthalocyanine (TiOPc) as our model system, denoting C_{60} as A and TiOPc as B, we have U_{aa}=-1.0 eV[46], U_{bb}=-0.8 eV[47], and z=6. We could then estimate the critical U_{ab} that leads to phase segregation of C_{60} and TiOPc. On one hand, if we suppose the interaction between C_{60} and TiOPc is comparable to that

between C_{60} (U_{ab}=-1.0 eV in Fig. 1.3a), we could expect a C_{60}-TiOPc intermixed phase. On the other hand, when we assume that TiOPc does not interact with C_{60}, (U_{ab}= 0 eV in Fig. 1.3a), we obtain the concave curve. C_{60} and TiOPc are expected to segregate into two stable single phases in this situation.

1.2.2 Electronic Coupling at Hetero-Interfaces

Apart from the morphology of the grown film, the interfacial electronic structures between organic/metal and constituent organic materials are important in the practical applications. The energy band alignment on the interfaces directly drives the unbinding of the excitons. The molecular packing and orientation on the interfaces have strong effects on charge transport.

When organic molecules are brought into contact with the surface of another material, the adsorption process may result in a wide variety of effects. These include polarization of the electron density of the organic material due to interaction with image charge in the substrate, orbital re-hybridization, partial charge transfer through covalent bonds, molecular reorganization by (inter) diffusion across the interface, and adsorption-induced substrate reconstructions[48,49]. The charge transfer across the interface could cause the formation of a band bending in the semiconductor and/or localized interface dipoles, as shown in Fig. 1.4. Relating the magnitude of the shift (Δ) to the electronic details presents a significant research challenge[48,49].

In the present work, the electronic structure variations of C_{60} along different domain boundaries are explored, and we try to explain the variations (transport gap and HOMO, LUMO resonance positions) with different polarization energies. We

also correlate the electronic structures across domain boundaries to local molecular packing and orientation.

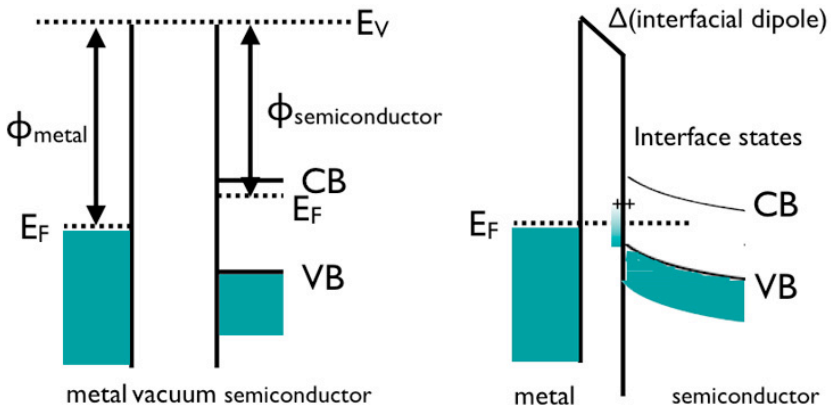

Figure 1.4 Schematic representation of the adjustment of equilibrium conditions at a semiconductor/metal interface. The charge transfer across the interface could cause the formation of a band bending in the semiconductor and/or localized interface dipoles.

1.3 Introduction to Model Systems

In this thesis work, we have selected C_{60}, C_{70}, and TiOPc as our model systems. Metal phthalocyanines (MPc) are a typical family of fully π-conjugated macrocyclic molecules with high thermal stability and versatile functionalities. Particularly, TiOPc has light sensitivity at the infrared region[50], which has applications in photoelectric conductivity. TiOPc is also applied to OPV cells as an electron donor material, and it is reported that TiOPc/C_{60} heterojunctions offer V_{OC} (open circuit voltage) 40% higher than that of CuPc/C_{60} heterojunctions[51]. For bulk heterojunction (BHJ) devices, V_{OC} should be linearly related to the frontier orbital energy offsets between the HOMO of the donor and the LUMO of the acceptor (E_{DHOMO}-E_{ALUMO})[52-56]. A limited number of studies have been undertaken to elucidate the supramolecular behavior of TiOPc molecules on surfaces[57]. In addition, their surface structural

organization with other redox or photoactive molecular species, such as fullerenes, is also of great interest.

C_{60} is a popular electron acceptor material with a tunable highest occupied molecular orbital-lowest unoccupied molecular orbital (HOMO-LUMO) gap[58,59], which makes it an appealing π-conjugated module for the construction of functional molecular materials[21].

The second most abundant fullerene, C_{70}, is less intensively studied. However, recent reports show it has a 25% higher efficiency in device performance[60,61], and stronger tendency for charge transfer with other donor type materials[39,60,61]. In addition, C_{70} possesses a greater variety of surface configurations and related properties compared with those of C_{60} because of the ellipsoid shape with lower symmetry and higher dipole polarizability. All these new findings motivate C_{70}/TiOPc heterojunctions for comparison.

1.4 Thesis Outline

The outline of this thesis is as follows. In Chapter 2, the experimental procedures and instrumentations are described. A brief introduction of the UHV system and STM used in this thesis are presented. The molecular deposition system and sample preparation procedure are introduced. In addition, the method used for computing the molecular properties is discussed.

In Chapter 3, single component adlayer structures for C_{60}, C_{70} and TiOPc are described and discussed. The chapter starts with the description of C_{60} and C_{70} superstructures formed on Ag(111). The richer single component phase diagram of the highly anisotropic TiOPc is then presented. Three completely different ordered

structures of TiOPc can be kinetically accessed by simply tuning the deposition flux. The resulting structures are described in terms of competition between intermolecular interaction and molecular-substrate interaction. The concept of critical nucleation density is explored from the perspective of energy differences.

Chapter 4 and Chapter 5 concern the mixtures of fullerenes and TiOPc. We explore C_{60} deposition onto distinct TiOPc monolayer structures, resulting in binary film morphology ranging from phase segregated domains with size dictated by the morphology (step density) of the substrate (on honeycomb phase TiOPc), to a co-crystalline $TiOPc_{(2)}C_{60(1)}$ honeycomb network (on hexagonal phase TiOPc) and nanophase-segregated TiOPc-C_{60} on the scale of 10-20 nm (on triangular dislocation network TiOPc). We also employ the TiOPc honeycomb structure as a dipole buffer layer to modify the electrostatic properties and morphology of Ag(111) substrate. C_{60} and C_{70} deposited onto this buffer layer show distinct adsorption behavior with C_{60} phase segregating with TiOPc while C_{70} vertically stacking on top of TiOPc. We attribute this divergence to different geometric structure and electrostatic polarizability of C_{60} and C_{70}.

Preliminary results on interfacial electronic structures are presented in Chapter 6. For this effort, we employ C_{60} as the probe molecule to profile the electronic landscape across domain boundaries. Energy alignment and molecular packing on the heterointerfaces are discussed.

A summary and suggestions for future work are presented in Chapter 7.

Chapter 2 Instrumental Methods and Experimental Set-up

In this chapter, experimental methods and molecular modeling approaches are described. In Section 2.1, introduction to UHV system is presented. In Section 2.2, details on the Ag(111) substrate are given. In Section 2.3 I describe the OMBE system for molecular deposition. The main instrument used during thesis research is scanning tunneling microscope (STM), as described in Section 2.4. Finally, computational methods investigating quantum molecular problems are briefly introduced in Section 2.5.

2.1 The Ultra High Vacuum Environment

Ultra high vacuum (UHV), defined as $P \leq 1 \times 10^{-9}$ torr , is indispensable in studying atomic processes on surfaces because it dramatically reduces the surface contamination. At the pressure of 10^{-10} torr, the residual gas density is so low that the mean free path at ambient pressure increases from the order of 10^{-8} m to the order of 10^{3} m[62]. The number of collisions at the sample surface is similarly reduced from 3×10^{19} $cm^{-2}s^{-1}$ to 4.2×10^{6} $cm^{-2}s^{-1}$ at ambient temperature. This enables study of processes on atomically clean surfaces during several hours or days.

The UHV multi-analysis system used for most work of this thesis consists of two individually pumped chambers that are separated by a gate-valve, as shown in Fig. 2.1. The main UHV chamber contains the tools for sample preparation, molecular deposition, and sample analysis. The loadlock has a home-build deposition source

attached, and with the fast entry port: freshly prepared substrates (e.g. vacuum deposited metal films, cleaved HOPG) are first load into the loadlock. Subsequent processes such as cleaning, film growth, and analysis (LEED, STM/STS) are preformed in-situ in the main vacuum chamber. A base pressure better than 5×10^{-10} torr in the main chamber is maintained for all characterizations in this thesis.

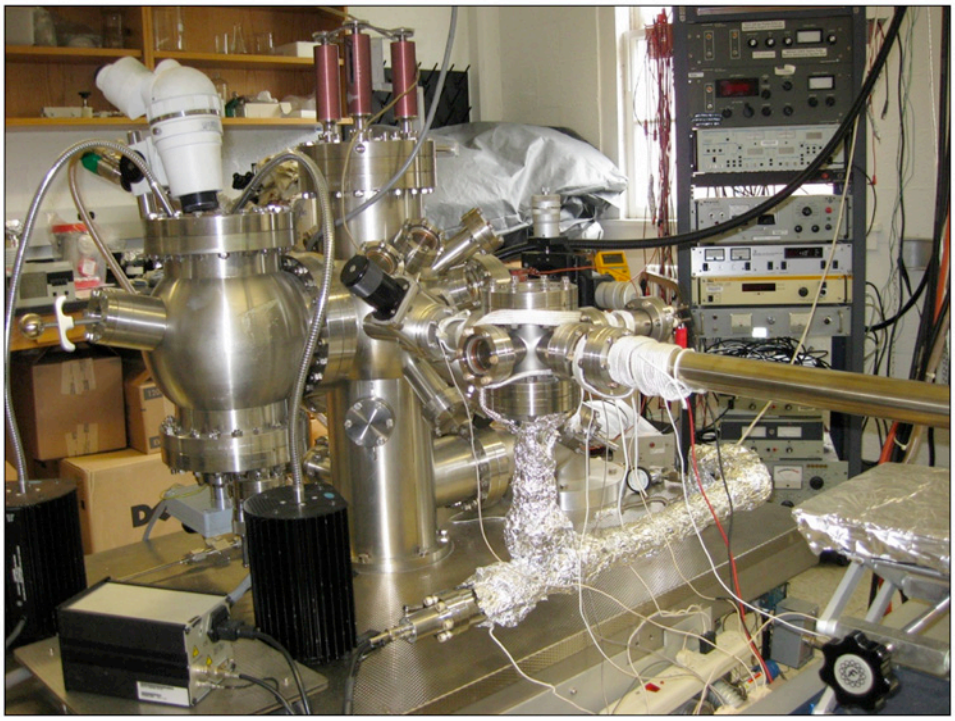

Figure 2.1 UHV multi-analysis system with fast entry loadlock used in this thesis research.

2.2 Substrate Preparation

For the investigations in this thesis, crystalline, atomically clean substrates serve as supports for the molecular layers. These include oriented single crystals and single crystalline films prepared with physical vapor deposition. Ag(111) films are employed for the thesis study. The reasons silver was chosen are the following:

1. Silver is one of the popular electrode materials in practical use,

2. Ag(111) is a surface of low reactivity, thus allowing a moderate adsorbate-substrate interaction,

3. Procedures for the preparation of single crystalline Ag(111) films are well established[63,64].

The Ag(111) films (surface lattice constant a=0.289 nm) were grown hetero-epitaxially on air-cleaved mica (SPI, V4 grade) substrates. The mica was first annealed at 600K for 2 hours at a vacuum of $P<5\times10^{-6}$ torr. The mica temperature was then increased to 650K, when Ag deposition was performed. Ag was evaporated from a homemade tantalum crucible filled with Ag shots. The typical deposition rate is 10 nm/s, as monitored from a nearby quartz crystal microbalance (QCM). Ag films with the thickness of up to 500 nm prepared in this method are found to be single crystal with (111) orientation.

The Ag/mica substrates were transferred into UHV chamber for additional preparing. After several cycles of Argon ion sputtering (30 minutes, 1000 V, 10 mA) and subsequently annealed to 760 K, large step free Ag (111) terraces with typical terrace widths over 100 nm were obtained. The resulting surface was then characterized by STM and low energy electron diffraction (LEED). Sharp (111) diffraction features, indicative of a single crystalline film, are shown in Fig. 2.2a. STM images reveal (111) terraces separated by monatomic steps (Fig. 2.2b). The irregular step structures are resulted from the relative low (<800K) sample annealing temperature, which is sufficient to fully equilibrate the surface structure. Higher annealing temperature would lead to dewetting of the Ag film. For the STM measurements, we will focus our studies on large Ag(111) terraces.

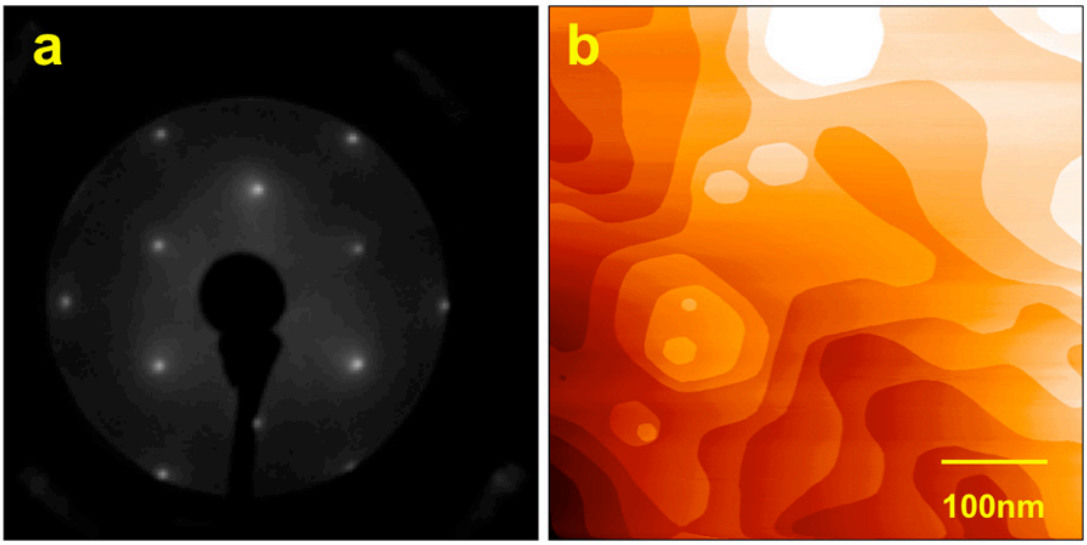

Figure 2.2 (a) LEED diffraction pattern shows sharp C6 symmetry lattice, (b) representative STM image of a clean, smooth Ag (111) surface, characterized with irregular steps and silver islands.

2.3 Organic Molecular Beam Epitaxy

Organic molecular beam epitaxial (OMBE) is an ideal growth technique for controlling the structures and hence the properties of molecular films. Samples prepared by OMBE allow for stringent control of film thickness, composition and processing conditions[65-68]. Growth strategies that involve both sequential deposition and co-deposition are used herein to selectively fabricate film structures that include nanophase-separated, intermixed (co-crystalline), and layered phases. From previous studies conducted in our group, binary monolayer films with donor (9-acridine carboxylic acid (ACA)) and acceptor (C_{60} molecules) were fabricated with film structures that range from an intermixed chiral phase to nanophase-separated single component domains[69,70]. Mismatched thermal properties, molecular masses and

molecular shapes of the film constituents allow for thermodynamic as well as kinetic control of binary film morphology.

TiOPc (Aldrich, 95% in purity) and C_{60} powder (Mer. Corp. purity $\geq$ 99%) are thermally deposited from separate effusion cells (Knudsen-type-evaporator) onto the atomically clean Ag(111) substrates in the main UHV chamber. C_{70} was loaded into a quartz crucible and was deposited in the loadlock chamber from a simple homemade evaporator. Deposition rate and surface coverage are directly calibrated with STM images as well as a nearby QCM. The deposition conditions for each species are summarized below in table 2.1. Here one monolayer of TiOPc is defined as 2 TiOPc molecules per 48 surface Ag atoms (1 TiOPc/1.73 nm^2) and one monolayer of C_{60} is defined as one C_{60} molecule per 12 surface Ag atoms (1 C_{60}/0.87 nm^2 Ag). For C_{70}, 1 ML is defined as one C_{70} molecule per 13-14 surface Ag atoms (1 C_{70}/0.9 nm^2). It should be mentioned that there is substantial ($\pm$50K) uncertainty in the absolute deposition temperature due to difference of the location and/or contact of the thermocouple used during the deposition.

Table 2.1 Deposition conditions for different molecules.

Molecule	Rate [ML•min^{-1}]	P_{max} [torr]	Temperature [K]
TiOPc	(0.1, 0.4)	1.0×10^{-7}	(480, 495)
C_{60}	0.01	4×10^{-9}	658
C_{70}	0.15	2×10^{-8}	530

2.4 Scanning Tunneling Microscopy/Spectroscopy

2.4.1 Introduction

With the development of surface science and nanotechnology, it is very important to observe the nanostructures and surface structure at very high resolution in real space. The invention of scanning tunneling microscopy (STM) provides us the unique experimental technique that can be used to characterize the surface with unparalleled resolution. The imaging resolution is so high that individual atoms become easily visible. With its ultimate resolution, STM and its family members (SPM: STM, AFM, MFM, EFM, KPFM, etc.) establish the basis of an enormous development in physics, chemistry, and biology within a very short time. In 1986, soon after the first publication about STM in 1981[71], the inventors of STM, Gert Binnig and Heinrich Rohrer were awarded the Nobel Prize in Physics. Nowadays, SPMs are used as both the standard surface analysis tools and high-level research instruments. There are huge amount of researches performed with SPM techniques and introduction to them is easy to access[72-76].

STM does not work in the way a conventional microscope does. It does not really magnify the sample until it can be watched with an unaided eye. Instead, a needlelike conducting tip (W, Pt/Ir) is scanning above the surface of a conductive (or semi-conductive) sample. The distance between the tip and the sample is only a few angstroms. When a small voltage is applied, electrons can jump or "tunnel" across the space between the tip and sample, building a small but detectable tunneling current based on quantum tunneling effect. As the tip moves along the sample surface, the

tunneling current flowing between the sample and tip is recorded. Then the computer generates a human readable image based on the recorded data.

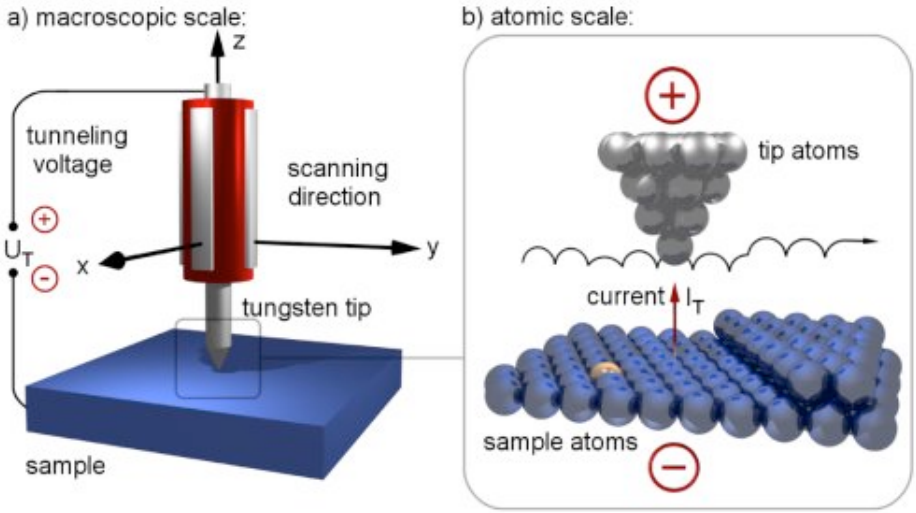

Figure 2.3 Simple schematic of the working principle of STM (not sized to scale). The motion of the tip operated in constant current mode over a surface step is indicated.

A schematic drawing of STM operation is shown in Fig. 2.3. There are several imaging modes for STM operation. Among them, the constant current mode and the constant height mode are the most popular ones. In constant current mode, a feedback loop is applied that the tip position can be adjusted vertically during scanning to keep a constant tunneling current. Since the current is proportional to the local density of states of the surface, as we will discuss in Sec. 2.4.2, the tip follows a contour of a constant DOS during scanning. A topography image of the surface is generated by recording the vertical position of the tip. In the constant height mode, the feedback loop is turned off and the vertical position of the tip is fixed. The tunneling current as a function of its lateral position represents the surface image. The advantage of this mode is STM can be operated at high scanning frequencies compared with the constant current mode. However, the sample surface must be atomic flat to avoid a tip

crash. Another important imaging mode is the current imaging tunneling spectroscopy (CITS). In this case, the tip is scanning over the surface in the constant current mode to give a constant distance to the sample. In addition, at each point given by a pre-defined grid, the feedback loop is disabled and a current-voltage curve (I-V curve) is recorded. Local electronic information can be deduced in the mode.

The development of STM has been one of the most important events in surface science area in recent years. It also opens up many new areas of science and engineering at atomic and molecular level, especially in the nanotechnology area. STM can be used to determine the local geometry and the local electronic characteristics of the sample. It also allows for the manipulation of individual atoms or molecules on the surface. The superb resolution, real space imaging, and high flexibility of STM make it particularly suitable for investigating the systems in my thesis works.

2.4.2 Basic Principles of STM

It is practically unrealistic to give an exact theoretical description of the tunneling process in STM due to the lack of a complete understanding of the quantum mechanical states of the tip and the scanned sample. For example, the determination of the tip states is problematic because of the uncertainty in tip geometry and chemical composition. Moreover, the tip situation is easy to change during experiments especially when adsorbates are presented on the surface. Nonetheless, instructive models with various approximations have been developed in the past[72,73,77].

According to quantum mechanics, an electron with wavelike characteristics will have a specific probability, P, to penetrate a barrier. For an electron with energy E to tunnel through a potential barrier E_{bar} (E_{bar}>E),

$$P \propto \exp[-2d\sqrt{2m(E_{bar}-E)}/\hbar] \tag{2.1}$$

where d and m are the barrier width and electron mass, respectively. Despite the complexity of the tip-sample system, most aspects of STM can be explained with the simple theory proposed by Bardeen[78]. In this theory, the specific geometry of the tip-sample junction is neglected, and the tunneling junction is modeled as a simple one-dimensional system. In the approximation proposed by Bardeen the net tunneling current between tip and sample measured while applying a bias V will simple be

$$I = \frac{4\pi e}{\hbar}\int_0^{eV} \rho_s(E_F - eV + \varepsilon)T(\varepsilon, eV, d)\rho_t(E_F + \varepsilon)d\varepsilon \tag{2.2}$$

where ρ_s and ρ_t are the density of states of the sample and tip, respectively, while $T(\varepsilon, eV, d)$ is the transmission coefficient for electrons with energy E tunneling from the tip into the sample.

For this simplified one dimensional model (Eqn. 2.2), the transmission coefficient

$$T(\varepsilon, eV, d) = \exp[-\frac{2d}{\hbar}\sqrt{2m(\frac{\phi_s + \phi_t - eV}{2} - E_F - \varepsilon)}] \tag{2.3}$$

where ϕ_s and ϕ_t are the work function of the sample and tip, respectively. It is important to note that Eqn. 2.2 is just the integral of the transmission coefficient over the density of states of the tip and sample within the energy interval allowed for tunneling (indicated by the arrows in Figure 2.4[77]). This interval corresponds to the energy range where the occupied states of the tip and the unoccupied states of the sample are overlapping. In this simplified model, both tip and sample have a perfectly

symmetric shape. The same assumption applies for negative sample bias (i.e. for electrons tunneling from occupied states of the sample to unoccupied states of the tip).

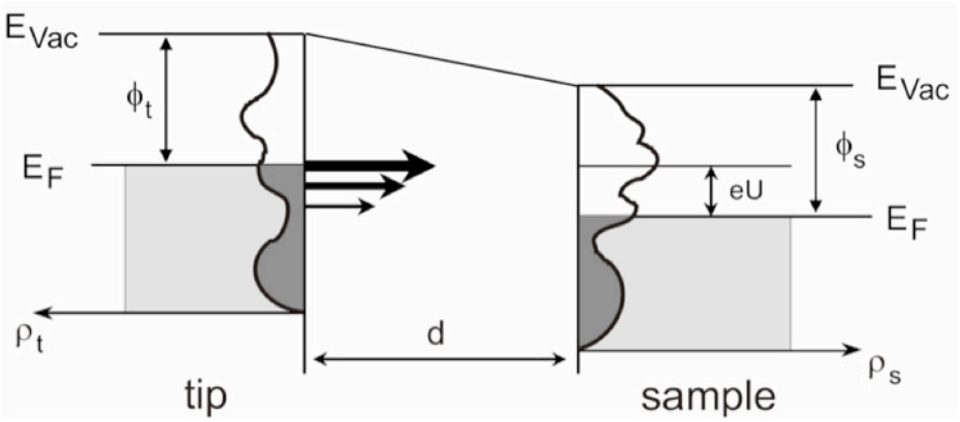

Figure 2.4 Schematic energy diagram for the one-dimensional tunneling process between tip and sample. ρ_s, ρ_t indicate the respective density of states for the sample and the tip which are separated by a distance *d*. The arrows in the gap illustrate the probability for tunneling (greatest near Fermi energy E_F) when a bias voltage *U* is applied.

In reality, the geometries of tip and sample are usually asymmetric and of various shapes. Such effects would complicate the situation significantly and make it almost impossible to develop a first principles model for the STM tunneling process. Many efforts have been made to build more realistic models with approximations closer to the real tunneling situation. The so-called s-wave-tip model developed by J. Tersoff and D. R. Hamann is certainly one of the most important ones[79]. It approximates the tip apex with a symmetric metal sphere, assuming that only the s states of the tip contribute to the tunneling process. At low bias voltage (much smaller than the tip work function ϕ_t), the current turns out to be proportional to the local density of states (LDOS) at the center of the sphere with radius r_0

$$I \propto eV\rho_s(E_F)\rho_t(E_F,r_0)\exp[-\frac{2d}{\hbar}\sqrt{m\frac{\phi_s+\phi_t}{2}}] \qquad (2.4)$$

Interestingly, in this approximation the dependence of the current on the DOS of the tip is only through $\rho_t(E_F,r_0)$ which is a constant in this approximation. Therefore, in the s-wave-tip model, the variations of the tunneling current during scanning depend solely on the local properties of the sample. In the case of clean metal surfaces, the STM image reflects dominantly the surface topography[78]. However, this situation is not necessarily true in the case where adsorbates presented as described in section 2.4.3.

It should be mentioned this simple s-wave-tip model fails to explain the observed atomic resolution on close-packed metal surfaces. Eventually, this puzzle is solved by C. J. Chen in 1990 by considering the d_{z^2} states of the tip[80,81].

2.4.3 Imaging Organic Adsorbates

The application of STM to image organic adsorbates and molecules on surfaces was firstly demonstrated in the mid 1980s, shortly after the invention of STM[82,83]. Before that, doubts were being raised due to the relatively large energy gap presented between the highest occupied molecular orbital (HOMO) and the lowest unoccupied molecular orbital (LUMO) compared to the low bias voltages applied in STM measurement. This energy gap was thought to prevent the electron tunneling under low bias voltage, leading to molecules' invisibility on the surface. What happens is, after molecules adsorption on the surface, the molecular orbitals (MO) can interact with density of states of the metal surface. As a result, the molecular imaging

becomes possible[84]. However, this also means that the HOMOs and LUMOs of adsorbed molecules differ from those of isolated ones.

Many effects can influence the appearance of adsorbates in STM images. Depending on the applied bias voltage, different MOs are preferred detected and give distinct features for individual molecules. Such an effect can be utilized to analyze the adsorption configuration/orientation of a molecule on a surface[85]. The molecular adsorption site on the surface also has an influence on the adsorption state. For example, a CO molecule appears either like a "bump" on top sites or as a sombrero-shape on bridge sites of Pt(111)[86]. For larger organic adsorbates, the final appearance in STM image depends on the bias voltage, adsorption site[87], and the surface geometry[88]. Moreover, an isolated molecule usually possesses a different appearance from those assembled into ordered structures due to the presence of intermolecular interactions in the later case.

There are other effects that influence the molecular imaging. Static conformational changes of the adsorbate on the surface can lead to different appearances of the molecules even on the same surface[89,90]. If the molecule (or moiety of molecule) diffuses or rotates much faster than the characteristic scanning speed of the STM, it would be very hard or even impossible to identify the molecule or its inner structure[91]. The imaging quality can be improved by lowering the sample temperature or increasing the adsorbate surface density (and increase the intermolecular interaction). Practically, the tunneling current indeed has a substantial dependence on the DOS of the tip. During STM studies of adsorbate systems, the tip can be easily

contaminated by molecules, leading to the change of scanning condition and consequently the recorded STM images.

Despite of the above-mentioned effects that might influence imaging process, STM is well proven as a powerful technique to investigate the adsorbate systems. Impressive literature has been accumulated in this topic[92-97]. Useful information can be explored with STM, such as surface kinetic and thermodynamic properties, molecular self-assembly process, nanoarchitecture, electronic properties, etc. of adsorbate on the supporting surface. In Chapter 3, 4, 5, and 6, I will present detailed STM studies on TiOPc, C_{60}, and C_{70}.

2.4.4 Scanning Tunneling Spectroscopy

Another powerful way to investigate a surface by means of STM is tunneling spectroscopy (STS). While the bias voltage is varied, the separation between tip and surface is fixed and the resulting tunneling current is recorded. From these *I-V* (tunneling current at corresponding bias voltage) curves, the normalized derivative $(dI/dV)/(I/V)$ can be calculated. From Eqn. 2.2, under the gross assumption the tip DOS is constant, we obtain

$$\frac{dI}{dV} \propto \rho_s(EF - eV + \varepsilon) \qquad (2.5)$$

The tunneling conductance is directly proportional to the sample LDOS at the given point on the surface. As bands are decided by the LDOS, STS can be used with "chemical contrast" to determine the HOMO-LUMO energy gap, band bending, and chemical bonding. However, the interpretation of tunneling spectra is challenging. Interpretation is based on the assumption that the tip is featureless, and its DOS resembles that of the free electron gas in an ideal metal. In reality, the validity of this

assumption requires special testing. Another problem is the dependence of the tunneling current on the tunneling transmission probability. As a result, the states of the sample that do not overlap with the ones of the tip are not accessible in the measurements[98].

Molecular systems are somewhat fragile and require special "handling". Large currents are destructive for molecular films and may be compensated by reducing the sample temperature during the measurements. An alternative low current method for measuring spectroscopic data is to keep the feedback active while ramping the voltage at a fixed tunneling current, resulting in *z(V)* traces. The tunneling current is held constant by moving the tip. In this way the tip-sample separation is constantly adjusting, and a large dynamic range in voltage can be obtained. To minimize perturbation to the film, low (~50 pA) currents are utilized and tip height *z* begins at a noncontact position (controlled via the initial voltage of ca. 0.5 V). The *z* position is then monitored as voltage is increased under constant low-current conditions. Electronic states are detected as steps in the *z(V)* trace, where the tip rapidly retracts due to an increase in tunneling probability resulted from resonance (Figure 2.5). The tip response time for *z* motion must be faster than the ramp rate. One limitation of this approach is that lower voltage ($4.0 \leq V$) cannot be measured reliably due to strong tip-sample interactions. The *z(V)* method is useful for locating the energetic position of bands, but the tip motion precludes an accurate determination of the LDOS.

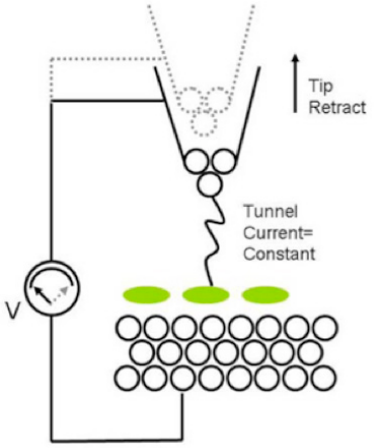

Figure 2.5 Schematic illustration of Z (V) curve measurement.

In this thesis, we mainly utilize *z-V* measurements to determine the energetic positions of electronic states with respect to the Fermi level. Experimental validation of this method is shown in Figure 2.6[99] where *z(V)* spectra of $(2\sqrt{3}\times 2\sqrt{3})\mathrm{R30}^{\circ}$ C_{60} on Ag(111) (Fig. 2.6a) are used to determine the electronic states and are compared to the results of ultraviolet photoemission spectroscopy (UPS) (Fig. 2.6b). In general, the two measurements agree within a few tenths of 1 eV.

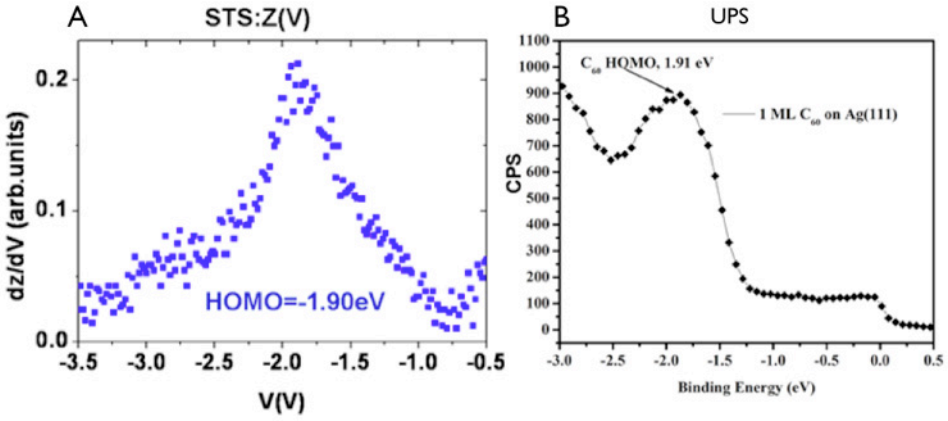

Figure 2.6 Validation of z-V scanning tunneling spectroscopy. Comparison of the highest occupied molecular orbitals (HOMO) for $(2\sqrt{3}\times 2\sqrt{3})\mathrm{R30}^{\circ}$ -C_{60}/Ag(111): (a) z-V spectroscopy (b) Ultraviolet photoemission spectroscopy (UPS).

2.5 Introduction to Molecular Modeling

Molecular modeling is the science of representing molecular structures numerically and simulating their behavior with the equations of quantum and classical physics. Computational chemistry programs allow scientists to generate and represent molecular data including geometries, energies, electronic properties, spectroscopic properties, and bulk properties.

Quantum theory uses well-known physical constants such as the velocity of light, values for the masses, charges of nuclear particles, and differential equations to directly calculate molecular properties and geometries. This formalism is referred as *ab initio* quantum mechanics.

The first approximation attempts to differentiate nuclei and electrons. It assumes that nuclei are much heavier than electrons and move much more slowly so that molecular systems can be viewed as electrons moving in a field of fixed nuclei (Born-Oppenheimer approximation). Solutions to the Schrodinger equation using this assumption lead to values of effective electronic energy that are dependent on relative nuclear coordinates[100].

The second approximation allows the orbital of a molecule to be represented by the linear combination of atomic orbitals of the atoms. This is called Linear Combination of Atomic Orbitals theory. Hartree-Fock theory is used to derive the orbital coefficients (which define the energy of the system). The theory is that the energy of a set of molecular orbitals can be derived from the basis set functions describing the orbitals by a set of adjustable coefficients that are used to minimize the energy of the system.

Walter Kohn showed in 1964/65 that the ground state energy of a quantum-mechanical system is uniquely determined by its electron density. This quantity is more easily handled than the complicated wavefunction in the Schrödinger equation. Kohn also provided a method that made it possible to set up equations whose solution give the system's electron density and energy. This method, called density functional theory (DFT) has become widely used in chemistry, due to its simplicity and applicable to fairly large molecules. It provides a good accuracy as long as the electron correlation is small.

There are other methods, which requires greatly reduce computational resources. An example is semi-empirical methods: rather than performing a full analysis on all electrons within a molecule, some electrons interactions, usually core electrons, are ignored. A further simplification is the Molecular Mechanics or Force Field method, mainly suited to compute molecular geometries and their associated properties. These methods rely on the laws of classical Newtonian physics and experimentally derived parameters to calculate geometry as a function of steric energy. Since they are fast and efficient, they can be used to examine systems containing thousands of atoms.

For TiOPc, *ab initio* density functional calculations using the Dmol[3] computational package with B3LYP functional at the 6-31Gd bases set level were performed. The charge distribution, electrostatic potential, dipole moment, and molecular orbitals including HOMO and LUMO are calculated.

Chapter 3 Single-Component Molecular Self-Assembly on Ag(111)

The molecules presented in this work can be divided into two categories. Fullerenes, C_{60} and C_{70}, are typically electron acceptor materials. They are selected for their good availability, tunable electronic properties[1-4] and ease of measurements on the surface. TiOPc, a conventional electron donor material in OPV cells, is selected in this work for its anisotropy (non-planar shape and electrostatic properties). The highly anisotropic intermolecular interactions between TiOPc can be used to control molecular architectures at surfaces as they do for the bulk crystal[5-8]. All materials are solids at room temperature and can be deposited by vacuum deposition.

3.1 Fullerenes Adsorption on Ag(111)

In 1985, Kroto et al. discovered large molecules consisting of carbon atoms. The name they proposed for the C_{60} molecule in their original paper[101] was Buckminsterfullerene in tribute to R. Buckminster Fuller who is best known for his work concerning the geodesic dome. Many closed-cage all-carbon molecules of different size have since been discovered including C_n with n=36 to bigger ones with n=60, 70 and 78, 90, and 96. This class of compounds has since become known as fullerenes. More than 20 stable fullerenes between n=60 and n=96 have already been characterized[102]. In 1996 Robert F. Curl, Harold W. Kroto, and Richard E. Smalley were awarded the Nobel Prize in chemistry “for their discovery of fullerenes”. Since 1990, C_{60} can be produced and isolated in macroscopic quantities[103]. Nowadays, C_{60}

and C_{70} along with many other fullerenes are commercially available in high purity (>95%). In this work, the fullerenes C_{60} and C_{70} were used. In Fig. 3.1 the structures of the two molecules are drawn to scale in order to reflect their respective sizes and shapes.

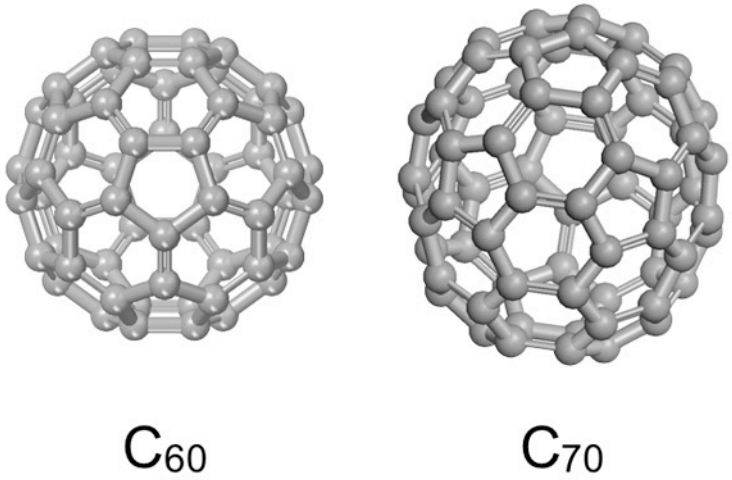

Figure 3.1 Chemical structures of fullerenes materials (a) C_{60} and (b) C_{70}.

3.1.1 C_{60} on Ag(111)

C_{60} is the most abundant member of the fullerene family. The structure of C_{60} resembles a round soccer ball made of hexagons and pentagons, with a carbon atom at the corners of each polygon and a bond along each edge. None of the pentagonal rings make contact with each other. The diameter of the C_{60} cage is 0.7 nm (center C atom to center C atom) and the molecule has a vdW diameter of $d(C_{60})$=1.06 nm[103,104]. C_{60} has a large ionization potential of about 7.8 eV compared to metal surface work functions (e.g. 4.6 eV for Cu and 5.4 eV for Au) and an electron affinity of 2.7 eV[72,102]. Thus, it is not surprising that C_{60} acts as an electron acceptor in many applications. C_{60} chemisorbs onto most metals (including Ag, Au and Cu) via charge transfer of up to 3 electrons per molecule (Ag(100))[102], hence forming an interfacial

dipole. Particularly for the substrates used in this study, namely Ag(111), the electron transfer per C_{60} molecule is 0.75[105]. The energy gap between the lowest unoccupied molecular orbital (LUMO) and the highest occupied molecular orbital (HOMO) is 1.9 eV[106]. Therefore, it is an intrinsic semiconductor. Previous temperature programmed desorption (TPD) studies reveal that the desorption temperature for C_{60} from Ag(111) is about 770 K, with a fullerene-substrate interaction of 2 eV per molecule[107,108].

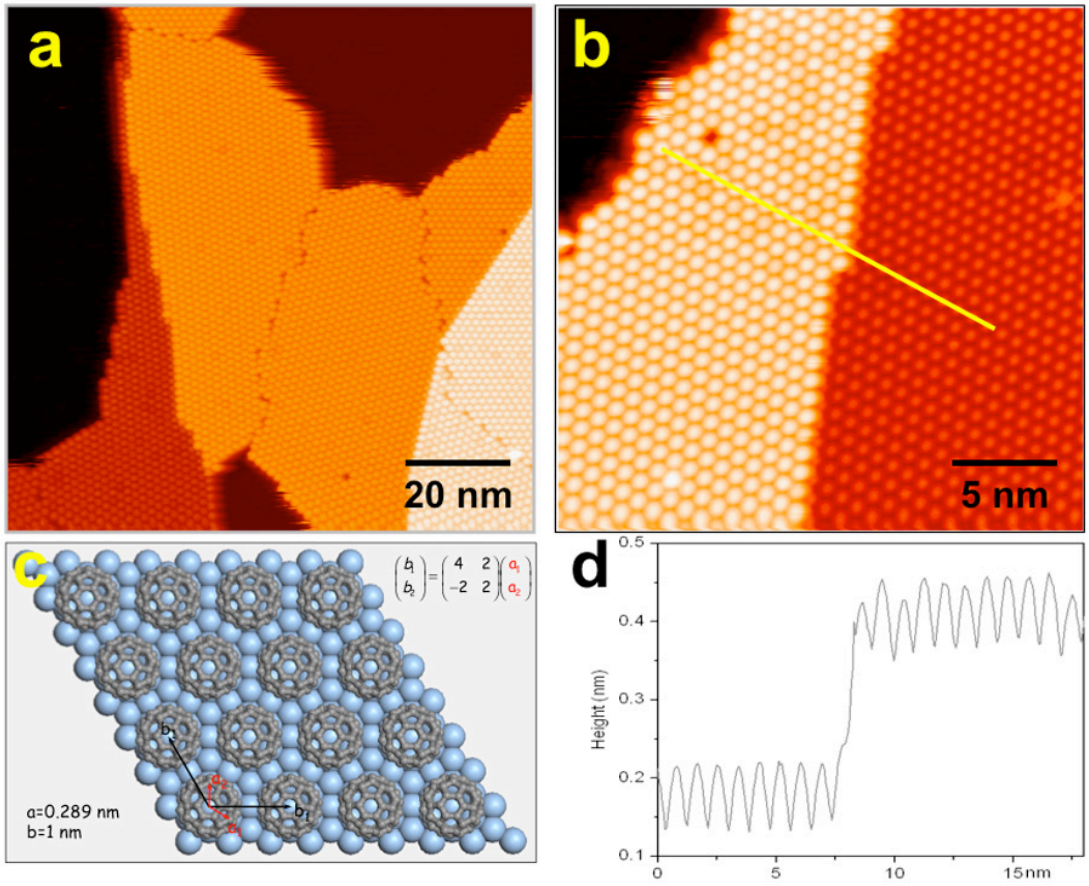

Figure 3.2 C_{60} monolayer structure on Ag(111). (a) Large scale STM image shows different rotational domains of sub monolayer C_{60} on Ag(111), (b) magnified STM image of $2\sqrt{3}\times 2\sqrt{3}R30°$ C_{60} superstructure, (c) adsorption model of C_{60} $2\sqrt{3}\times 2\sqrt{3}R30°$ structure on Ag(111), and (d) height profile along the yellow solid line in (b).

C_{60} adsorbed on noble metals has been widely studied[107,109-115]. They preferably condense along step edges at low coverage. Increase coverage usually leads to

hexagonal or quasi-hexagonal arrangements of the molecules. On Ag(111) they arrange into a $2\sqrt{3}\times 2\sqrt{3}R30°$ superstructure with respect to the Ag lattice (figure 3.2a and 3.2b). A C_{60} molecular packing model on Ag (111) is demonstrated in Fig. 3.2c. Two less stable phases are also observed. However, after mild annealing, only the most stable phase survives. Also, contrast difference between adsorbed C_{60} can be seen after annealing at 430K, probably due to molecules bound in different rotational orientations. However, the origin of the contrast difference of C_{60} is still under debate. Possible explanations include local surface reconstruction or electronic effects connected to the bonding C_{60} molecules with the substrate are discussed[116-118].

3.1.2 C_{70} on Ag(111)

C_{70} molecules are built analogous to C_{60} from hexagons and pentagons as shown in Fig. 3.1b. Due to the additional carbon atoms, C_{70} has an ellipsoid shape with diameters of 0.7 nm and 0.79 nm, respectively, along the two axes of the cage (atom center to atom center). The vdW diameters of C_{70} are d_{min}=0.9 nm along the short axis and d_{max}=1.2 nm along the long axis[119]. The ionization potential (7.3 eV) and electron affinity (2.7 eV) of C_{70}[102], are similar to the those for C_{60}. However, C_{70} has considerably higher dipole polarizability of 102±14Å^3, compared with the C_{60} value of 76.5±8Å^3.

The adsorption of C_{70} has been studied previously on metal surface. The first STM experiment was on Cu(111), where it forms a (4×4) C_{70} over layer. In order to accommodate the lattice mismatch between Cu and C_{70} of 4%[111], C_{70} generally adopts a standing-up orientation with its long axis almost perpendicular to the surface. A

more recent study of C_{70} on Au(111) reported two phases with one adopting the standing-up orientation and the other with the lying-down orientation[120].

The calibration involved the deposition of a partial monolayer of C_{60} to form either $(2\sqrt{3}\times 2\sqrt{3})R30^\circ$ or $(2\sqrt{3}\times 2\sqrt{3})R15^\circ$ close packed C_{60} structures. Subsequently deposited C_{70} phase segregate to form ordered C_{70} structures.

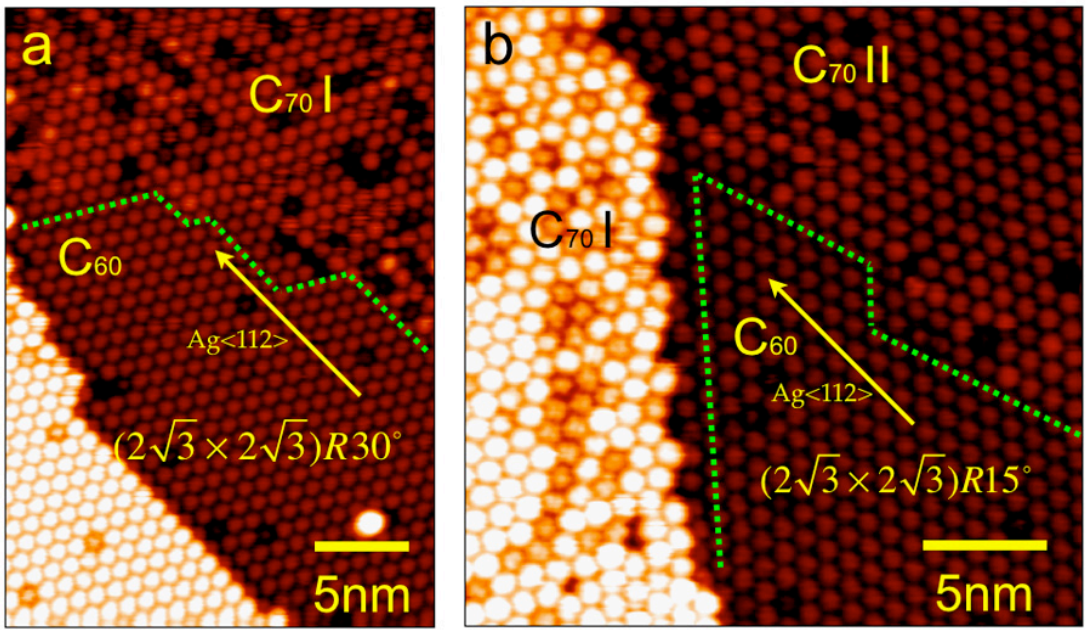

Figure 3.3 Binary C_{60}/C_{70} film monolayer on Ag(111). (a) $(2\sqrt{3}\times 2\sqrt{3})$R30° C_{60} adjoins C_{70} phase I (b) $(2\sqrt{3}\times 2\sqrt{3})$R15° C_{60} coexisting with C_{70} Phase I and II.

A binary molecular film of C_{60}/C_{70} is shown in Fig. 3.3. Domain boundaries between C_{60} and C_{70} are marked by a green dash line. Generally, we observe less contrast variation inside C_{60} domains compared to that of C_{70} domains. C_{70} structures adjacent to C_{60} domains were calibrated with different C_{60} structures. We have $(2\sqrt{3}\times 2\sqrt{3})R30^\circ$ C_{60} in Fig. 3.3a, and $(2\sqrt{3}\times 2\sqrt{3})R15^\circ$ C_{60} in Fig. 3.3b. Two phases of C_{70} are identified. Both of them are hexagonal close packed with a nearest

neighbor distance of 1.06 nm, but the close packed directions run along different Ag lattices vectors. We denote them as Phase I and Phase II in Fig. 3.3. Compared to Phase II, phase I has more contrast variations, and we ascribe these variations to different adsorption configuration (standing-up or lying-down). Both of these two phases are point-on-line commensurate with Ag(111) lattice. The registrations of these two phases with Ag lattice are summarized in table 3.1 of Section 3.1.3.

After the parameter calibration, pure C_{70} films were prepared and characterized, as shown in Fig. 3.4. C_{70} exhibits a different growth mode from C_{60}, as summarized below:

(1) Unlike layer-by-layer growth, multilayers of C_{70} start to grow before the first layer saturates, as marked in Fig 3.4a. Along the vertical direction, C_{70} have an fcc stacking, as shown in the model of Fig. 3.4c. This contrasts the layer-by-layer growth mode of C_{60}.

(2) Within the first layer, two metastable phases are observed. A interesting feature is that the intramolecular structure of single C_{70} as two elongated protrusions can be resolved at room temperature, as circled in Fig. 3.4b. This C_{70} signature indicates a lying-down orientation based on the lower apparent height and the molecular orbitals assignments. The LUMO orbitals of C_{70} are localized on the four pentagons facing upwards for a lying-down C_{70} (as shown in the inset of Fig. 3.4b), in agreement with STM images, in which two of pentagons are imaged as an elongated protrusion.

(3) On domain boundaries of C_{70} Phase I and II, dislocations are generally formed, as marked in Fig. 3.4b, and one example of the burgers vector is shown. These

dislocations are formed due to the mismatch between Ag lattice constant and C_{70} lattice, as we listed in table 3.1.

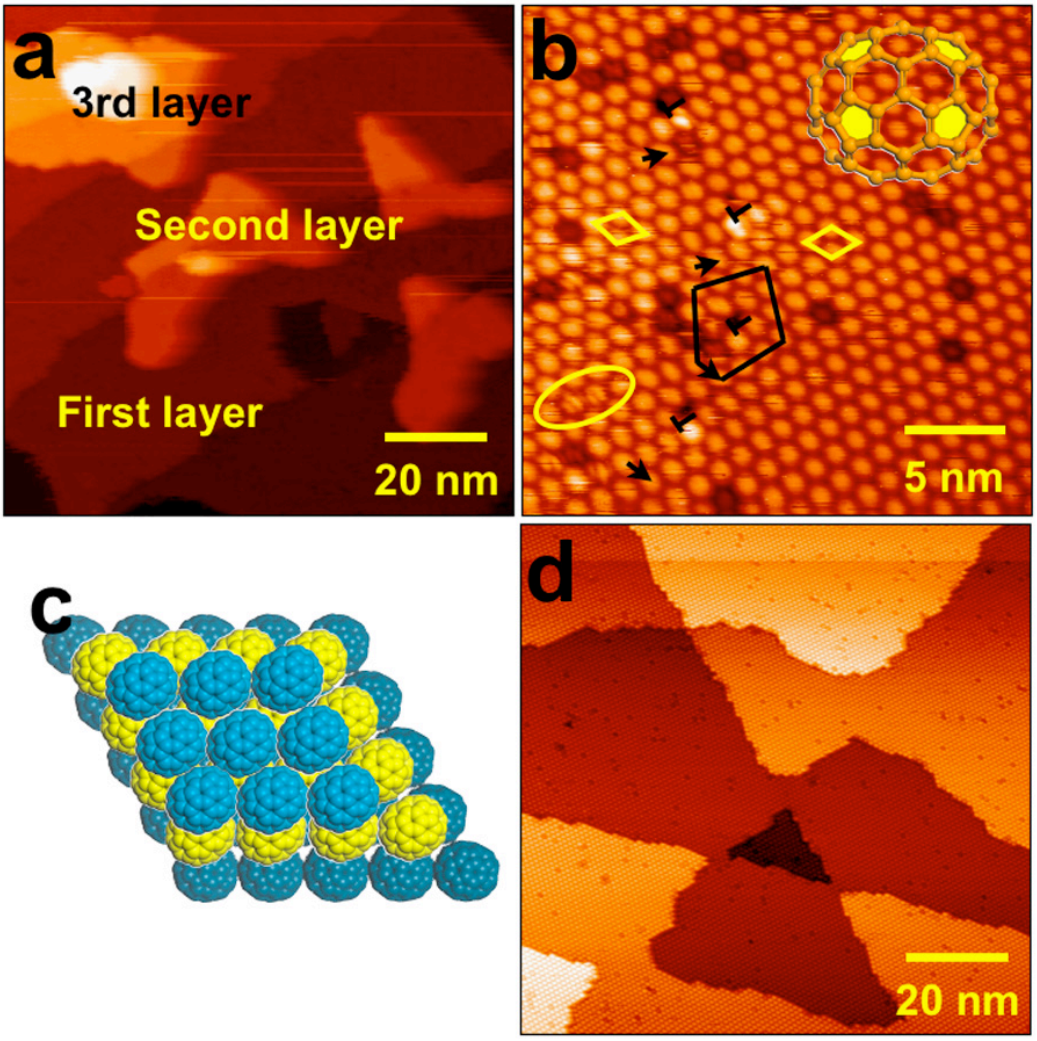

Figure 3.4 C_{70} structure on Ag(111). (a) Large scale STM image shows multilayer growth before first layer saturates, (b) high resolution STM image of C_{70} Phase I and Phase II with intramolecular resolution, (c) overhead view of C_{70} multilayer, and (d) large scale STM image of C_{70} monolayer after annealing at 400K.

(4) After a mild thermal annealing, only Phase II of C_{70} dominates on the surface, indicating that it is more stable than Phase I. This is consistent with less observed contrast variations in Phase II. As listed in table 3.1, Phase II also has less lattice mismatch (1.9%) with Ag(111) relative to Phase I (2.5%).

3.1.3 Summary

Fullerenes are popular adsorbates for surface science researches due to their properties and ease of use. In the following chapters, we will use them as probe molecules to study the heterostructures with other organic species, as well as the electronic properties along the domain boundaries.

Neither C_{70} nor C_{60} forms covalent chemical bonds with the Ag(111) substrate. However, the ca. 2eV binding energy classifies C_{60} and C_{70} as chemisorbates[107,108]. The phase diagram of C_{60} and C_{70} on Ag(111) surface are drawn in Fig. 3.5 by only considering the thermodynamically stable phase. Unlike many other small organic molecules, which need a critical nucleation density of the 2-D gas phase to initiate island nucleation, fullerenes have a very low critical nucleation density, and Ag(111) step edges decorated by single row C_{60} molecules have been observed at room temperature[121,122].

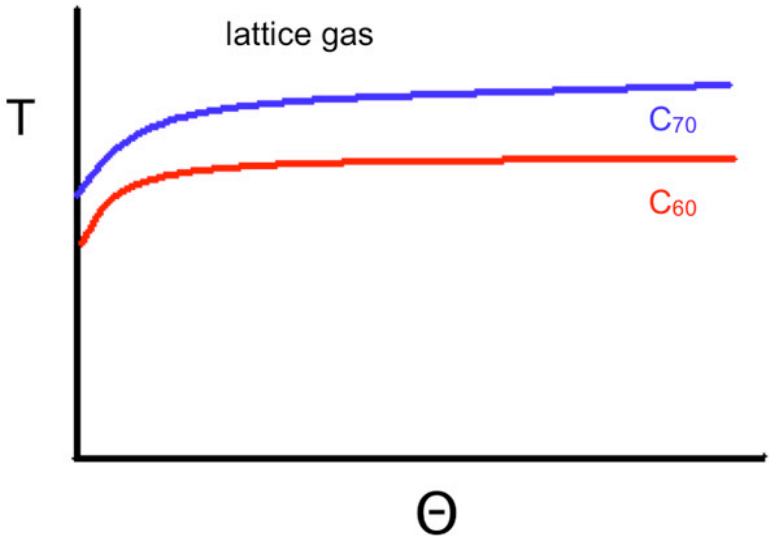

Figure 3.5 Schematic phase diagram of C_{60} and C_{70} on Ag(111) surface.

Table 3.1 Fullerene (C_{60}, C_{70}) registration with Ag(111) lattice.

	Bravais lattice	Lattice constant	Rotation from Ag[$1\bar{1}0$]	Ag lattice length	Corresponding fullerene close packing	Lattice mismatch
C_{60}	Hexagonal	10.4 Å	R30°	10.4 Å	10.4 Å	0%
C_{70} (phase I)	Hexagonal	10.6 Å	R32.5°	32.6 Å	3NNd=31.8 Å	2.5%
C_{70} (phase II)	Hexagonal	10.6 Å	R13.9°	10.4 Å	NNd=10.6 Å	1.9%

Both of these two fullerenes have high polarizability, mainly due to their delocalized π orbitals extending around the carbon cage. For example, the degenerated LUMO orbitals are show in Fig. 3.6. Due to their large molecular weight, a significant van der Waals interaction originates from mutually induced polarization fluctuation on the molecules and on Ag (111) surface[123,124].

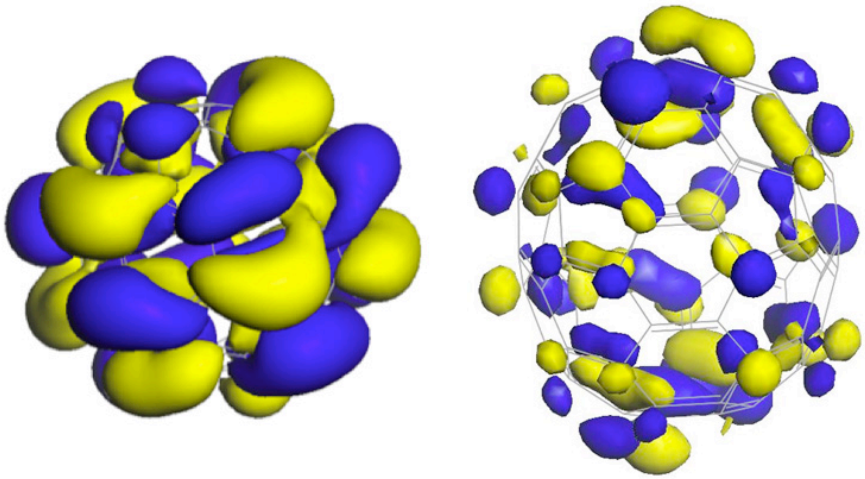

Figure 3.6 LUMO orbital of C_{60} (left) and C_{70} (right).

C_{70} has a higher polarizability than C_{60} and possesses a Stranski-Krastanov growth mode on metal surface instead of layer-by-layer growth. In the following chapter, we are going to show how the difference in polarizability influences their heterointerfaces formation with another molecular species (TiOPc).

3.2 Titanyl Phthalocyanine Ordering on Ag(111)

TiOPc is chosen in our experiment for its highly anisotropic intermolecular interactions and for its electron donating properties relate to fullerenes. The orientation dependence of TiOPc intermolecular interactions can be harnessed for polymorph selection and property control. The chemical structure of a TiOPc molecule is shown in Fig. 3.7a. This nonplanar molecule has C_{4v} symmetry, with the titanyl core protruding from the phthalocyanine macrocycle. Based upon a geometric optimization performed with Dmol[3], the height of the molecule (oxygen-macrocycle base distance), is 0.23 nm, and the hydrogen-to-hydrogen diameter (at the widest point) is 1.5 nm. TiOPc is a polar molecule with a calculated axial permanent dipole moment of 3.07 Debye pointing from the electronegative O atom to the center of the electropositive Pc ring. The TiOPc electrostatic potential is provided in Fig. 3.7b. Technologically useful physical properties of TiOPc include broad optical absorption that spans the near infrared-visible region and high photoconductivity[50,125,126].

Interest in TiOPc has led to several recent STM studies involving monolayer films. On Au (111), TiOPc molecules adopt a flat-lying geometry and pack with a square unit cell[57], while on HOPG, they pack with a hexagonal unit cell and individual molecules appear triangular in STM images[127]. This structure sensitivity of TiOPc monolayer films motivates this thesis study, in which we manipulate monolayer structure through growth kinetics.

Organic monolayer films can exhibit different adlayer structures depending on many factors, such as substrate temperature[128-131], surface coverage[70,132,133], and growth substrates[134-137]. Deposition flux is seldom reported as a determining factor for

phase selection, except for the influence on islanding at submonolayer coverage[138-140]. Film growth models generally describe how the flux/diffusion length ratio determines the island size distribution. Here we demonstrate the monolayer phase-sensitivity of TiOPc films to deposition flux. Low deposition fluxes delay the critical coverage of island formation, selecting the most thermodynamically stable adlayer structure. Moderate deposition fluxes yield a metastable film with uniform molecular orientation. We describe how flux impacts film growth through density variations in the 2-D molecular gas.

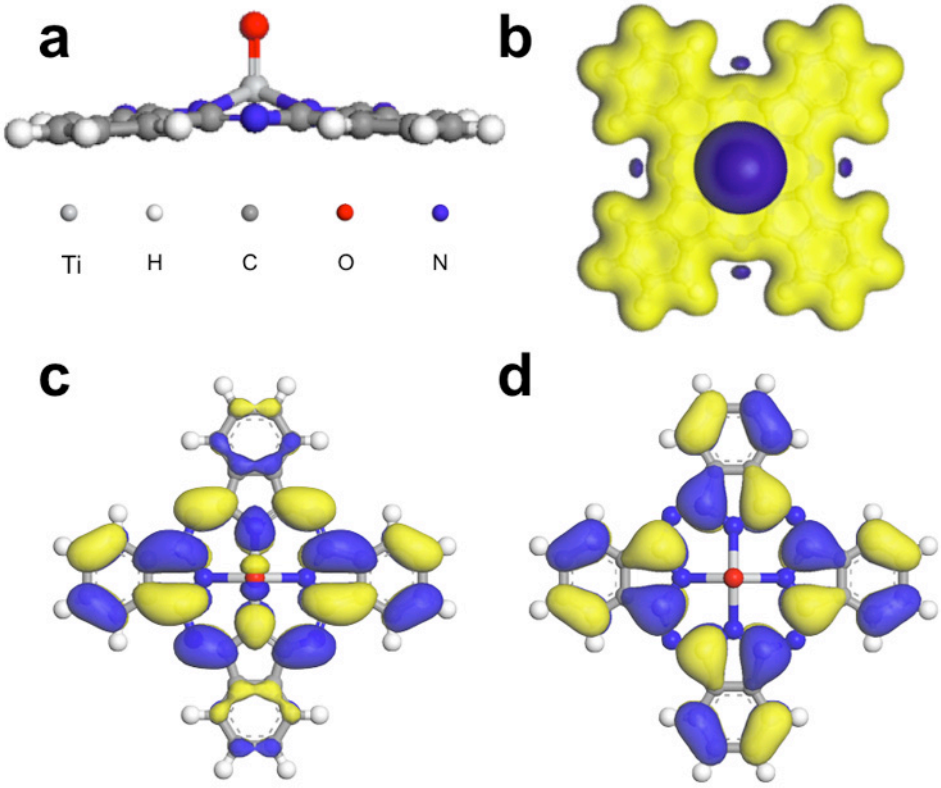

Figure 3.7 (a) Side view of the geometric structure of a free TiOPc molecule, (b) corresponding top view of charge distribution map of TiOPc, blue (yellow) represents negative (positive) charge distribution, the cutoff is ± 0.04 a.u. Å^{-3}, (c) calculated HOMO orbital of TiOPc, and (d) calculated LUMO orbital of TiOPc.

Using deposition flux as a key variable, we show distinct monolayer film structures are created. Scanning tunneling microscopy images reveal TiOPc arranged in honeycomb and hexagonal structures, as well as a misfit dislocation network of triangular domains. We propose detailed structural models for these three distinct film structures and relate film stability to electrostatic properties. Also, we describe how deposition flux captures molecular anisotropy to drive phase selection.

3.2.1 Low Flux Deposition

Deposition with a low (0.1 ML/min) flux up to a coverage of 0.47 ML (all ML are defined with respect to the unfilled honeycomb phase) yields no ordered structures on the room temperature surface. Once a 0.47 ML TiOPc threshold is reached, ordered islands begin to nucleate on the terrace, growing to cover the surface with one uniform monolayer.

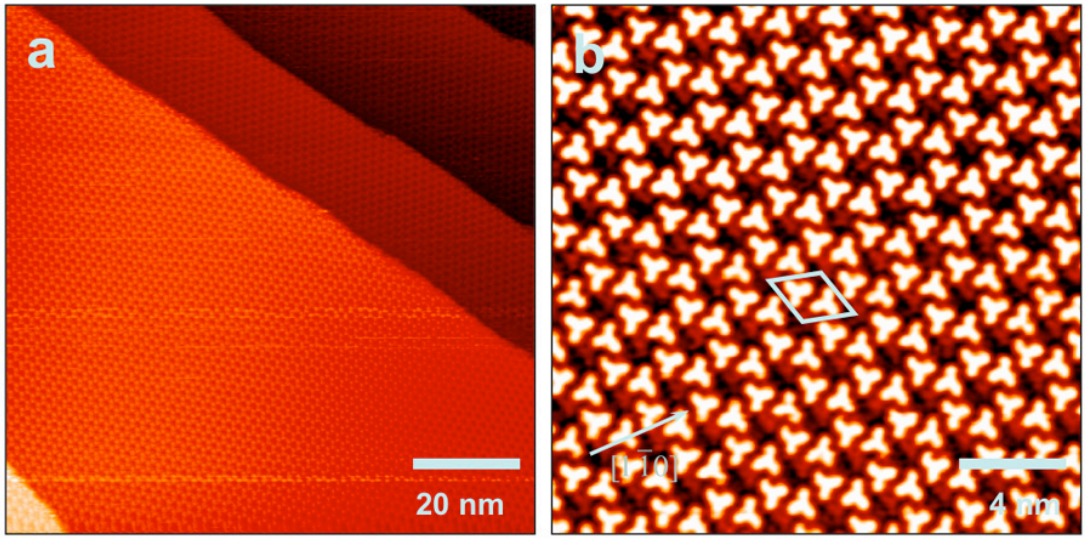

Figure 3.8 STM image of a full monolayer of TiOPc honeycomb phase on Ag (111): (a) Large field of view, shown as a differential image with tunneling condition: (+0.66V, 0.7pA), (b) Molecularly resolved constant current image obtained at higher magnification (20nm×20nm field of view). Each molecule displays a triangular shape with three lobes corresponding to two phenyl rings and one upward oxygen atom. Tunneling condition: (-0.69V, 0.57pA).

An STM image of the ordered adlayer formed by the lowest (0.1 ML/min) flux of TiOPc is shown in Fig. 3.8. This single-phase structure is described as a honeycomb phase. A high magnification image of this honeycomb phase is shown in Fig. 3.8b. Each triangular feature in Fig. 3.8b is attributed to a single TiOPc molecule. Six molecules with alternative orientations arrange into one honeycomb cage. The TiOPc adlayer is commensurate with the Ag (111) substrate, as evidenced by the observation of orientational domains. (In Fig. 3.8a, for example, the unit cell vector of the domain spanning the widest terrace is rotated by 120^{o} relative to the domain on the lower terrace.) The unit cell, drawn with a blue solid line in Fig. 3.8b, is described as $(2\sqrt{13} \times 2\sqrt{13})$R13.9^{o} -TiOPc/Ag (111) in Woods notation or (6 -2, 2 8) in matrix notation.

As shown in Fig. 3.8b, two nearest-neighbor TiOPc molecules with distinct orientation form an interlocked pair, which packs in a staggered pattern to form the honeycomb structure. Images with similar resolution were obtained with different bias voltages and opposite polarity, indicating the high stability of this structure. Unlike previous studies of TiOPc[57,127] on Au and HOPG substrates and VOPc[141] on Ag(111) , TiOPc does not adopt a uniform molecular orientation at these fluxes. Instead, TiOPc arranges into a honeycomb structure comprised of molecules with two different tilted orientations.

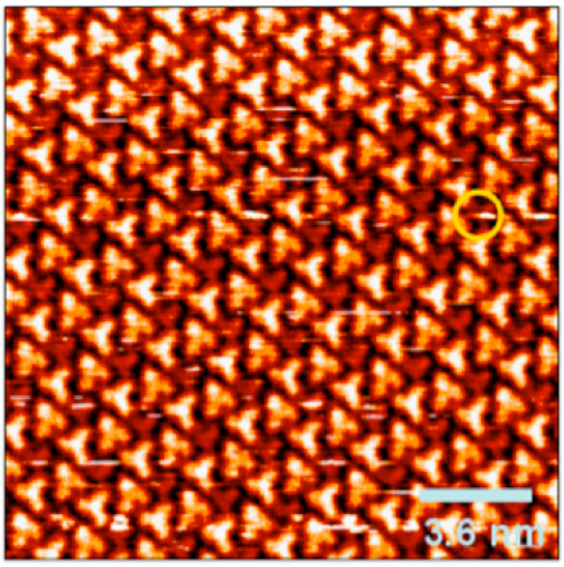

Figure 3.9 High resolution image of TiOPc honeycomb phase contrasts the "frame" molecules (bright triangles) from the "hole" molecules (dim features). Streaks on the "hole" molecules (circled in yellow) indicate tip dragging, indicative of more weakly bound species.

In addition to the bright triangular molecular features that comprise the honeycomb frame, the pores of the honeycomb contain a dimmer feature, indicating occupation by a TiOPc molecule. In high resolution images (Fig. 3.9), images of pore molecules exhibit streaks resulting from the dragging of pore molecules by the STM tip. The dragging of pore molecules, while the honeycomb frame molecules remain fixed, indicates that the pore molecules are more weakly bound than the frame molecules. The honeycomb framework is very stable. Extended annealing to temperatures of 450 K does not degrade the honeycomb network, instead, a reduction in the TiOPc occupation of pore sites may be induced.

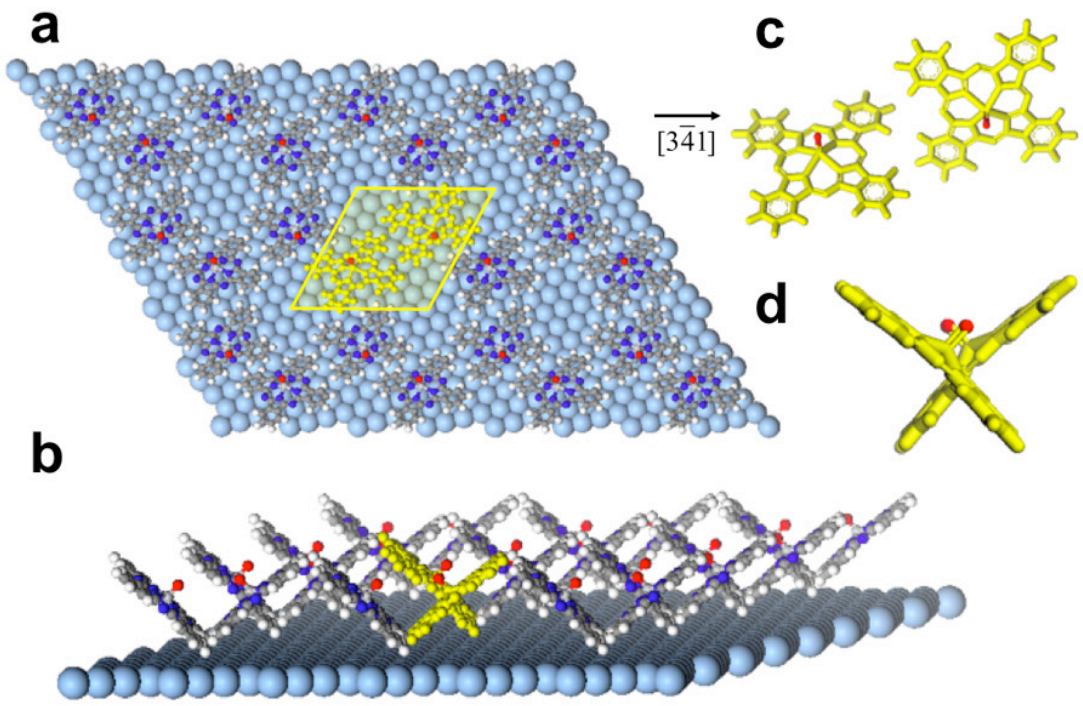

Figure 3.10 Proposed molecular packing model for the unfilled honeycomb phase. (a) Top view of honeycomb molecular frame. The unit cell is indicated by the yellow rhombus. The dimer of TiOPc within each unit cell is highlighted by yellow, (b) side view of honeycomb molecular frame, with TiOPc dimer highlighted again in yellow, (c) top view of the "on-edge" orientation TiOPc dimer that forms the basis for the honeycomb phase, and (d) side view of the "on-edge" TiOPc pair.

The proposed molecular model for the most stable honeycomb phase is shown in Fig. 3.10. The unit cell contains two TiOPc molecules, indicated by the yellow rhombus in 3.10a, and involves a $40^{o} \pm 10^{o}$ tilt of the TiOPc molecule with respect to the surface plane. This tilting is needed to accommodate the observed surface density of TiOPc. Within each unit cell, the pair of molecules involves a counter rotation to generate a twist-pair "on edge" structure, as shown in Fig. 3.10c and 3.10d.

The stability of this honeycomb phase indicates very favorable TiOPc-TiOPc interactions. Indeed, the "on-edge" oriented dimer of TiOPc molecules in one unit cell is highly stabilizing. The quadrupole attraction of two macrocyclic molecules are maximized in the "on edge" configuration by a dominant $\sigma - \pi$ interaction[142]. Such

an “on edge” molecular packing is widely adopted by metal Pc and other macrocyclic aromatic molecules as a “herringbone” arrangement in their bulk crystal structures[143-145]. We note that the in plane component of the 3 Debye molecular dipole moment is 1.9 Debye, leading to a residual dipole of just 2.3 Debye at the 1.3 nm TiOPc spacing. These TiOPc dimers organize into an offset honeycomb pattern, further minimizing the dipole-dipole repulsion between the dimers. In principle, a larger tilt angle would be more electrostatically favorable, but this would occur at the expense of the chemisorption energy (decreased pi-surface interaction). Because the honeycomb structure is in registry to the Ag (111) lattice, the TiOPc interaction with the substrate clearly favors the (6 -2, 2 8)-TiOPc/Ag (111) honeycomb phase. The total stability of the adlayer reflects both TiOPc adsorption and TiOPc-TiOPc interaction.

Molecules trapped in the hole of the honeycomb are imaged with some variations in apparent shape. This is not particularly surprising, as the 3-fold symmetry of the honeycomb "holes" does not match the 4-fold symmetry of the individual TiOPc molecules. The "hole molecules" appear as weaker protrusions that mostly align with respect to the honeycomb phase. Such "hole molecules" are easy to disperse and have streaks on them during scanning, or otherwise change shape with respect to imaging, indicating somewhat weaker binding than that the honeycomb frame molecules.

Two growth conditions are needed to select the honeycomb structure at room temperature - a critical coverage of 0.47 ML and low (<0.1 ML/Minute) flux. This high critical coverage suggests a relatively large critical nucleus, as would be expected for the honeycomb structure, in which four TiOPc dimers would be needed to nucleate a single pore. Low deposition fluxes ensure near-equilibrium growth

conditions[45], enhancing the uniformity of the 2-D molecular gas density. Low flux conditions thus allow a critical coverage of 0.47 ML to be reached without premature nucleation of the hexagonal phase.

3.2.2 Medium Flux Deposition

With a medium flux, island nucleation occurs at lower threshold coverage of just 0.40ML (See session 3.3.4) and the observed islands exhibit a hexagonal structure. Submonolayer hexagonal islands, coexisting with a 2-d TiOPc gas phase, are more difficult to image and appear less stable than the submonolayer islands of honeycomb structure.

With increasing coverage, the hexagonal islands grow and become more stable and easier to image. Monolayer films of the hexagonal phase are shown in Fig 3.11. In contrast to the honeycomb structure, all molecules within the hexagonal phase display the same orientation. Like the honeycomb phase, individual TiOPc molecules display triangular features in STM images. Such triangular features belie the intrinsic C_{4v} symmetry of the TiOPc molecule, suggesting a tilted orientation. The physical origin of this structure, as well as a detailed structural model, will be discussed further in Section The hexagonal phase is commensurate with Ag lattice, as determined by the observation of 120^{o}-rotational domains. This phase is represented as $(\sqrt{21} \times \sqrt{21})$R10.9^{o} in Woods notation (or (4 -1, 1 5) in matrix notation), as shown by blue solid line in Fig. 3.11b. The packing density is 17% less dense than the filled honeycomb phase (and 19% higher than that of the honeycomb frame.)

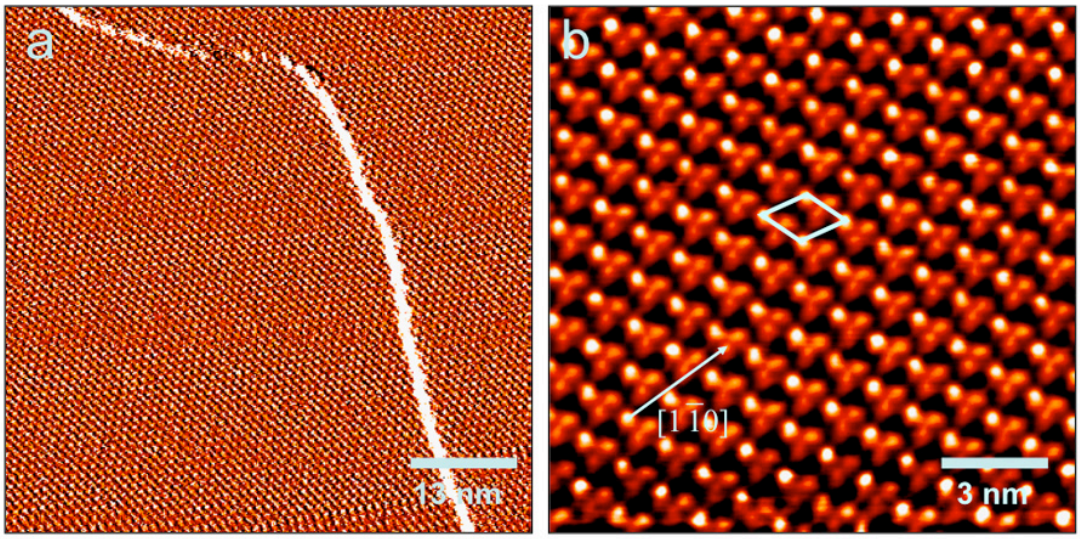

Figure 3.11 STM image of a near monolayer of TiOPc hexagonal phase on Ag (111): (a) Large field of view shown as a differential image. Tunneling condition: (+0.6V, 0.4pA), (b) Molecularly resolved constant current image (15nm×15nm). Each molecule exhibits three distinct lobes corresponding to two phenyl rings (more dim) and the projecting oxygen atom (brighter). Tunneling condition: (-0.8V, 0.4pA).

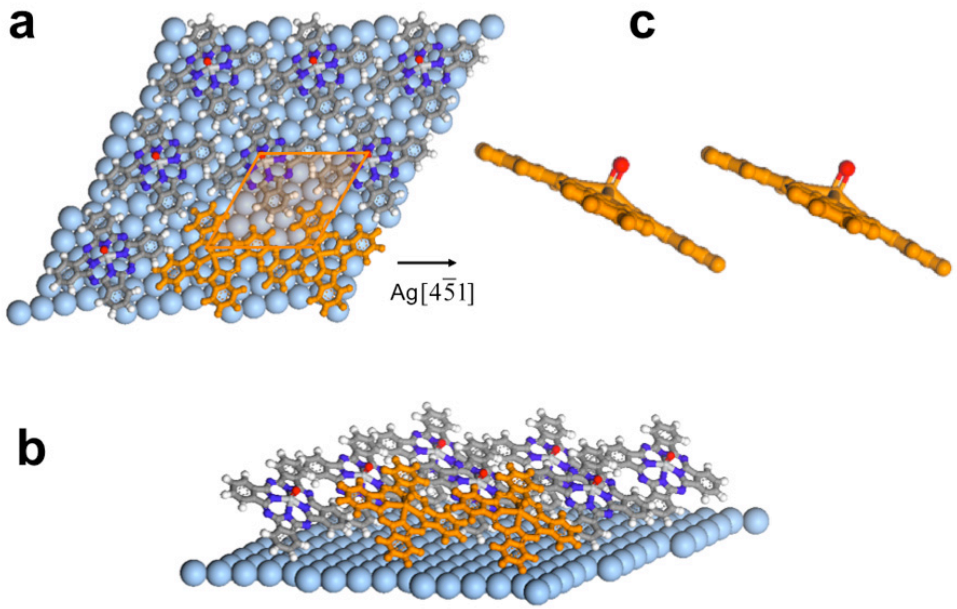

Figure 3.12 Proposed molecular packing model for the hexagonal phase (a) Top view with a unit cell indicated by the gold rhombus. (b) Side view of the hexagonal packing, and (c) The "face to face with offset" pair of TiOPc.

Thermal annealing of the film to 430 K for 20 minutes rapidly reduces the size of hexagonal islands, with no apparent conversion to the honeycomb phase. The

hexagonal phase is thus a metastable phase that is directly accessible through medium TiOPc flux.

At medium flux, TiOPc assemble into a close packing hexagonal arrangement, as shown in Fig. 3.12. In this model, all molecules are uniformly oriented with their oxygen pointing away from the surface. Like the honeycomb phase, the TiOPc molecules are tilted, albeit with an angle of just $30° \pm 10°$. The partial overlapping of the aromatic Pc rings without rotation is also reported to be an optimal configuration for two macrocyclic molecules to produce a stronger attraction between their quadrupoles, and is described as "overlap with offset"[142], as specified in Fig. 3.12c. The quadrupole attraction of the pair is enhanced by putting one lobe of the Pc ring close to the center of the eclipsed ring, thus forming a σ-π interaction between two rings. In the bulk crystal structures of π conjugated organic molecules, this overlap configuration is also widely adopted, but is reported to be slightly less favorable than the herringbone structure for the same molecule[146,147]. The TiO- dipoles in this overlap-with-offset motif are reduced to 2.6 Debye spaced by 1.3 nm. Evidently, the energy cost due to a weaker π interaction between the Pc rings and the Ag (111) substrate is compensated by the energy gain due to this electrostatic attraction.

We note that a higher TiOPc flux (0.2 ML/min) nucleates the hexagonal structure at a critical coverage of just 0.40 ML, lower than the coverage onset for the honeycomb phase. Several factors select the hexagonal phase under these farther-from-equilibrium growth conditions. First, the structurally simpler hexagonal phase (single molecular orientation), should require a smaller critical nucleus, permitting nucleation at lower coverage. Secondly, the increased flux pushes the growth

condition farther from equilibrium, causing greater variation in the 2-D gas density that causes early nucleation. The "overlap with offset" orientation of the hexagonal phase is the kinetically accessible packing mode under these growth conditions, as it requires simple collisions between near-parallel TiOPc molecules at modest densities.

3.2.3 High Flux Deposition

With a yet higher flux, TiOPc molecules no longer form the large singular domains that are observed for the honeycomb and hexagonal phases. Rather, a quasi-periodical triangular network appears on the surface, as shown in Fig. 3.13. When the triangular network covers a small (<25%) fraction of the surface, the discrete, triangular domains have limited stability and do not display a clear registration with the (111) substrate. With increasing coverage, the triangular network expands and becomes more amenable to high resolution imaging. From the magnified image, shown in Fig. 3.13b, the unit cell size within each of the triangular domains is identical to the hexagonal phase. However, the base lattice vector for these small hexagonal domains runs along the $[3\bar{5}2]$ direction of the silver lattice. Thus, the triangular domains exhibit a different orientation (and registration) with the (111) substrate. The triangular domains display a remarkable uniformity in size with 11~13 molecules packing along each side, creating a domain length of *ca.* 15 nm. All TiOPc within one triangular domain have the same orientation, as for the hexagonal phase.

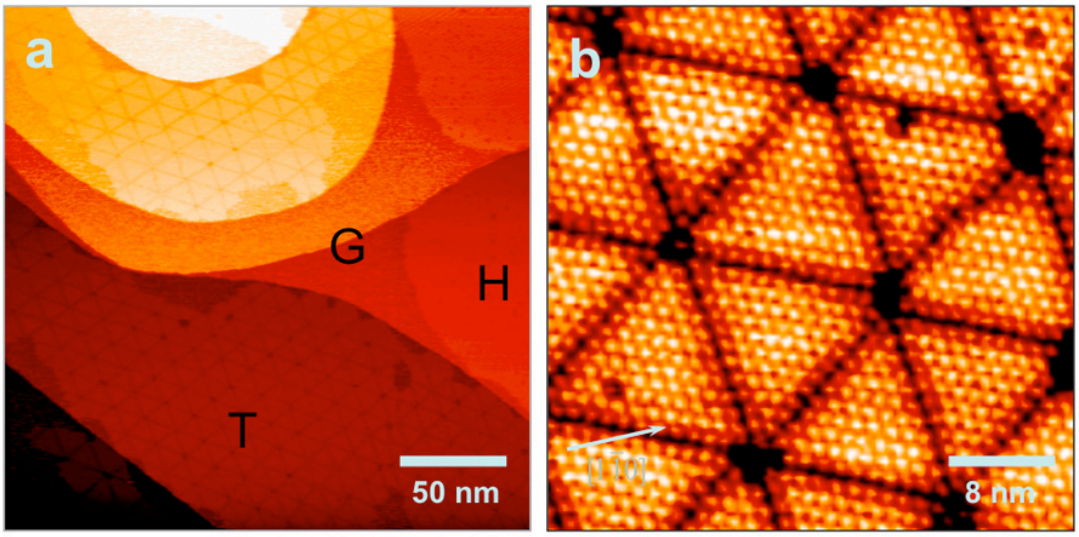

Figure 3.13 STM images of the misfit dislocation triangular network of TiOPc: a. large scale image (differential mode) shows the triangular network (T) in coexistence with the hexagonal phase (H) and dense 2-D gas phase (G). Tunneling condition: (+0.7V, 0.4pA), (b) High resolution image (40nm×40nm) of the triangular network. Each molecule is represented by a bright spot on the image tunneling condition: (+0.7V, 0.4pA).

The long range order of the domain network indicates a common structural relationship between neighboring triangular domains. The domain offset juxtaposes TiOPc molecules of alternating orientation along the boundary. The intersection of six adjacent triangular domains reveals two structural variations: One intersection involves perfect vacancy-free packing of TiOPc. The second involves the formation of a void with 3~4 missing molecules. While the triangular network grows to cover large areas of the surface, we have never generated a complete monolayer of this structure. Its formation appears to be self limited to about 70% of the fractional surface area, with the remaining surface covered either with a dense 2D gas (mobile disordered phase) or the hexagonal phase, shown in Fig. 3.13a. At room temperature, the triangular network structure is very stable. Thermal annealing of the network

structure to 390 K transforms the structure to the hexagonal phase. The network structure is thus a metastable structure.

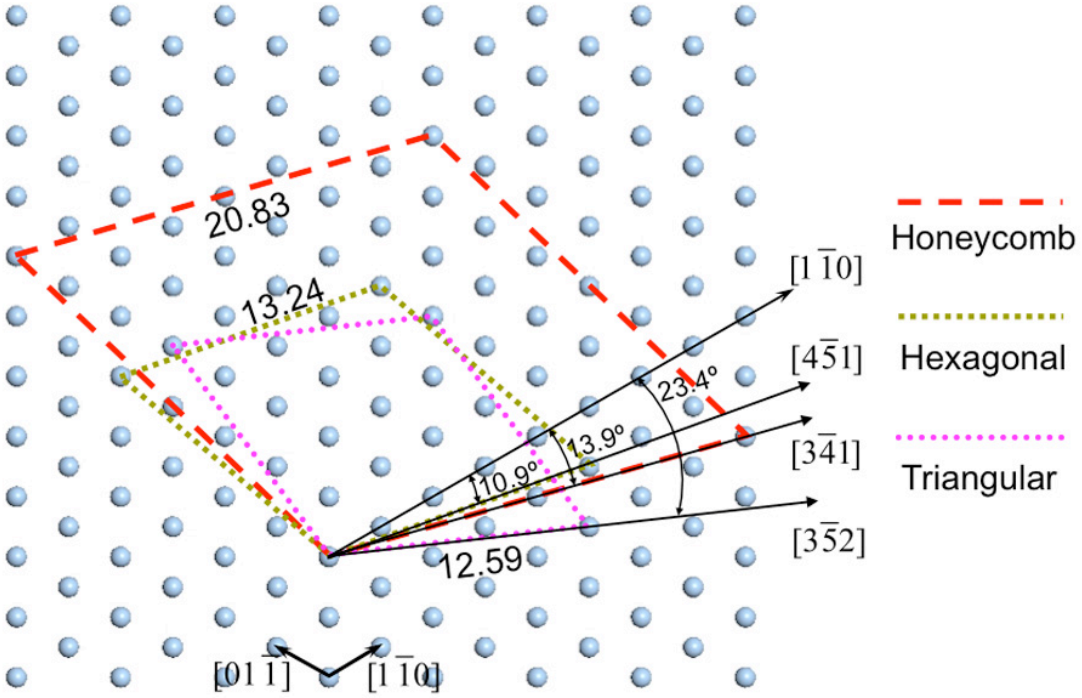

Figure 3.14 Unit cell of the three ordered phases observed for TiOPc monolayers on Ag (111). Bravais vectors, as well as the azimuthal rotation from the substrate [1 $\bar{1}$0] direction, are indicated.

A key difference between the high-flux hexagonal domains and the singular hexagonal phase, accessible at lower fluxes, is in the adlayer alignment with respect to the silver substrate. For the high-flux islands, the hexagonal unit cell vector runs along the substrate [3$\bar{5}$2], as opposed to the [4$\bar{5}$1] direction observed for the pure hexagonal phase. For both adlayers, the unit cell length, corresponding to a 1.32 nm nearest-neighbor separation remains the same. In the case of the pure hexagonal phase, as shown in Fig. 3.14, the TiOPc unit cell along the [4$\bar{5}$1] Ag azimuth similarly has a 1.32 nm separation between the registering Ag atoms, and the

hexagonal phase is commensurate with the Ag (111) surface. However, for the high flux structure, the "registering" Ag atoms along the unit cell's $[3\bar{5}2]$ endpoints are separated by just 1.26 nm. The interaction between the triangular domains and the Ag (111) surface thus imposes a compressive stress on the TiOPc adlayer. To relieve this stress, a misfit dislocation forms at 11~13 molecule intervals along $[3\bar{5}2]$, driving the formation of uniformly sized hexagonal domains.

Our model for the triangular network possesses three types of domain boundaries, as shown in Fig. 3.15. The molecular pairs marked A1 and A2 are organized in the "on-edge" configuration similar to that stabilizing the dimers in the honeycomb phase, with somewhat different twist and tilt angles. This arrangement provides electrostatic stabilization, thereby reducing the energy of the domain walls. To establish the periodicity of the network, another type of domain boundary is needed, marked by B in the model. Along this boundary, molecules are tilted toward the boundary. The pair of oppositely tilted TiOPc along boundary B possess no in-plane dipole and a reduced vertical dipolar component. Effectively, the three types of domain boundaries are stabilized by the electrostatic interactions.

The formation of a triangular network suggests that small hexagonal domains were simultaneously nucleated on the surface. The observed domain size would then require a diffusion length of <15 nm. This short diffusion length is completely consistent with the high flux growth conditions.

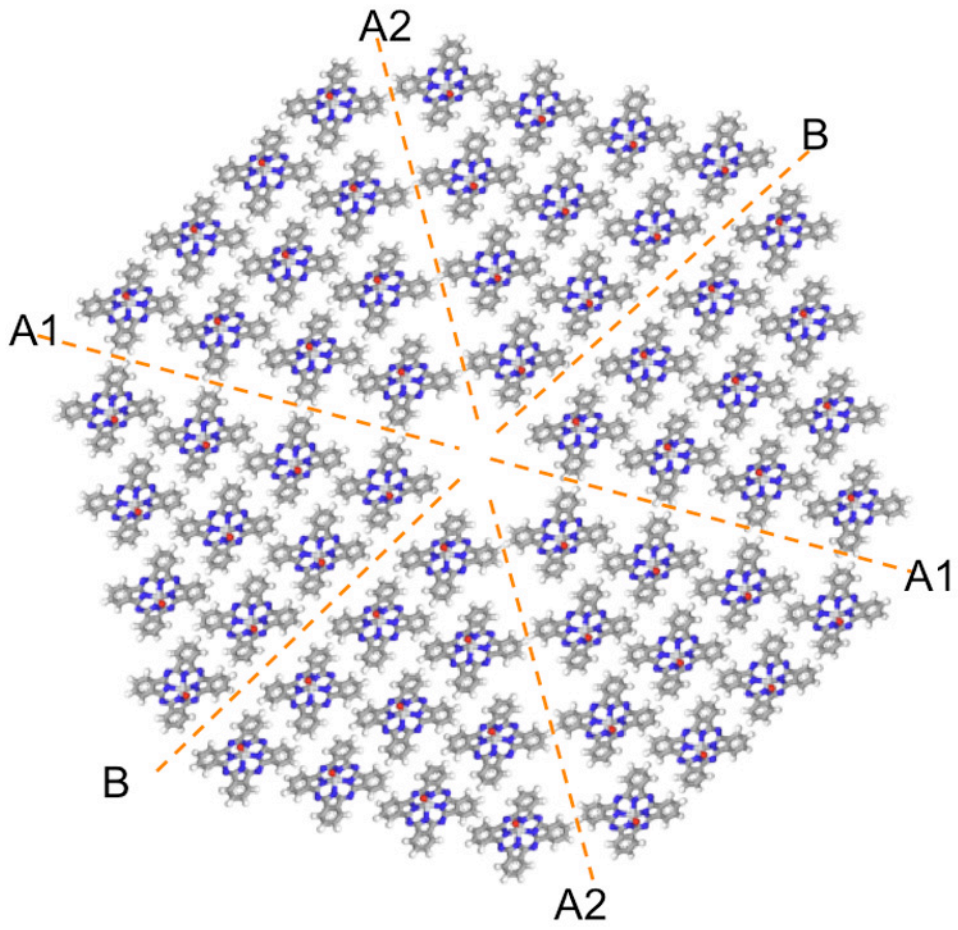

Figure 3.15 Proposed model for the triangular network phase of TiOPc. A1 and A2 mark the domain boundaries with twisted "on-edge" molecular pairs; B marks the domain boundary with opposing TiO tilts. For clarity, the domain network is truncated to show only 4 molecules (out of the 11-13) along the domain boundaries.

3.2.4 Determination of Nucleation Density

Molecular adsorbates generally show a pattern in the submonolayer region. At ambient temperature, a minimum coverage is needed to trigger island formation. On increasing coverage, the islands grow until they cover the entire surface. Critical nucleation density, defined as the surface coverage at which deposited adsorbates start to nucleate and aggregate into islands, is an important reference for the evaluations of inter-adsorbate interaction versus adsorbate-substrate interaction. For

systems with strong adsorbate-adsorbate attractive interaction, molecules on the surface start to aggregate into compact islands with very low critical nucleation density, such as C_{60} and C_{70}. On the other hand, some organics have very high critical nucleation density, ordered structures only form when the coverage is beyond 0.9 ML, such as CuPc and SnPc.[148] High critical nucleation density implies a strong repulsive interaction between the adsorbates, becoming attractive only after the critical point. We have used the concept of "critical nucleation density" to rationalize the interaction between TiOPc in each phases. In the following text, we are going to describe how this number is obtained experimentally.

STM images of honeycomb monolayer formation (Fig. 3.16) are used to determine the critical coverage for honeycomb island nucleation. The spatially average coverage (θ_{Tot}) is first estimated for each image by assuming a coverage-independent sticking coefficient. From the 480 s time required to reach the full monolayer in Fig. 3.16d, where $\theta_{Tot} = \theta_{HC} = 1.0ML$, here we define 1 TiOPc molecule per 24 surface Ag atoms, and we find average coverages for Fig. 3.16a ($\theta_{Tot} = 0.18ML$), Fig. 3.16b ($\theta_{Tot} = 0.38ML$) and Fig. 3.16c ($\theta_{Tot} = 0.63ML$). The critical coverage for island nucleation may then be determined from Fig. 3.16c by applying the lever rule: $f_g\theta_g + f_{HC}\theta_{HC} = \theta_{Tot}$, where f_g and f_{HC} represent the fractional surface area covered by the 2-D gas and the honeycomb phase, respectively; θ_g and θ_{HC} represent the local monolayer coverage of the 2-D gas and honeycomb phase, respectively; and θ_{Tot} represents the spatially averaged monolayer coverage. When honeycomb islands nucleate (Fig. 3.16c), the fractional area of the honeycomb phase is 0.3, while that of

the 2-D gas is $f_g = 1 - f_{HC} = 0.7$. Based upon the average coverage, $\theta_{Tot} = 0.63ML$, θ_{HC}=1.0, we determine θ_g=0.47. This coverage of the 2D gas phase in equilibrium with ordered TiOPc islands is the critical coverage for honeycomb island nucleation from a 2D molecular gas.

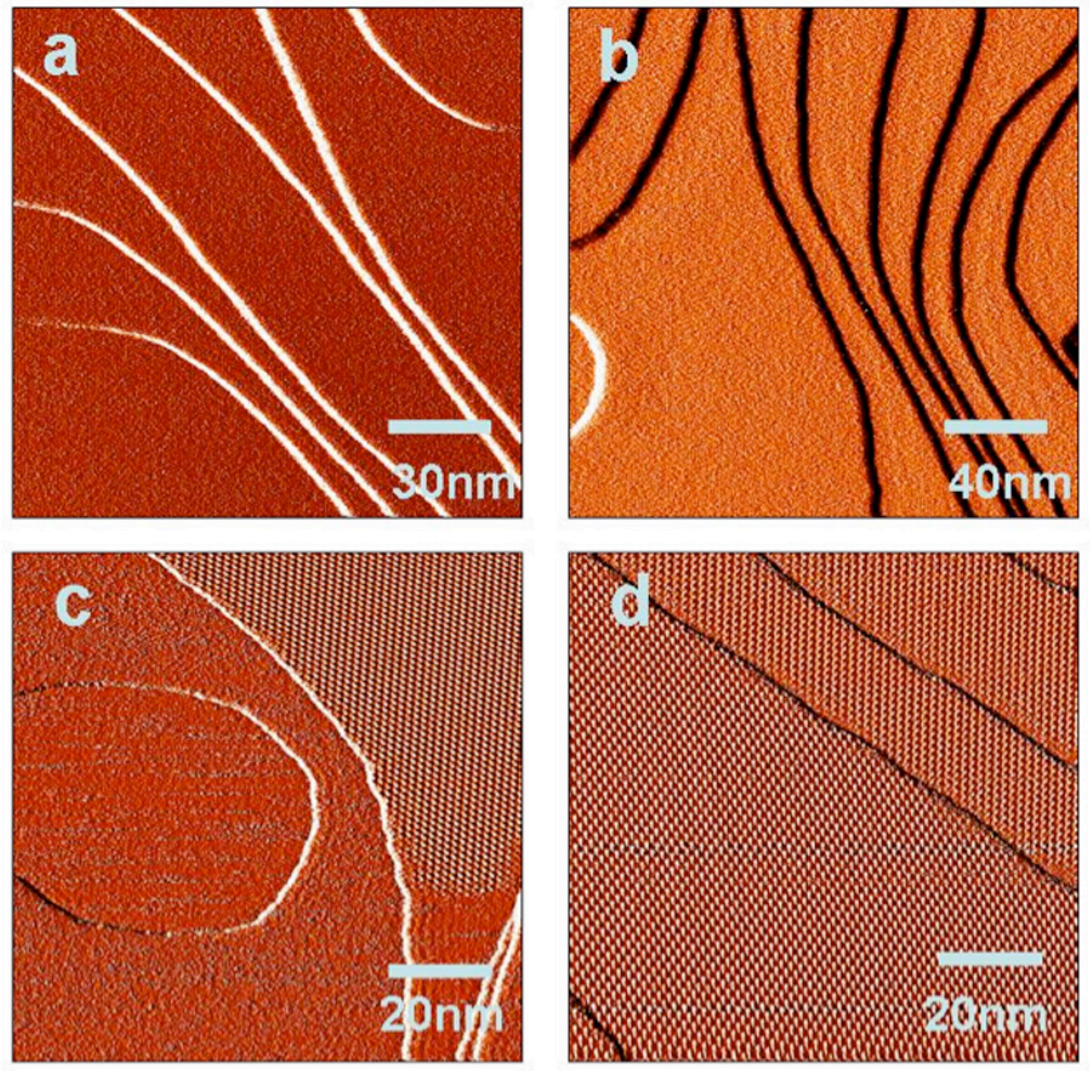

Figure 3.16 Coverage-dependent growth of the TiOPc honeycomb monolayer phase (a) 90 seconds deposition, no ordered structures are observed. Surface covered by 2-D molecular gas. (b) 180 seconds deposition, no ordered structures emerge, indicating increasingly dense 2-D molecular gas (c) 300 seconds deposition, honeycomb islands (upper right corner) nucleate and coexist with 2-D molecular gas (d) 480 seconds deposition, full monolayer of honeycomb phase TiOPc develops.

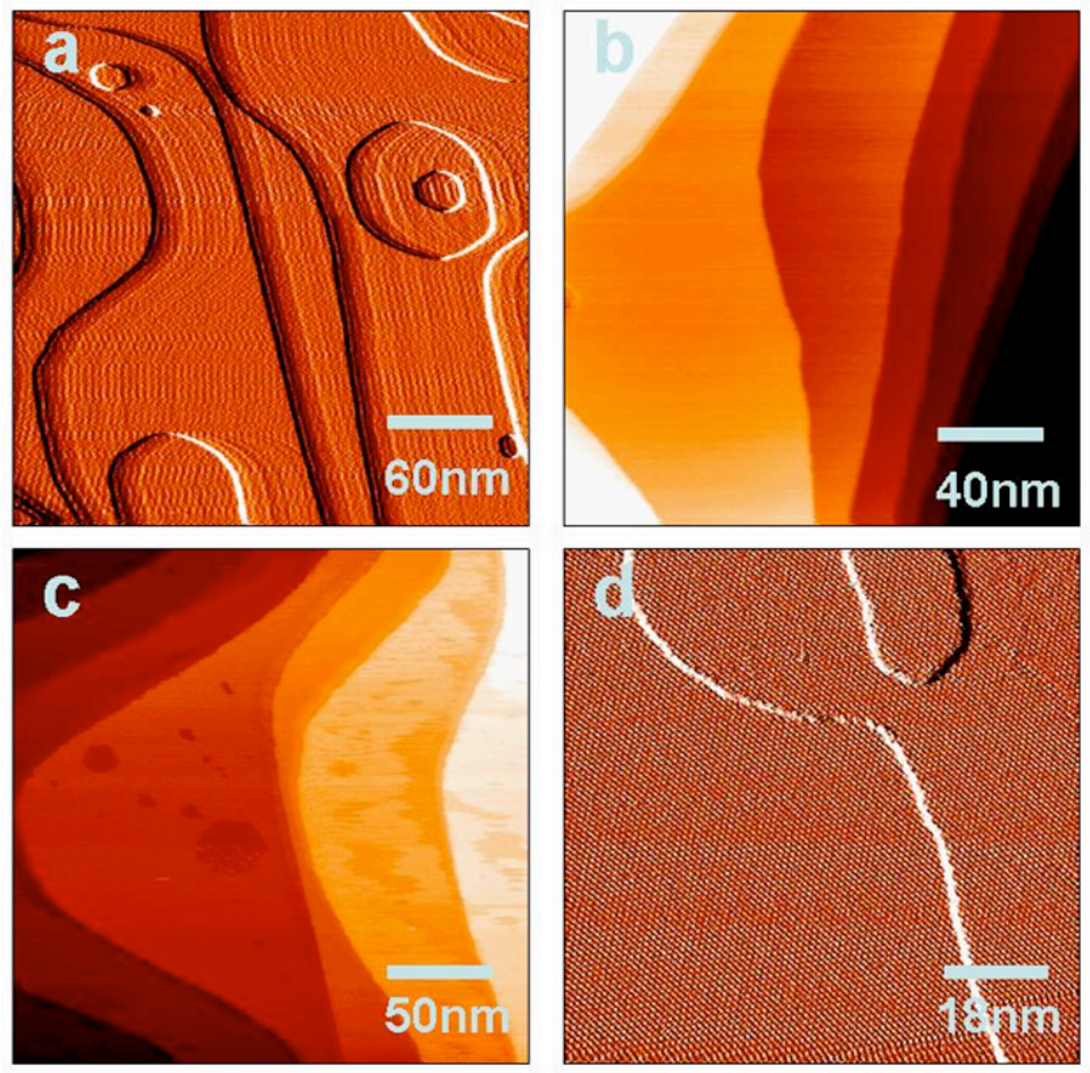

Figure 3.17 Coverage dependent growth of the TiOPc hexagonal monolayer phase: (a) 90 seconds deposition, no ordered structures can be observed. Surface is covered by 2-D molecular gas (b) 180 seconds deposition, no apparent ordered structures can be observed. Surface is covered by 2-D molecular gas of increasing density(c) 300 seconds deposition, ordered hexagonal islands of TiOPc appear on Ag terraces in coexistence with the 2-D gas phase (d) 360 seconds deposition, full monolayer of the hexagonal phase TiOPc formed.

STM images of the hexagonal monolayer formation (Fig. 3.17) are used to determine the critical coverage for hexagonal island nucleation, by application of the lever rule as described above. From the Fig. 3.17c image, where $\theta_{Tot} = 0.83ML$ and $f_g = 0.25$, we determine the critical coverage for the hexagonal phase nucleation as

$\theta_{g,Hex}$ =0.32 ML. Using the following equation converts this coverage to the representation defined with respect to unfilled honeycomb phase:

$$\frac{\theta_{\mathrm{g,hex}} \times \text{ Density of hexagonal phase}}{\text{Density of unfilled Honeycomb phase}} = \frac{0.32 \times 1.52^{-1}\,\mathrm{mol/nm^2}}{1.88^{-1}\,\mathrm{mol/nm^2}} = 0.40\mathrm{ML}$$

3.2.4 Summary

We have observed that deposition flux allows for the selective preparation of uniform TiOPc films that are thermodynamically stable (honeycomb) or metastable (hexagonal or hexagonal network). In these experiments, deposition flux selects both molecular architecture and registration with the substrate. Based upon DFT-calculated energies of TiOPc dimers, the energy difference between the hexagonal and honeycomb structures (neglecting the substrate) is estimated to be *ca.* 0.03 eV[149]. Because the energy difference between these adlayer structures is so small, the substrate must play a substantial role in selecting the honeycomb phase. A more complete theoretical calculation is necessary to evaluate the relative contribution of intermolecular interaction and molecule-adsorbate interaction in phase selection. However, a sense of this balance can be obtained by comparing adlayer structures on Ag(111) to those observed on other substrates. The molecular tilt angle provides a measure of the relative importance of chemisorption interaction relative to intermolecular interaction. Higher tilt angles generally indicate the greater importance of intermolecular interactions; a planar orientation generally indicates the greater importance of molecule-substrate interactions. On Au(111), TiOPc adopts a parallel orientation and a square unit cell of 1.4 nm, indicating domination by the TiOPc-Au interaction. In the case of the HOPG substrate, however, a hexagonal arrangement

with a unit cell of 1.3 nm is observed. This phase also appears as a metastable phase on Ag(111) and has a shallow tilt angle of ~30°, indicating increased contribution of intermolecular interactions relative to the molecule-substrate interaction. The greatest TiOPc molecular tilt angle, 40°, is observed in the thermodynamically stable honeycomb phase on Ag (111). The TiOPc-TiOPc interactions thus appear to be a more important factor in establishing monolayer film structure on Ag (111) than previously studied elemental surfaces. Nonetheless, the honeycomb phase is a commensurate structure on Ag (111), and the role of substrate interaction is thus significant. We have rationalized the adlayer structures on Ag (111) in terms of the electrostatic stabilization of the molecular films. The extent that the electrostatic properties of the molecular films are mediated by the dielectric properties of the substrate remains an open question.

Chapter 4 Model Molecular Hetero-interface TiOPc:C_{60}

Currently, there is great interest in the study of fullerenes with other small organic semiconductors as donor acceptor combinations[150-152], mainly because of their promising applications in organic electronics, including organic light-emitting devices, solar cells, field effect transistors and sensors[153-157]. A key strategy for the improvement of devices performance involves the optimization of chemical morphology at the interfaces of donor-acceptor heterojunctions for efficient charge separation. Understanding how to control the molecular architectures on the interfaces, particularly along crucial domain boundaries, is needed to realize these goals. However, a tendency of polymorphism in organic molecular crystals as well as surface supported thin films may put a limitation on these applications[19,20,158]. Polymorphs often differ only slightly in energy. In the previous chapter, we observed how monolayer phase selection is controlled by the substrate growth kinetics. In this chapter, we investigate polymorph response to the deposition of a secondary fullerene component, C_{60}. Careful characterization on the interfacial architectures grown from different polymorphs is crucial to understand how the interactions drive their formation and to achieve control over optimized film/crystal growth conditions.

We have shown in Chapter 3 that TiOPc can generate three distinct adlayer structures on Ag(111) selected by deposition flux, all of which are stable at room temperature[159]. This ability to selectively prepare TiOPc monolayer films with

different structures provides an opportunity to explore interface stability with respect to C_{60} co-deposition. From a technology perspective, C_{60}-TiOPc is also reported to have a higher energy conversion efficiency in OPV devices, which also makes this system important to study[51,151].

C_{60} has been deposited on various organic thin films to create multicomponent 1D or 2D interfaces[34,69,160-162]. The interfacial architecture is driven by a combination of thermodynamic and kinetic factors. In most cases, thermodynamic control has been the more common approach to design systems that self-assemble to form desired structures. The present work begins with different TiOPc monolayers on Ag (111) and tracks structural evolution following C_{60} deposition. The C_{60} deposition on these pre-engineered TiOPc films yields distinct structural motifs, ranging from phase-segregated domains with domain size dictated by the morphology (step density) of the growth substrate to a co-crystalline TiOPc $_{(2)}$ $C_{60\,(1)}$ honeycomb network, to a regular nanophase segregated domain network that is directly templated by TiOPc monolayer structure. We propose detailed structural models for the formation of each heterointerface and analyze their stability. In addition, we identify kinetic factors that underlie the formation of heterointerfaces.

4.1 C_{60} on Honeycomb TiOPc

Depositing of C_{60} on honeycomb TiOPc film immediately leads to phase segregation into C_{60} $(2\sqrt{3}\times 2\sqrt{3})\mathrm{R}30^{\circ}$ close-packed islands and TiOPc honeycomb islands, as shown in Fig 4.1a. Based upon the TiOPc honeycomb monolayer structure, determined by STM, the pore of the honeycomb (ca. 1.5 nm) is sufficient to accommodate a single C_{60} molecule (ca. 1.0 nm), as illustrated in Fig. 4.1c. However,

C_{60} do not occupy pore sites on the TiOPc honeycomb. Deposited C_{60} segregates instead to the Ag step edges, where they nucleate into $(2\sqrt{3}\times 2\sqrt{3})R30^{\circ}$ 2-D close-packed islands. The surface area for the growing C_{60} islands is created by the shrinking of the TiOPc islands. As shown in Fig. 4.1a, an irregular 5~10 nm gap is observed between the C_{60}, TiOPc domains. On some occasions, isolated C_{60} can be imaged in the honeycomb pores (Fig. 4.1b), but they are easily displaced by the STM tip during consecutive scanning, indicating that they are interacting very weakly with the pore sites as well as the TiOPc layer.

Simple geometric factor is excluded due to the smaller size of single C_{60} relative to the pore. As discussed in Chapter 3, the TiOPc honeycomb structure is composed of two sets of interlocked TiOPc molecules, shown in Fig. 4.1c. Six molecules with alternative orientation constitute the honeycomb frame, which are the main features in the STM image. In addition, the pores of the honeycomb contain another set of TiOPc forming a hexagonal lattice. The pore molecules don't have a fixed orientation, thus leading to varying shapes in the STM images. The absence of C_{60} molecules from the TiOPc pore indicates that these are repulsive sites. Evidently the electrostatic interaction between the TiOPc pore molecule and C_{60} is repulsive in this geometry. We note that the pore TiOPc molecules are more weakly bound to the Ag surface relative to the honeycomb skeleton. Nonetheless, the C_{60} diffusing over the TiOPc honeycomb do not displace TiOPc from the pores. Instead, deposited C_{60} displace TiOPc from the island edges. Without considering the pore molecule, each molecule in the honeycomb network is stabilized by its three nearest neighbor and is estimated to be about 40° tilted from the Ag surface. Removal of one TiOPc, as shown in the

model by the solid arrow, reduces the stability of 2 additional frame TiOPc and a pore TiOPc molecules. At room temperature, the displaced TiOPc must migrate to the 2nd layer. These second layer TiOPc are mobile at room temperature, and are sensed indirectly as tunneling noise. Thermal annealing desorbs this 2nd layer TiOPc, improving image quality.

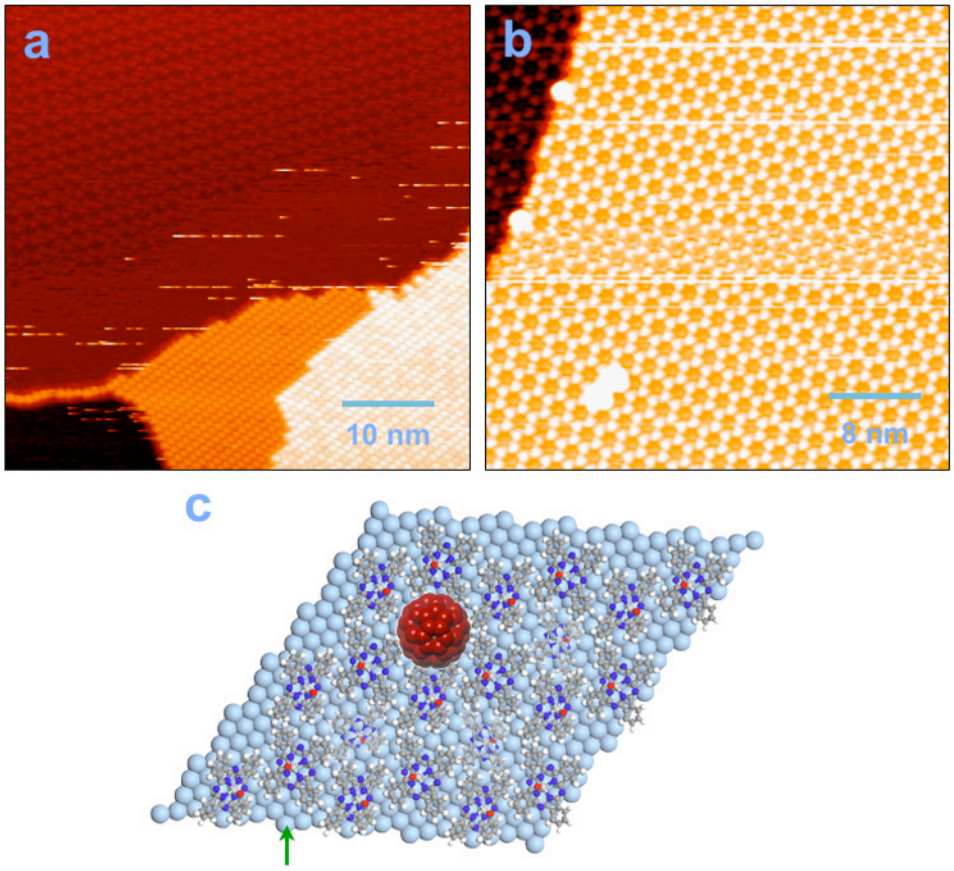

Figure 4.1 (a) Molecular resolved STM image of phase segregated TiOPc honeycomb island (upper left) and C_{60} (lower right) (+0.6V, 0.7pA) (b) High resolution STM image of isolated C_{60} on honeycomb pore sites (+0.65V, 0.6pA) (c) Proposed molecular packing model of filled honeycomb structure, drawn proportionally to compare the pore dimension with a single C_{60}. Pore TiOPc do not have defined orientations.

4.2 C_{60} on Hexagonal TiOPc

Depositing C_{60} on the hexagonal TiOPc film results in completely different growth patterns. Film structures obtained with increasing C_{60} coverage are shown in the STM images Fig. 4.2a-c. Upon deposition of 0.2 ML of C_{60} on the hexagonal TiOPc film, Fig. 4.2a reveals the formation of short disordered chains and small clusters in the vicinity of Ag(111) steps. The apparent heights of these C_{60} are almost identical to those of hexagonal C_{60} islands formed on bare Ag (111) surfaces, indicating that they are directly adsorbed on the Ag surface. The distance between C_{60} molecules in these structures is estimated to be 1.0nm, which equals that of close-packed C_{60}.

With increasing C_{60} coverage, a nascent TiOPc-C_{60} cocrystal structure is observed along the interfaces between these segregated structures, as circled in green in Fig. 4.2b. Within the cocrystal hexagonal lattice, the C_{60} adopt a ca. 2.1nm spacing, and the apparent height with respect to the Ag(111) is 0.5nm, which is similar to that of the close-packed C_{60} in the same image. Consequently, C_{60} within this co-crystal hexagonal phase is still bonded to Ag(111) surface.

The growing TiOPc-C_{60} cocrystal phase induces the formation of a mosaic pattern within the remaining hexagonal TiOPc phase. This is evident in Fig. 4.2 b and its inset. We have observed that the left hand domain is shifted by about 0.7 nm with respect to the right hand domains and these two domains have opposing TiOPc orientation. Notably, no such domain boundary is observed for the TiOPc hexagonal phase before the adsorption of C_{60}.

Upon further deposition of C_{60}, the TiOPc-C_{60} cocrystal structure grows into 2-D islands. From the protocol (C_{60} deposition on hexagonal TiOPc), the TiOPc-C_{60}

cocrystal island size is self-limiting at about 50% of the surface area. A combination of C_{60} close- packed islands and dense disordered TiOPc molecules occupy the remaining surface area, as shown in Fig. 4.2c. The size of each domain is limited within a characteristic length of 15 to 20 nm. Subsequent C_{60} deposition leads to 3-D film growth, with C_{60} aggregating above the hexagonal close-packed C_{60} domains on the monolayer. With a mild annealing (400K), multilayer C_{60} desorbs from the surface and while multi-phase TiOPc-C_{60} monolayer remains stable.

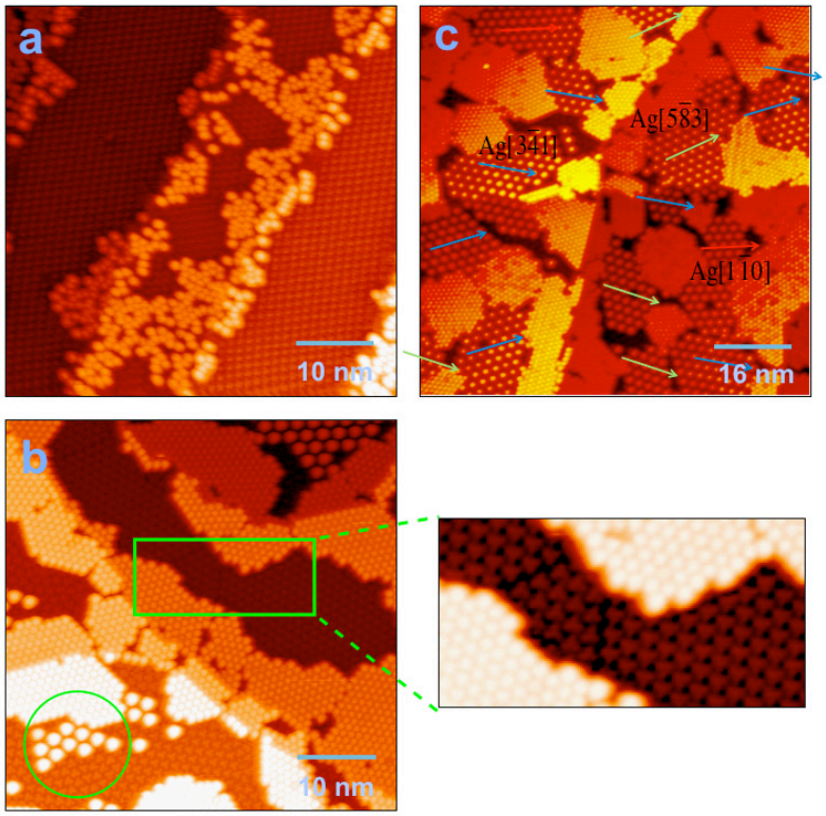

Figure 4.2 Molecular resolved STM image of C_{60} adsorption on hexagonal TiOPc film with increasing C_{60} coverage. (a) Θ_{60}= 0.2 ML, C_{60} nucleate on Ag step edges as well as narrow terraces, small clusters and short chains form. (-0.6V, 0.2pA) (b) Θ_{60}=0.4ML reveals the formation of a new diluted C_{60} structure, circled in green. In the magnified image on the right, formation of domain boundaries and orientation flip of TiOPc inside different domains are shown. (-0.6V, 0.6pA)(c) Θ_{60}=0.6ML, the surface is saturated with a combination of C_{60} closed packed islands, C_{60}-TiOPc cocrystal phase, and remaining dense disordered TiOPc. Three exclusive azimuthal angle of C_{60}-TiOPc cocrystal structure are indicated with color arrows. (+0.6V, 0.6pA).

Several structural features are noted for this TiOPc-C_{60} multiphase:

(1) The TiOPc-C_{60} cocrystal phase adopts three azimuthal orientations with respect to Ag(111), as shown in colored arrows in Fig. 4.2c. For the TiOPc-C_{60} along $\mathrm{Ag}[3\bar{4}1]$, the length of the unit cell is 20.8 Å, whereas along $\mathrm{Ag}[1\,\bar{1}0]$ and $\mathrm{Ag}[5\bar{8}3]$, the TiOPc-C_{60} cocrystal unit cell length has a smaller value of 20.2 Å. Analysis of the TiOPc-C60 cocrystal islands identifies Ag[$3\bar{4}1$] as the dominant direction (~40%), followed by $[5\bar{8}3]$ (30%), and $\mathrm{Ag}[1\,\bar{1}0]$ (30%).

(2) The segregated TiOPc and C_{60} domains are molecularly abrupt with no gap between the domains. The molecular density in this disordered area is estimated to be 6% higher than that of the hexagonal TiOPc. The TiOPc-C_{60} interfaces thus are formed in dynamic processes balanced between intermolecular interaction between the two components and the modulation from Ag substrate.

Additional structural details for the cocrystal phase are shown in the high resolution STM image Fig. 4.3. The initially formed isolated TiOPc-C_{60} cocrystal structure (Fig. 4.3a) as well as vacancies (Fig. 4.3b) reveals the local TiOPc molecular arrangement. Indicated by the green triangulars, six TiOPc molecules with alternative orientations arranged in pinwheel style surround each C_{60}. Ironically, this pinwheel arrangement is the same frame structure as that of the TiOPc honeycomb phase. Indeed, even the lattice constants in these structures are almost identical.

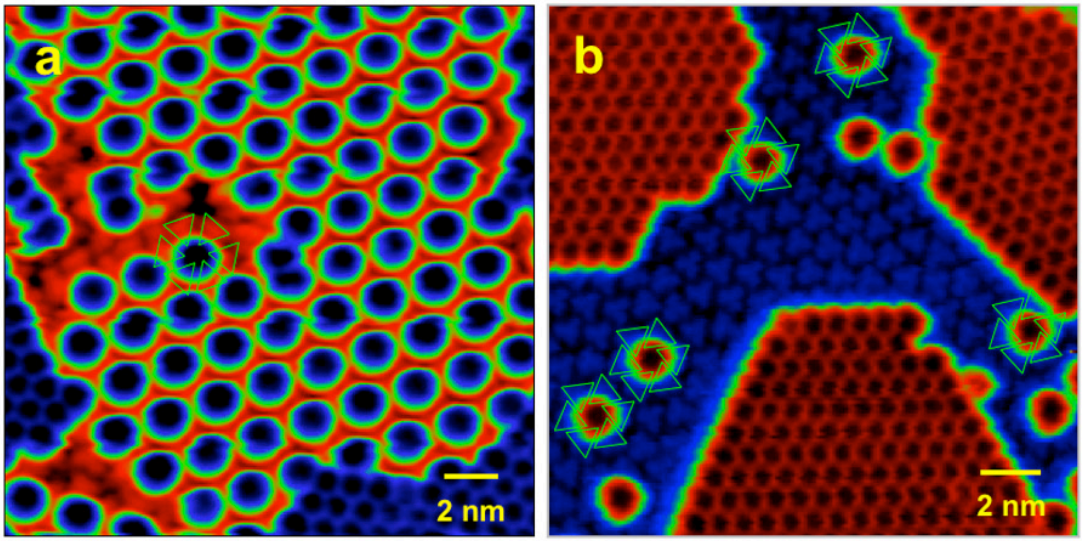

Figure 4.3 High-resolution STM images to reveal TiOPc structures around one C_{60} at the initial stage (left) and vacancies in "dilute TiOPc-C60"cocrystal phase (right)

The mechanism for interface formation between C_{60} and TiOPc films depends directly upon TiOPc monolayer structure. These differences reflect the stability difference of the TiOPc monolayer phase. For the less stable hexagonal TiOPc film, there is a greater abundance of vacancy defects. Those defects, together with Ag step edges, provide nucleation sites for C_{60}. A single missing TiOPc molecule in the hexagonal phase can accommodate 2-3 C_{60} molecules as sketched in Fig. 4.4c. Once these C_{60} nuclei form, subsequent C_{60} easily expand their cocrystal islands by displacing TiOPc from neighboring sites. The strong C_{60}-C_{60} interaction and greater adsorption energy on Ag support this displacement.

As discussed in Chapter 3, TiOPc has three polymorphs with only a moderate energy difference. The metastable hexagonal phase is mainly stabilized by electrostatic intermolecular interactions. Each TiOPc is estimated to be 30° tilted with respect to Ag surface. Estimated from their desorption temperature on Ag(111)

surface (700K for C_{60} and 450K for TiOPc), the adsorption energy of a single TiOPc is smaller compared with that of C_{60} on Ag. Moreover, removal of one TiOPc permits replacement by 2-3 C_{60}, making C_{60} adsorption much more favorable on an energy-per-area basis. With increasing surface coverage, the disordered C_{60} features grow into isolated 2-D close-packed islands, leading to disordered TiOPc on their interfaces. How do the TiOPc molecules along the C_{60} boundary respond? We surmise that each tilted TiOPc can locally adjust its orientation, tilt angle and position to minimize the total energy and continue to accommodate C_{60}. The metastability of hexagonal TiOPc under C_{60} adsorption thus leads to a stable multiphase structure. This includes the formation of a new TiOPc-C_{60} cocrystal phase on the interfaces, where growth is limited by the persistence of C_{60} close packed islands, and densely packed disordered TiOPc molecules.

Next we present a "nucleation and growth" scenario to describe the molecular events that lead to the TiOPc-C_{60} cocrystal structure. In Fig. 4.4 and 4.5, a single TiOPc is represented by a single triangular, the blue side is assigned to the two phenyl rings of a tilted molecule, and the red side represents the TiO group of this molecule.

Suppose a C_{60} assumes one vacancy site of the hexagonal phase. This C_{60} induces the surrounding TiOPc molecules to readjust their orientations and positions and form a honeycomb structure with C_{60} at the center. As shown in Fig. 4.4b, this involves a rotation of the molecule with respect to its internal symmetry axis (perpendicular to the surface), and a translation movement along the Ag surface. To grow into 2D islands with a specific azimuthal direction and unit cell, TiOPc molecules must

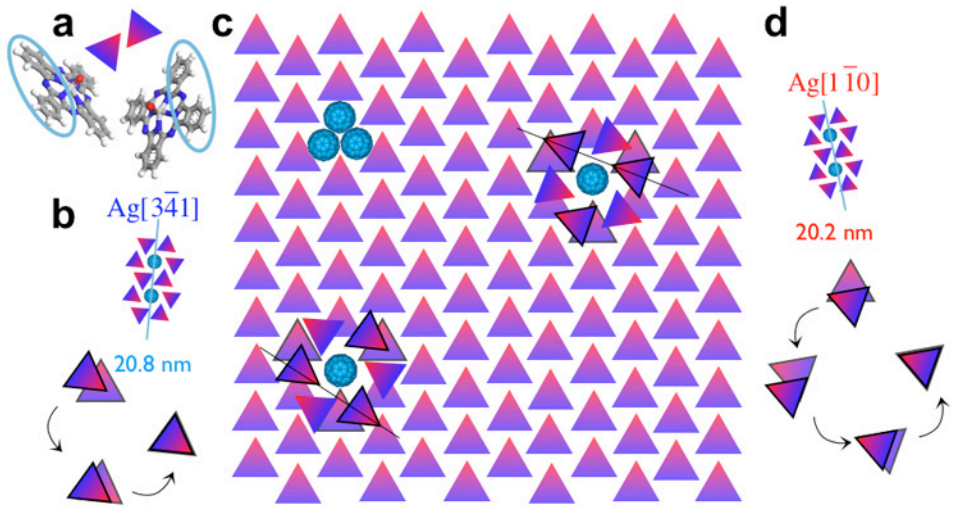

Figure 4.4 Structural models for the rearrangements of hexagonal TiOPc films with C_{60} coadsorption. (a) Each triangular in the model represents a tilted TiOPc molecule, the blue side corresponds to two phenyl rings and the red end represents the TiO group. (b) Schematic representation of the rotational and translation displacement of undisturbed TiOPc to its cocrystal structure with C60 along $Ag[3\bar{4}1]$ direction. (c) Rearrangement to honeycomb TiOPc structure, accompanying by co-adsorption of the center C_{60} molecule (d) TiOPc rearrangement along $Ag[1\,\bar{1}0]$ direction.

undergo different rotations and translations. To nucleate $[1\,\bar{1}0]$ directed and $[5\bar{8}3]$ directed honeycombs, the first six TiOPc molecules must undergo greater adjustment to form a unit cell at 20.2 Å, than for the $[3\bar{4}1]$ directed honeycomb (20.8 Å). Nucleation of the cocrystal structure must create space for next nearest TiOPc adjustment to form the next honeycomb.

Following the honeycomb co-crystal nucleation event, Fig. 4.5 shows the continued "chain" growth process. Hexagonal film defects and Ag step edges serve as nucleation sites that induce more defect sites. The typical interfacial architecture, shown in Fig. 4.5, composed of cocrystal TiOPc-C_{60}, close packed C_{60} and dense disordered TiOPc is thermally stable because no more sites are available for further C_{60} adsorption and the mass transport pathways are blocked. This also explains why

this TiOPc-C_{60} cocrystal structure is limited in size and cannot cover the whole surface. When the rest of surface is covered with disordered high density TiOPc, the TiOPc are prohibited from adjusting their orientation, and cannot be displaced by C_{60}.

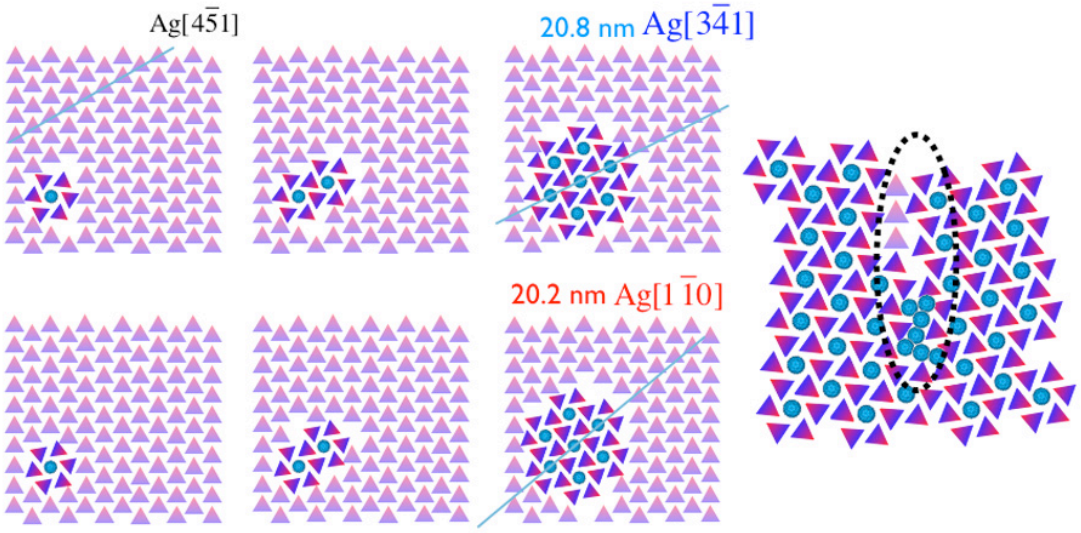

Figure 4.5 The evolution of TiOPc-C_{60} honeycomb structures along different directions (left), and the typical interfacial architecture constituted of disordered TiOPc, small patch close packed C_{60} following this process (right).

In addition to the TiOPc-C_{60} cocrystal structure, TiOPc domains with oppositely orientated molecules on boundaries and half unit cell offset are generally observed on Ag terraces. Such domain boundaries, reminiscent of the TiOPc triangular network, provide alternative sites for C_{60} adsorption and nucleation of the honeycomb TiOPc-C_{60} cocrystal phase.

The TiOPc arrangement is a dynamic process driven by the "push" of TiOPc-C_{60} cocrystal network formation. This nucleation and growth model is strongly supported by the inability to generate this cocrystal honeycomb from the pure TiOPc honeycomb. Moreover, we have prepared neat honeycomb TiOPc without the pore molecules with a compressed unit cell, and the empty honeycombs undergo a phase

transition to the hexagonal phase at room temperature, shown in Fig. 4.6a-d. The TiOPc-C_{60} cocrystal structure is energetically stabilized by the tendency of TiOPc to form stable honeycomb structures, and also the high adsorption energy of C_{60} on Ag substrate.

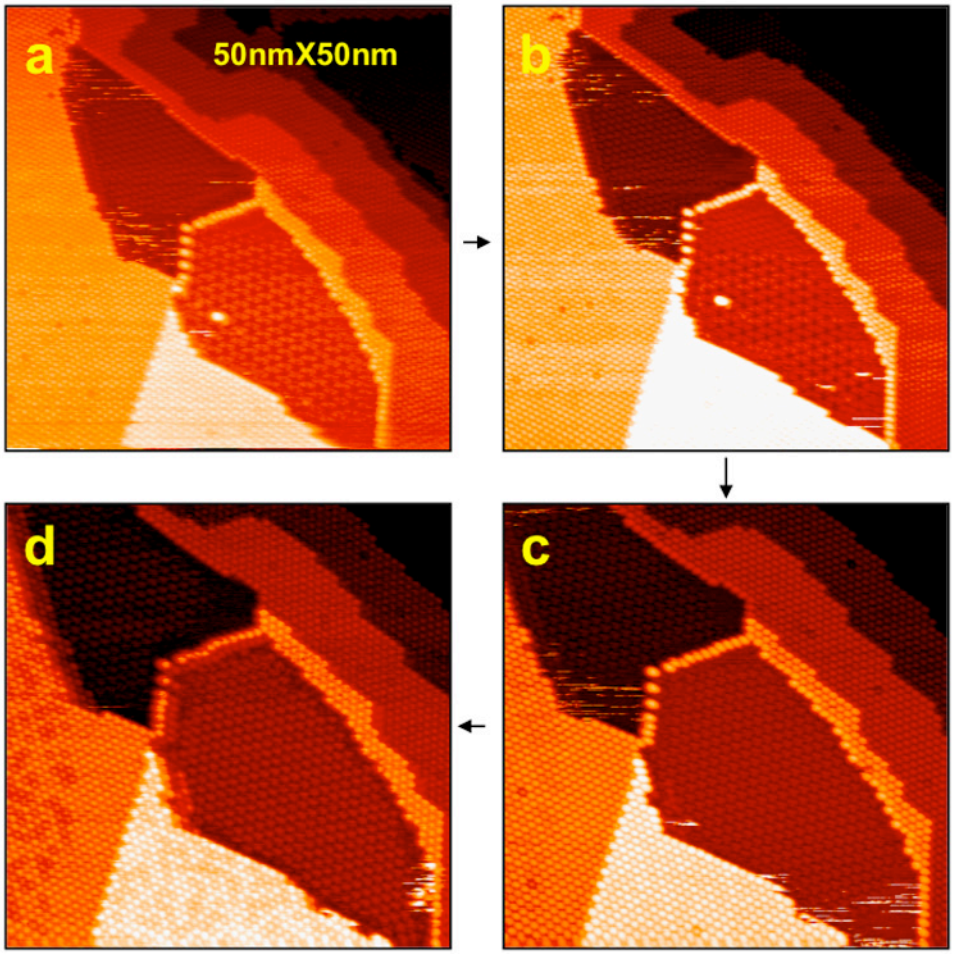

Figure 4.6 Phase transition from unfilled honeycomb TiOPc to hexagonal TiOPc with successive STM images. (a) Lower right, confined area of honeycomb TiOPc structure with single C_{60} on top (b) The top part of the honeycomb domain changed to hexagonal structure. (c) The whole honeycomb domain transits to hexagonal structure with streaks showing mobile molecules. (d) Stable hexagonal TiOPc domain without streaks.

Reversed-deposition-sequence experiments were also carried for this system. On the $(2\sqrt{3}\times 2\sqrt{3})R30^\circ$ C_{60} monolayer structure, TiOPc has a high mobility and does

not form either ordered structure at room temperature. Individual TiOPc with hindered rotation is observed on the C_{60} layer, and this is similar to the case of single CuPc on C_{60} previously reported[163]. For partially C_{60} occupied Ag (111) surface, the sequentially deposited TiOPc either form honeycomb phase or hexagonal phase depending on the flux chose, both of which are segregated with the preoccupied C_{60} islands. However, upon long time annealing, very limited diluted C_{60}-TiOPc cocrystal phase is observed on the interface of C_{60} close packed islands and hexagonal TiOPc. On the whole, C_{60} and TiOPc are phase segregated when C_{60} initially occupy part of the surface area.

Finally these results are compared to the well-studied phthalocyanine-C_{60} system[163-165]. At room temperature, CuPc form an ordered structure with a quadratic unit cell on Au (111). When deposited sequentially with C_{60}, they "demix" from C_{60} closed packed islands with a dense but irregular pattern, where single CuPc molecules are resolved. No single C_{60} is found within CuPc domains. However, single C_{60} or linear cluster with 3-5 molecules decorate on CuPc domain boundaries. This is similar to our results for C_{60} hexagonal TiOPc films, except the formation of the cocrystal structure with TiOPc. We note that CuPc adopts a planer orientation that may limit the readjustment of CuPc upon C_{60} deposition thus preventing the kinetic formation of cocrystal Pc-C_{60} structure. Moreover, this planer adsorption geometry indicates a higher adsorption energy, and CuPc molecules may not be so readily displaced.

Kinetically controlled co-adsorption of organic molecules with fullerenes is widely reported. Xu et al. have shown that using co-adsorbed fullerene on different coverage

acridine-9-carboxylic acid (ACA) on Ag (111) can cause the formation of different intermixed structures depending on the balance between C_{60}-ACA-Ag (111) interactions[69]. Nishiyama et al. reported the interstitial accommodation of the C_{60} into trans-BCaTBPP (15-bis(4-carboxyphenyl)-10,20-bis(3,5-di-t-butylphenyl) porphyrin) compact layer by inducing the local conformation change of the metalloporphyrin[161]. Compared with previous studies, we hereby demonstrate by starting from different polymorphs of organic material on metal substrate, i.e. TiOPc on Ag (111), the slight energy difference in the unitary system can be magnified by co-adsorption of a second molecular species. Induced local molecular rearrangements help not only the accommodation of the second adsorbate but also the formation of stabilizing interfacial areas, which reduces the total energy. A complete theoretical calculation incorporating Ag substrate and both of the adsorbates is necessary to evaluate the relative contribution of intermolecular interaction and molecular-substrate interaction in this dynamic process. However, a sense of this balance can be obtained by comparing the adsorption energy of MPc molecules and fullerenes on Ag, as well as their intermolecular interactions. C_{60} has higher adsorption energy on metal surfaces (~2eV[107,108]) than that of TiOPc. So C_{60} adsorbed on Ag surface would have a strong tendency to contact with the metal surface directly, thus causing partial desorption of TiOPc. On the other hand, TiOPc have a tendency to maximize their intermolecular attraction by rearrange into the most stable honeycomb phase. Although the hexagonal TiOPc film is less stable than the honeycomb film in its unitary system, by co-adsorbed with C_{60}, a highly stable TiOPc-C_{60} cocrystal structure is trapped

kinetically. The interfacial structure for hexagonal-C_{60} is thus more stable than that of honeycomb-C_{60}.

4.3 C_{60} on Triangular Network TiOPc

We then test this dislocation structure as a nanotemplate for C_{60} assembly. First we note that C_{60} molecules can select from three types of surface sites: above the TiOPc triangular domains, along the domain boundaries (dashed lines in Fig. 4.7d) and at the intersection of six adjacent triangular domains (circle in Fig. 4.7d). Only at the latter intersection will the C_{60} molecules interact directly with the Ag (111) surface. At this domain intersection, the area of exposed silver surface is determined by the packing of TiOPc molecules. Ideally terminated domains (Fig. 4.7d) leave Ag region of 3 to 4 nm^2 that is sufficient to directly accommodate 3 close-packed C_{60} molecules. Many domains are not ideally terminated, missing 3-6 TiOPc molecules at the domain intersection. Such domain intersections (see Fig. 4.7b and 4.7c) expose bare Ag (111) regions with 8-12 nm^2 in area.

Deposition 0.2 ML C_{60} onto triangular TiOPc networks immediately results in the formation of ordered arrays of C_{60} nanoclusters (Fig. 4.8a). The spacing between C_{60} clusters is 14.0 ± 1.0 nm, corresponding to the characteristic dimension of each triangular TiOPc domain. Each C_{60} cluster is positioned at the intersection of six TiOPc domains. The topographic line profile of C_{60} and TiOPc structures (Fig. 4.8a dashed line), confirms that C_{60} molecules directly contact the Ag surface. Under room temperature imaging conditions, C_{60} clusters show dynamic structure variations on the 30 s timescale of STM image acquisition. As shown in Fig. 4.8b, clusters contain

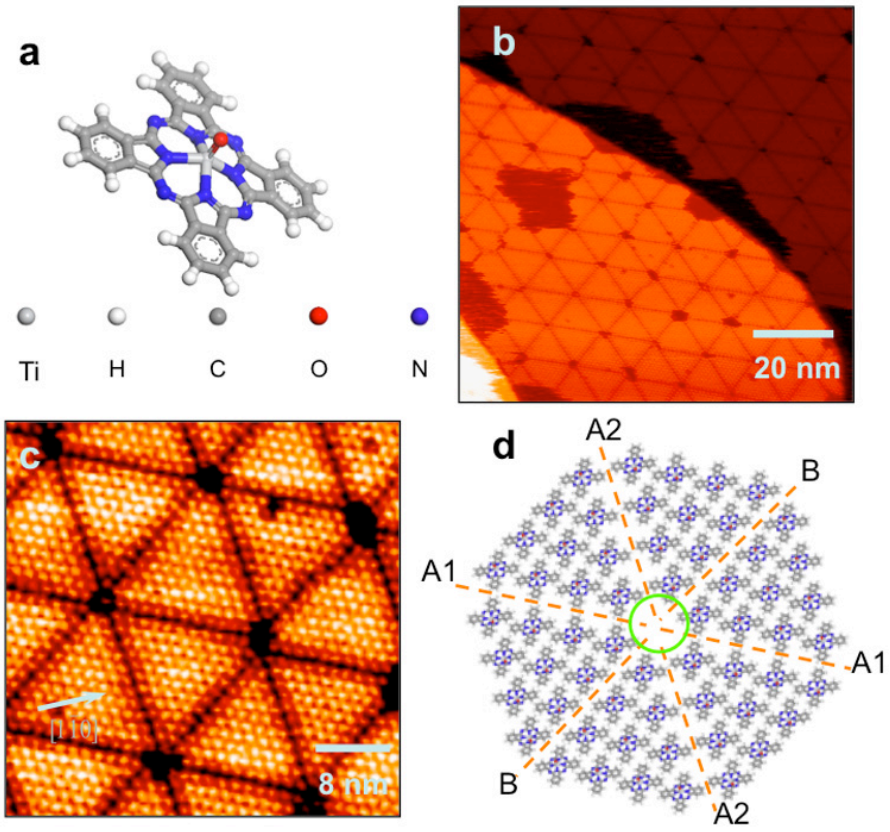

Figure 4.7 (a) Tilted view of the free TiOPc molecular. (b) STM image of TiOPc monolayer prepared by 0.4 ML/Min. Flux reveals a regular network of triangular TiOPc domains. (c) Molecularly resolved STM image of the triangular network. Each molecule is represented by a bright spot in the image. (d) Structural model for the triangular network. For clarity, the domain network is truncated to show only 4 molecules (out of the 11-13) along the domain boundaries.

a "core" of close-packed C_{60} molecules. The "rim" of the C_{60} cluster appears noisy in the STM images, indicating more weakly attached C_{60}. There are some variations in the size and shape of the clusters, with hexagonal clusters generally appearing more stable and easily imaged and elliptical clusters appearing somewhat less stable. This is consistent with C_{60}'s well-known hexagonal close packing, which energetically favors hexagonal-shaped clusters.

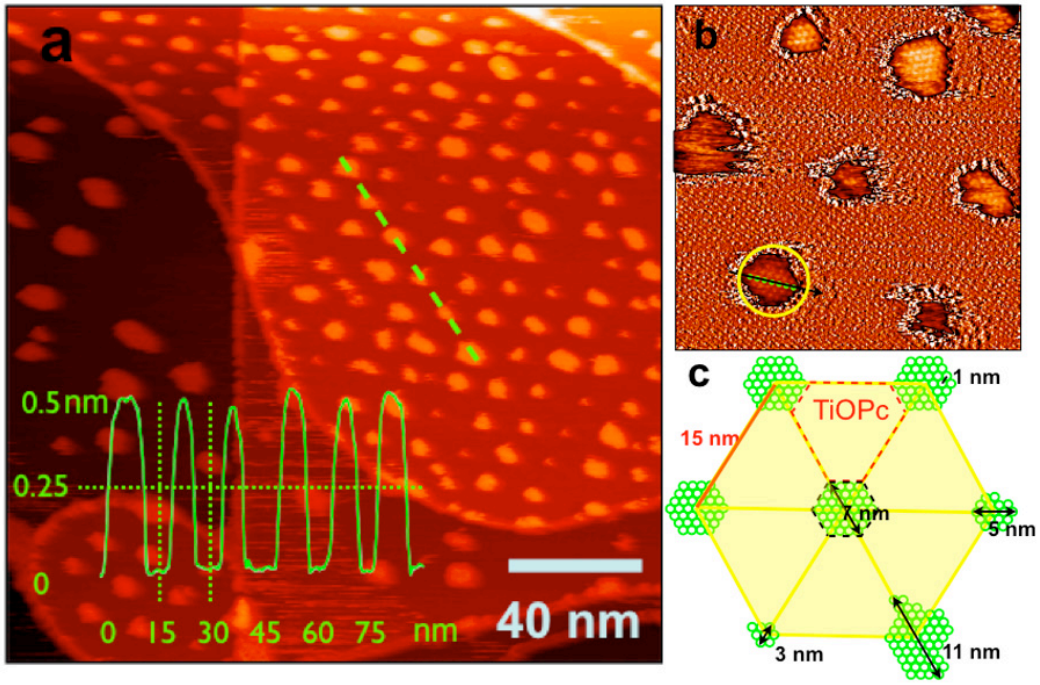

Figure 4.8 (a) Large scale STM image of C_{60} cluster array on TiOPc triangular dislocation networks. Inset is the line profile of the six C_{60} clusters along the dashed line. (b) STM image of C_{60} clusters shown as a differential image to enhance molecular resolution. (c) Size distribution of the diameter for C_{60} clusters, N represents the number of C_{60} molecules along the diameter. (d) Schematic illustration of the nanophase segregated C_{60} and TiOPc domains.

The C_{60} clusters thus occupy a quasi-periodic superlattice with a spread in cluster size. We quantify the size of an individual cluster by its diameter at the point of maximum width, as illustrated in Fig. 4.8b. A histogram of the C_{60} cluster width distribution, given in Figure 4.9, reveals a 7 ± 2 nm average cluster size and a 7 nm most probable size. Diameters of the C_{60} clusters span the 1~12 nm range, and are accommodated by the TiOPc network structure, as depicted in Fig. 4.8c. Effectively, both the C_{60} nanocluster and the TiOPc triangular domain must fit within the 15 nm repeat of the misfit dislocation network. The average 7 nm C_{60} cluster diameter leaves TiOPc domains of similar size. Consequently, C_{60} deposition on the TiOPc film template results in a pattern of nanophase-separated C_{60} and TiOPc domains with

characteristic domain size of 7 nm. We note that this 7 nm dimension is comparable to the exciton diffusion length in a molecular semiconductor. Achieving nanophase segregation of molecular semiconductors on this length scale is believed to be a crucial step toward improving the efficiency of small-molecule photovoltaic cells.

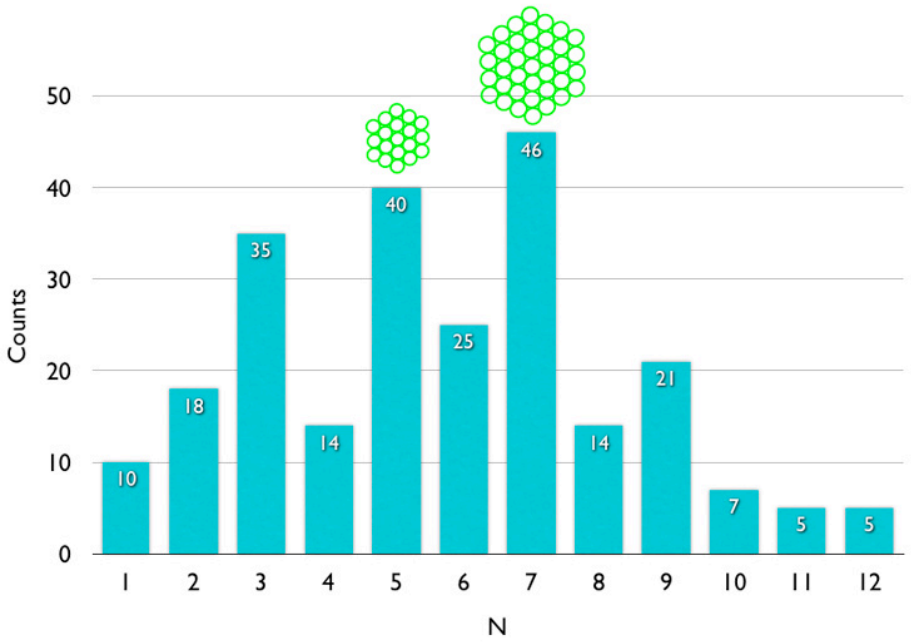

Figure 4.9 Size distribution of the diameter for C_{60} clusters, N represents the number of C_{60} molecules along the diameter. Observed size distribution of C_{60} clusters: The total number of clusters observed versus width N, where N is the number of C_{60} molecules along the cluster diameter. Each cluster diameters was evaluated from the STM topographic profile along the cross section of maximum width. A total of 240 clusters was analyzed (800 nm^2 surface area), revealing an average diameter of 7±2 nm, with the most probably diameter also 7 nm. A greater propensity for observing odd-N values is within the confidence limits of the available data. Smaller clusters (N=1,2) may be underestimated due to increased tip-sample perturbation. Close-packed C_{60} clusters, with corresponding N values, are shown schematically. The observed size distribution reflects the TiOPc vacancy size distribution in the TiOPc template and the relative stability of C_{60} clusters.

The resulted nanophase-separated TiOPc-C_{60} film structures are quite robust. Once C_{60} cluster arrays are formed on the TiOPc dislocation network, the binary film can be heated to 420 K without degrading the structure. In fact, this binary film structure is considerably more stable than the original TiOPc template, for which the dislocation network is removed by thermal annealing at temperatures of just 390 K.

4.4 Summary

In conclusion, we have shown that by selectively co-adsorption of C_{60} on different TiOPc films on Ag (111), three totally different interfacial architectures are observed in monolayer regime: ranging from nanoscale segregated phase with domain size dictated by the morphology (step density) of the growth substrate to a co-crystalline $TiOPc_{(2)}C_{60(1)}$ honeycomb network and a nanophase-segregated TiOPc-C_{60} on the scale of 10-20 nm, summarized in Fig. 4.10.

This diversity is attributed to the slight energy difference in three TiOPc polymorphs on Ag (111), which exposes the hexagonal TiOPc phase more sensitive to highly anisotropic external force induced by C_{60} co-adsorption. The hexagonal TiOPc film responds most dramatically to C_{60} deposition. The resulting structures are similar to the most stable honeycomb monolayer phase. The resulting multiphase structure is driven by the energy gain through the C_{60} occupation on Ag sites and the formation of a TiOPc honeycomb structure. The impact of these distinct interfacial architectures on the electronic properties will be further investigated in Chapter 6.

Phase separation of small semiconducting molecules, desirable for photovoltaic cells, is relatively easy to achieve. For TiOPc, the TiOPc honeycomb phase leads to phase separation. However, strategies for controlling domain size in the ~10nm length (limited to exciton diffusion length) are not well developed. Dislocations are important structural elements in crystalline materials that may be successfully harnessed for this lengthscale. Ultrathin metal films, for example, can form highly ordered arrays of dislocations to relieve the strain caused by the different lattice spacing between the metal films and the support.[166-169] Such misfit dislocation

networks have already served as structural templates for metal nanoclusters and organic SAMs.[170-172] In principle, these dislocation networks are not limited to metal films, but should be found also in thin molecular films with a suitable lattice mismatch to the substrate.

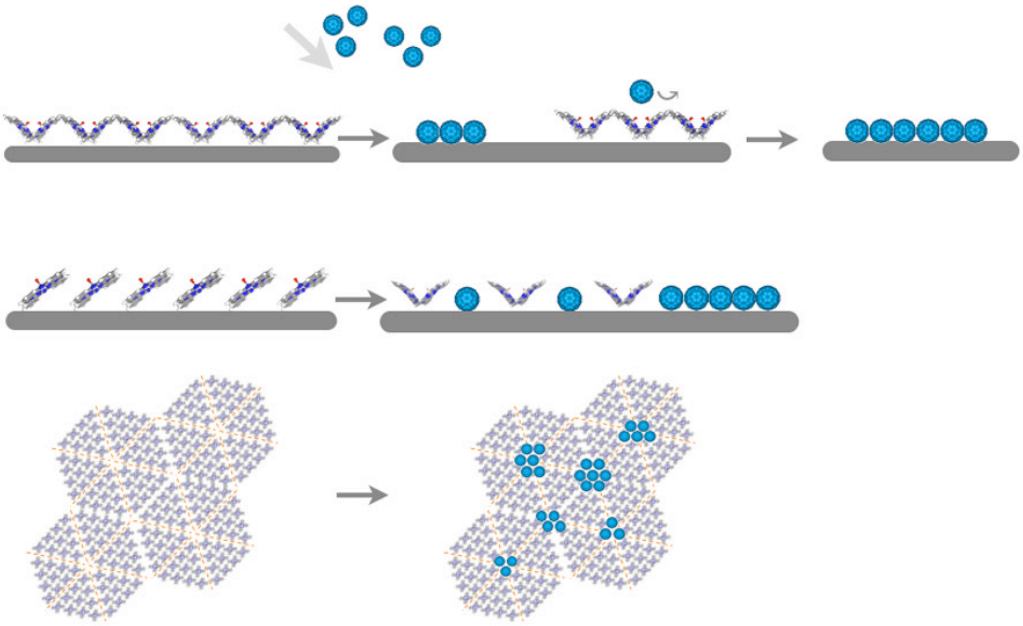

Figure 4.10 Schematic illustration of different C_{60}:TiOPc heterostructures with sequential deposition. (a) C_{60} on honeycomb TiOPc (b) C_{60} on hexagonal TiOPc (c) C_{60} on TiOPc triangular dislocation network.

Here we have used TiOPc, a molecular semiconductor with anisotropic interactions to generate a molecular film with a characteristic pattern repeat size of 15 nm. This structure then served as the nanotemplate for a superlattice of C_{60} clusters with characteristic diameters of 7 nm. As a result, C_{60} deposition on the TiOPc film template form a pattern of nanophase-separated C_{60} and TiOPc domains with characteristic domain size of 7 nm. Once the length scale of the phase separation is established by this method, it should propagate to some film thickness before

decaying. Studies to examine how well the templated phase separation can be maintained to multilayer films are currently being planned. Misfit dislocations in thin molecular films are a common phenomena[173,174] that can be more generally exploited for nanopatterning on the 10 nm length scale.

Chapter 5 Model Molecular Hetero-junction TiOPc:C_{70}

In Chapter 4, we have shown how TiOPc-C_{60} interface structure evolves from distinct TiOPc monolayer architectures. Increasingly C_{70} is replacing C_{60} in OPV devices, since the choice of C_{70} as an electron acceptor has demonstrated a significant 25% improvement in device efficiency[61,175,176]. Theoretical studies indicate C_{70} accepts more charge transfer from donating oligomers[4], in comparison with C_{60}. These findings stimulate us to investigate TiOPc-C_{70} heterostructures in order to identify key structural and/or electronic differences from TiOPc-C_{60} heterostructures.

The C_{60} and C_{70} fullerenes have distinct physical properties that will influence interface formation. Perhaps the most significant difference in these molecular species is the distinct polarizability, which is derived from their distinct shapes. As described in Chapter 3, C_{70} polarizability is 25% greater than that of C_{60}. Moreover, C_{70} polarizability is highly anisotropic, whereas C_{60} has a spherically symmetric polarizability. These differences, in combination with the electrostatic properties of TiOPc films, will produce significant differences in the heterostructures that are realized.

5.1 C_{70} on Honeycomb TiOPc

The electrostatic properties of TiOPc films are, of course, dependent on monolayer structure. Molecular TiOPc has a strong axial dipole moment 3 Debye. The honeycomb structure is compromised by two sets of interlocked TiOPc molecules,

tilted by ~40 degrees with respect to the surface. Six molecules with alternative orientation constitute the honeycomb frame. This structure possesses a net vertical dipole moment of 2.3 Debye/molecule. This TiOPc honeycomb contains another additional TiOPc molecule bound to the pore sites. Each pore contains one TiOPc molecule, oriented nearly parallel to the surface plane, with a net moment of ca. 3 Debye. Electrostatically, the TiOPc honeycomb monolayer presents a dipolar lattice with a symmetry that corresponds to the honeycomb lattice. This honeycomb dipole lattice is presented schematically in Fig. 5.1c, in which arrow length denotes relative dipole strength.

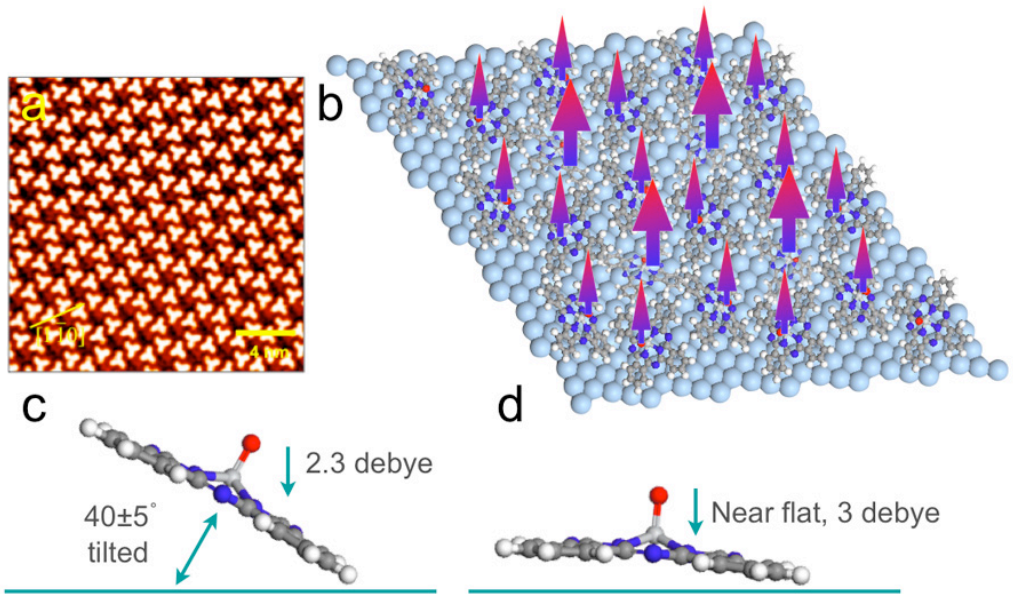

Figure 5.1 TiOPc honeycomb structure (a) Molecularly-resolved STM image of TiOPc honeycomb structure, acquired with a positive sample bias (0.7 V) and 0.05 nA tunneling current, and (b) Schematic illustration of the TiOPc honeycomb monolayer structure and the corresponding dipole lattice, where arrow length reflects the magnitude of the vertical dipole moment, and (c) Schematic illustration of the electrostatics of an individual TiOPc molecule inclined on Ag(111), and (d) Schematic illustration of the electrostatics of an individual TiOPc molecule flat on Ag(111).

In the following, we will explore the impact of this molecular dipole lattice on interface formation with C_{70}. We will grow C_{70} layer-by-layer on this TiOPc

honeycomb template and develop detailed structural models. The heterostructures that are developed involve C_{70} arrangement of unusually low density, demonstrating the TiOPc dipole layer exerts a long-range influence on the C_{70} growth patterns.

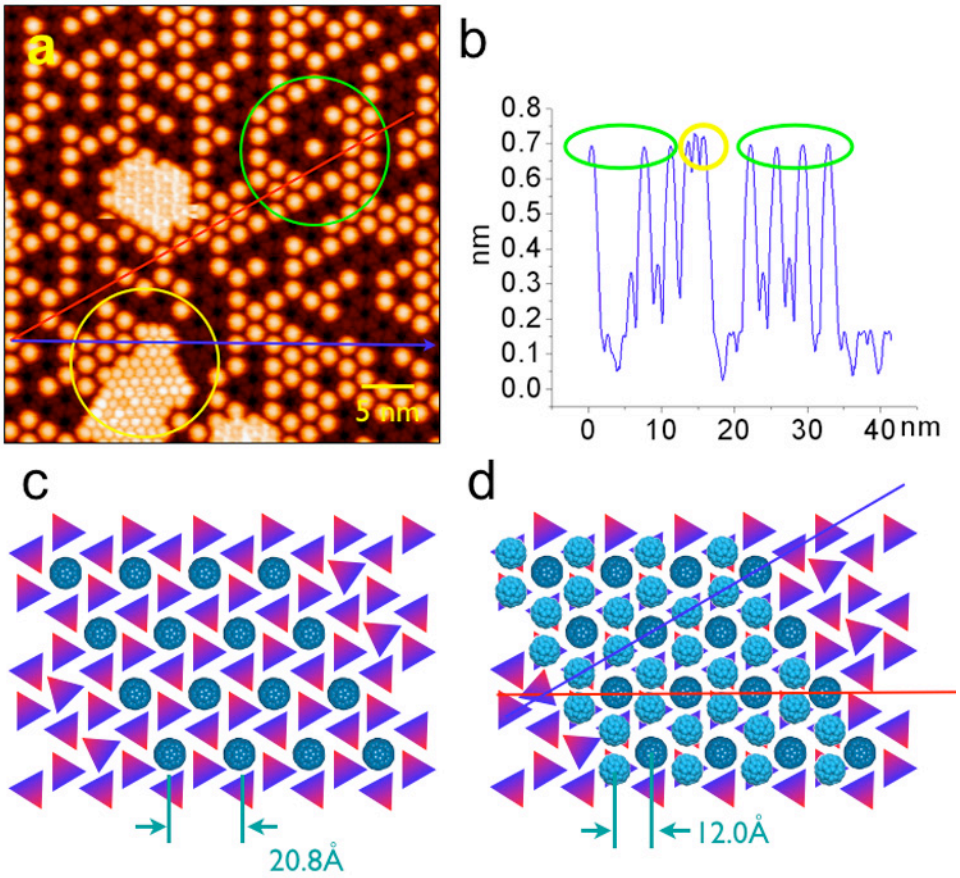

Figure 5.2 (a) STM image of first-layer of C_{70} deposited on the TiOPc honeycomb monolayer: Green circle denotes region where C_{70} are positioned directly above TiOPc pore molecules; Yellow circle denotes close-packed C_{70} structures that span the honeycomb. (b) Line profile along the blue solid line in (a) (c) Model depicts C_{70} occupation of sites over pore-TiOPc (green circle in (a)); (d) Model for C_{70} close packed structure (yellow structure in a). Dark blue C70 depict position above pore-TiOPc: Light blue depict position above frame TiOPc.

Initially deposited C_{70} first occupy sites above pore-TiOPc molecules. The nearest neighbor C_{70} - C_{70} distance, 20.8 Å, shown in Fig 5.2b (circled in green), corresponds to the pore-to-pore distance in the TiOPc honeycomb structure. With increasing TiOPc coverage, small areas of close-packed C_{70} (12 Å nearest-neighbor spacing) are

also observed on the surface, as circled in yellow in Fig. 5.2b. The underlying TiOPc honeycomb layer remains undisturbed by C_{70} deposition. The apparent heights of the two C_{70} structures, atop TiOPc-pore sites and the hcp islands, are very similar, as shown in Fig. 5.2b. Molecules in the close-packed island (yellow circle) appear ~0.3 Å higher than C_{70} above TiOPc-pore sites (blue oval). The slight difference in the apparent height is attributed to the different orientations of the TiOPc underneath as well as different electronic coupling between TiOPc and C_{70}. We note that the close-packed C_{70} islands align (blue line in Fig. 5.2a) with respect to the honeycomb lattice, which is highlighted by the C_{70} decoration of TiOPc-pore sites.

Based on these observations, a growth model for the first layer of C_{70} is developed, as shown in Fig. 5.2c. The TiOPc honeycomb layer remains fully intact. Pore-TiOPc sites (dark blue in Fig. 5.2c and d) are first populated, but at modest C_{70} coverage, C_{70} molecules (light blue ones in Fig. 5.2d) aggregate into close packed C_{70} structures that extend over both pore- and frame- TiOPc sites. The registration and dimension in the model are taken directly from STM observations. The small height difference between C_{70} molecules on pore sites and frame sites becomes obscured with increasing coverage. For simplicity, we use the terms "C_{70}-on-frame" and "C_{70}-on-pore" to represent C_{70} on different adsorption sites in the first layer.

To obtain independent information on the relative height of "C_{70}-on-frame" and "C_{70}-on-pore" molecules, we measured *z(V)* spectra above each featured C_{70}. As shown in Fig. 5.3, the red, green, and blue lines correspond to the unoccupied states of pure C_{70} on bare Ag(111), "C_{70}-on-frame", and "C_{70}-on-pore", respectively. The

almost indistinguishability of the *z(V)* spectra for "C_{70}-on-frame" and "C_{70}-on-pore" indicates that these C_{70} molecules are at comparable heights above the metal surface.

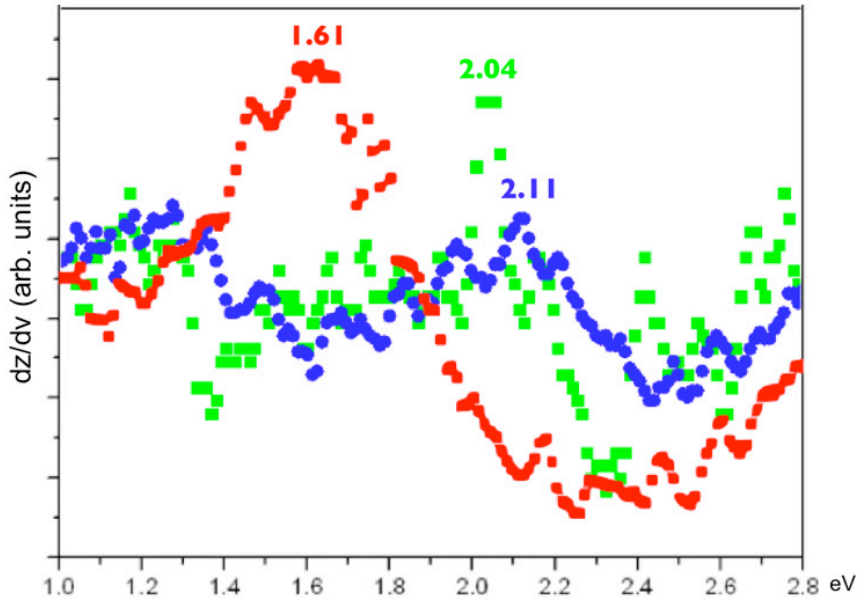

Figure 5.3 *z(V)* spectra taken for unoccupied states for C_{70} structures - Red: C_{70} / Ag(111); Green: C_{70}/frame-TiOPc; Blue: C_{70} /pore-TiOPc. Each spectrum represents an average of 20 individual traces, acquired at 0.03 nA tunnel current.

All *dz/dV* curves show one major peak, assigned to LUMO state of C_{70}. We use the spectra of C_{70} directly on Ag(111) as reference, following reported PES measurements on similar systems to make band assignments[114,177-180]. The shift of C_{70} LUMO upon direct deposition on Ag(111) indicates a charge transfer from Ag to C_{70}. Based upon these *z(V)* measurements, "C_{70}-on-frame" and "C_{70}-on-pore" are electronically distinct. In general, the LUMO level for C_{70} above a TiOPc monolayer remains far from the Fermi level. The "C_{70}-on-frame" LUMO is about 0.07 eV below that of "C_{70}-on-pore", reflecting the different electronic coupling between C_{70} and the underlying TiOPc molecule, as we will discuss in the following text.

We recall that individual C_{70} molecules have curved π surfaces, depicted as yellow "facets" in Fig. 5.4. These concave π surfaces are reputed to interact strongly with other small organic molecules[39,60]. The charge distribution for an individual TiOPc molecule, determined by DFT calculation, indicates the peripheral phenyl rings bear partial positive charge. In the following, we try to rationalize the stabilizing force with dipole-induced dipole interactions.

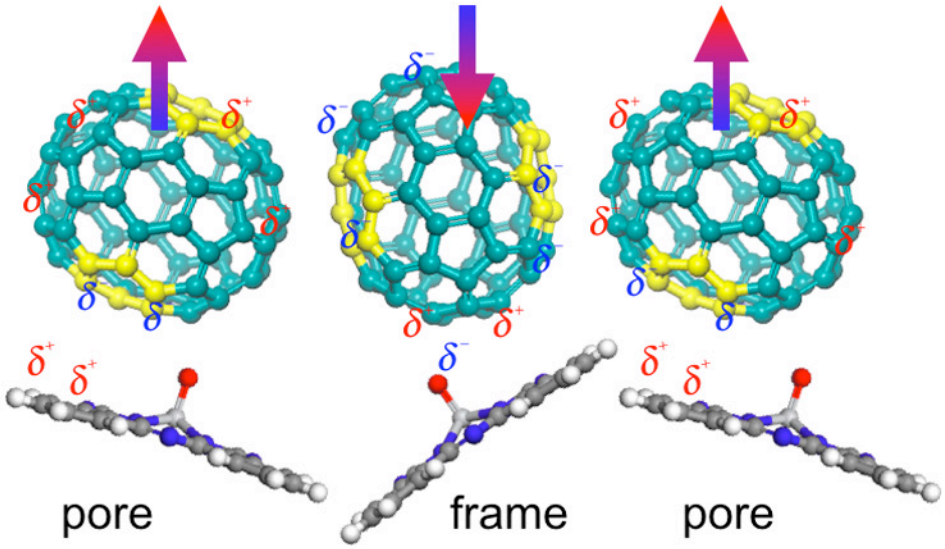

Figure 5.4 Schematic illustration of first layer C_{70} adsorption and charge redistribution, arrows indicate induced dipole moment, pointing from negative to positive.

The local configurations of "C_{70}-on-pore" and "C_{70}-on-frame" over honeycomb TiOPc are depicted in Fig. 5.4. Recalling C_{70}'s high dipole polarizability and TiOPc's net permanent dipole moment, we recognize that dipole-induced dipole forces as the dominant stabilization force for "C_{70}-on-pore". The charge redistribution is marked with δ^- or δ^+ in the figure. The "C_{70}-on-frame" (center C_{70} in Fig. 5.4) are stabilized by a strong mutually induced dipole polarization, as shown with the schematic charge redistribution of adsorbed C_{70} in Fig. 5.4. The induced dipole moment on each C_{70} is

shown by the arrows, "C_{70}-on-pore" and "C_{70}-on-frame" thus have antiparallel induced dipole moments, strengthening the intermolecular C_{70} interaction between "C_{70}-on-pore" and "C_{70}-on-frame". This qualitative electrostatic analysis is completely consistent with the C_{70}-TiOPc interface structures for the first C_{70} layer.

We can test this electrostatic model against the measured *z(V)* properties and C_{70} topographic variations. Following the model, "C_{70}-on-pore" contacts underlying TiOPc with the curved π surface. The long C_{70} axis thus faces the TiOPc phenyl rings, which have a net positive charge. This induces a negative charge in "C_{70}-on-pore" molecules at their molecular contact with TiOPc. This, in turn, leads to charge redistribution for "C_{70}-on-frame", as shown in the side C_{70} of Fig. 5.4. To optimize this electrostatic interaction, "C_{70}-on-frame" molecules orient their long molecular axis nearly normal to the surface (the middle molecule in Fig. 5.4), to maximize overlap of the C_{70} concave surface with the oppositely charged convex surface of the adjacent "C_{70}-on-pore" molecule. This vertical C_{70} orientation for "C_{70}-on-frame" molecules will enhance charge transfer from TiOPc to "C_{70}-on-frame". Indeed, this is reflected in the relative positions of the LUMO levels for "C_{70}-on-pore" and "C_{70}-on-frame" molecules, as well as their apparent height differences in STM images.

These C_{70}-TiOPc interfaces stand in sharp contrast with C_{60}-TiOPc interfaces. Recall that C_{60} molecules avoid TiOPc honeycomb pore sites. Deposition of C_{60} simply erodes the TiOPc honeycomb and leads to the two-dimensional phase separation of C_{60} and TiOPc. Beyond their structural and electronic similarities, C_{60} and C_{70} possess some key differences. C_{70} possesses concave "facets" and larger dipole polarizability. These molecular attributes will strongly impact interface

formation. This can be demonstrated clearly in reverse-sequence growth experiments. Interfaces formed by depositing TiOPc on monolayers of C_{60} and C_{70} are shown in Fig. 5.5. For TiOPc-C_{70} bilayer structure, a molecularly resolved TiOPc top-layer indicates a highly stable heterostructure. Vacancies in the TiOPc layer confirm the crystallinity of the TiOPc layer and 1:1 stoichiometry with the C_{70} sub-layer. In the case of TiOPc-C_{60} system, however, the TiOPc layer appears much more disordered. The noisiness of the images and the absence of vacancy defects indicate the greater mobility of TiOPc molecules on the C_{60} monolayer. Similar result has been reported for C_{70}/ZnTPP[60].

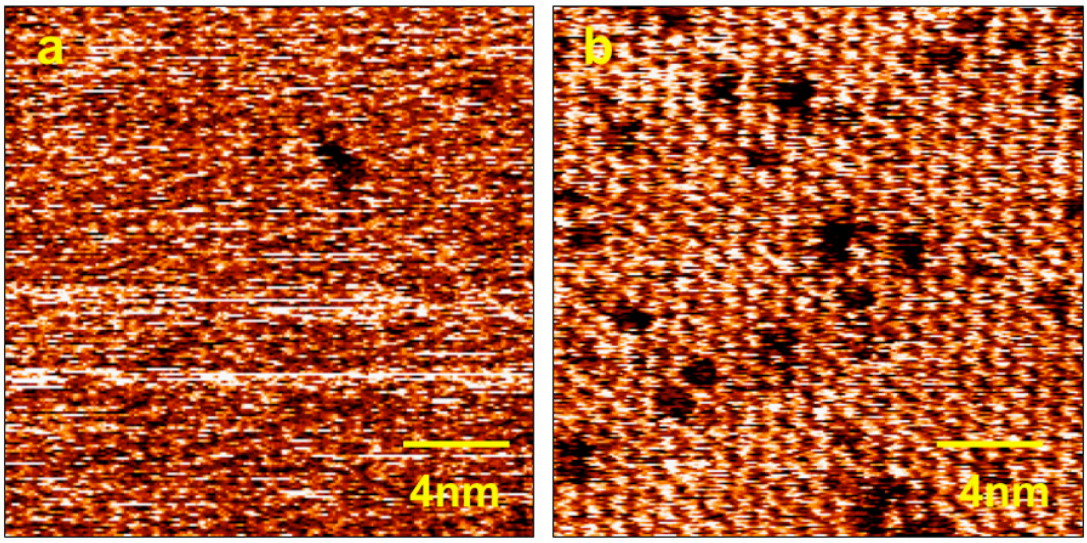

Figure 5.5 STM images of TiOPc on top of monolayer fullerenes (a) TiOPc on top of monolayer C_{60} (b) TiOPc on top of monolayer C_{70}.

Based upon qualitative electrostatic considerations, we are able to rationalize all structures observed for C_{60}- and C_{70}- TiOPc honeycomb heterointerfaces. We anticipate that the energy differences between "C_{70}-on-pore" and "C_{70}-on-frame" will be on the order of just 10's of meV. Such energetic differences remain difficult to

calculate for these molecular films, particularly given the size of the unit cell. Fortunately, these energetic differences can be qualitatively predicted from the properties of individual molecules, providing a basis for structure prediction.

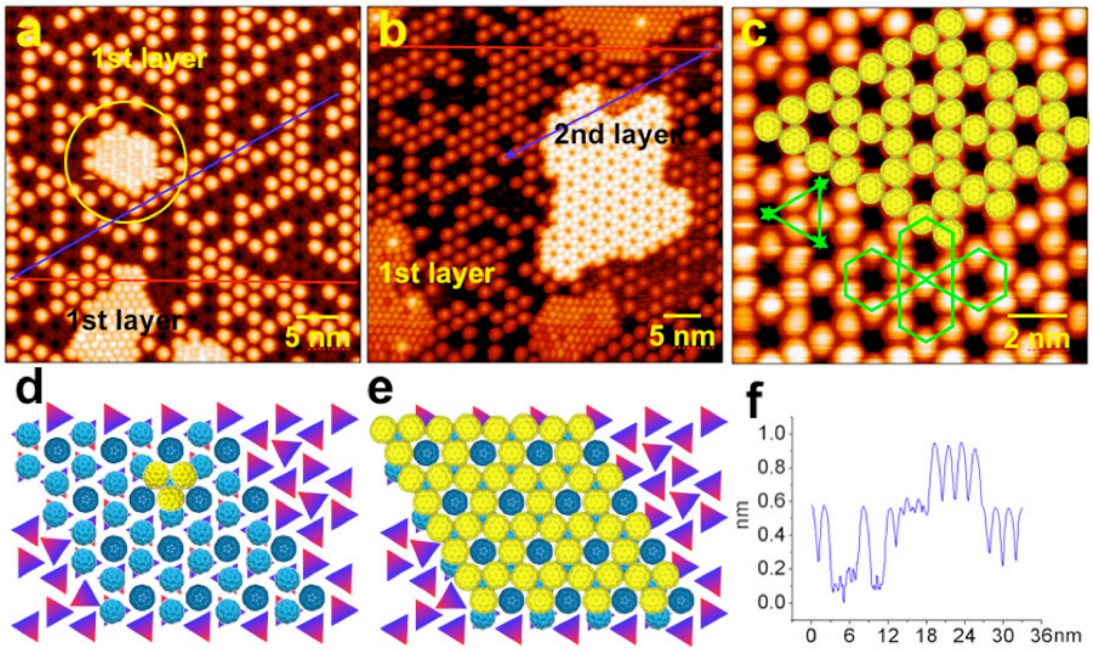

Figure 5.6 Onset of second-layer C_{70} grow on the TiOPc honeycomb template. (a) STM image of first-layer C_{70} showing the C70-on-pore and C70-on-frame molecules of the first layer (b) Island of second layer C_{70} supported above the first layer (c) High magnified STM image of the "kagome" second layer C_{70} structure, with structural model (yellow) superimposed. (d) Structural model of lying-down C_{70} adsorbed on bridge sites of the C_{70}-on-frame with three rotational orientations by 120° (e) Structural model of second layer C_{70} (yellow) on top of first layer (blue) (f) Line profile along the blue line in (b).

With increasing C_{70} deposition, second layer C_{70} starts to grow on top of the first-layer C_{70} (hexagonal close-packed C_{70} structure). Onset features for second-layer C_{70} are zigzag rows with interstitials, circled in yellow in Fig 5.6a. A large area of the second layer C_{70} is shown in Fig. 5.6b. Unlike C_{70}'s growth habit on Ag(111), in which molecules demonstrate an fcc stacking mode in the vertical direction, the second layer of C_{70} on the honeycomb TiOPc structure is *not* close-packed. Instead, they form a "kagome" lattice. In the kagome lattice, C_{70} molecules organize into

hexagons and trigons, as emphasized in Fig 5.6c. The centers of neighboring hexagons in the kagome structure are spaced at 20.8 Å and in registration with pore TiOPc molecules and "C_{70}-on-pore". Furthermore, C_{70} molecules in this layer appear ellipsoidal in STM topographs, indicating a lying down configuration. Also, three C_{70} molecules forming the trigon have distinct orientations rotated by 120°, marked by green arrows in Fig. 5.6c.

A structural model for the second layer C_{70} is developed from the experimental observations. In Fig. 5.6d, the first layer close packed structure is constituted with "C_{70}-on-frame" (light blue) and "C_{70}-on-pore" (dark blue). The second layer C_{70} molecules (yellow) seek bridge sites above two neighboring "C_{70}-on-frame" molecules on the first layer. (This corresponds to bridge sites of neighboring frame TiOPc molecules in the honeycomb structure.) A complete structural model is shown in Fig. 5.6e and superimposed onto the STM image in 5.6c.

Drawing upon the dipole model for the first-layer C_{70} (Fig 5.4), we place second layer C_{70} on sites that minimize the electrostatic interactions. The process is shown in Fig. 5.7. The base layer in Fig. 5.7 is a top-down view of Fig 5.4 with marked charge redistribution. In order to maximize the in-plane coordination number of the second layer C_{70}, all on-top sites are excluded. Also, it is clear that the hollow site of the first layer C_{70} is energetically unfavorable for C_{70} adsorption (due to local charge). The same argument applies to bridge site between neighboring "C_{70}-on-pore" and "C_{70}-on-frame" molecules. Consequently, bridge sites between neighboring "C_{70}-on-frame" molecules represent the local potential minima and the favorable adsorption sites for second layer C_{70}. The second layer C_{70} molecules thus form the "kagome"

structure with four nearest neighbor molecules in plane, as observed in the STM measurements and shown in the model.

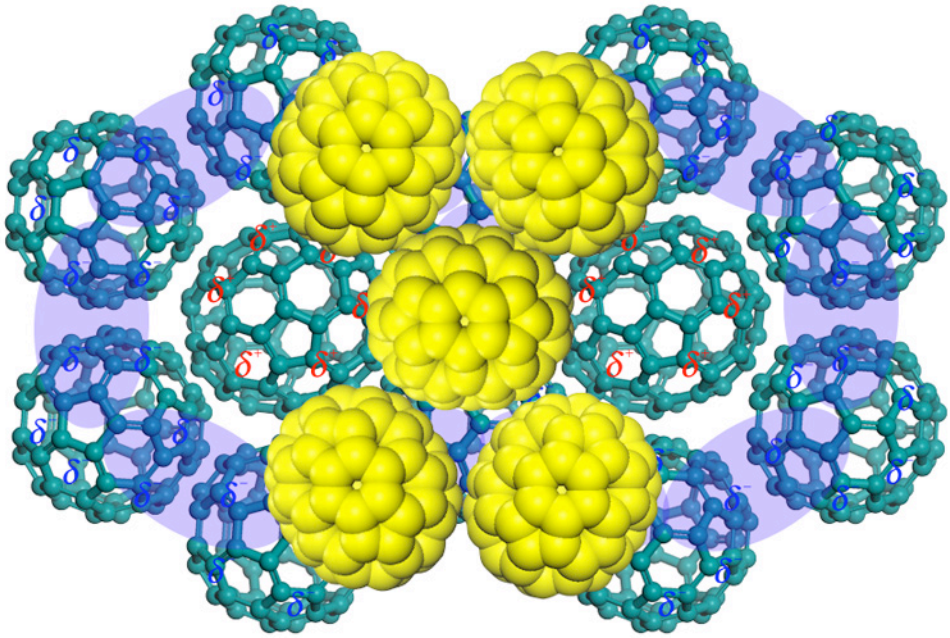

Figure 5.7 Schematic illustration of second layer C_{70} adsorption. First layer C_{70} are shown in green with charge distribution. The light blue ovals show local potential minima t favorable for adsorption. Second layer C_{70} adsorb on the bridge sites of two "C_{70}-on-frame" with partial negative charge distributed on top.

With continued C_{70} deposition, the third layer C_{70} appears, as shown in the STM image (Fig. 5.8a and b). Two distinct third layer structures are observed, a honeycomb pattern (superimposed with green circles in Fig. 5.8b) and a small close packed structure (circled in yellow). The honeycomb pattern is the dominant structure whose molecular packing model is suggested with light green C_{70} in Fig. 5.8d. The third layer "honeycomb" C_{70} molecules sit directly on the hollow position of C_{70} trigons in the kagome structure. This C_{70} honeycomb is registered vertically with the base TiOPc honeycomb. The simultaneous growth of both the honeycomb and close-

packed structures for third-layer C_{70} suggests that the influence of the base TiOPc dipole layer in C_{70} structure begins to wane within the third layer.

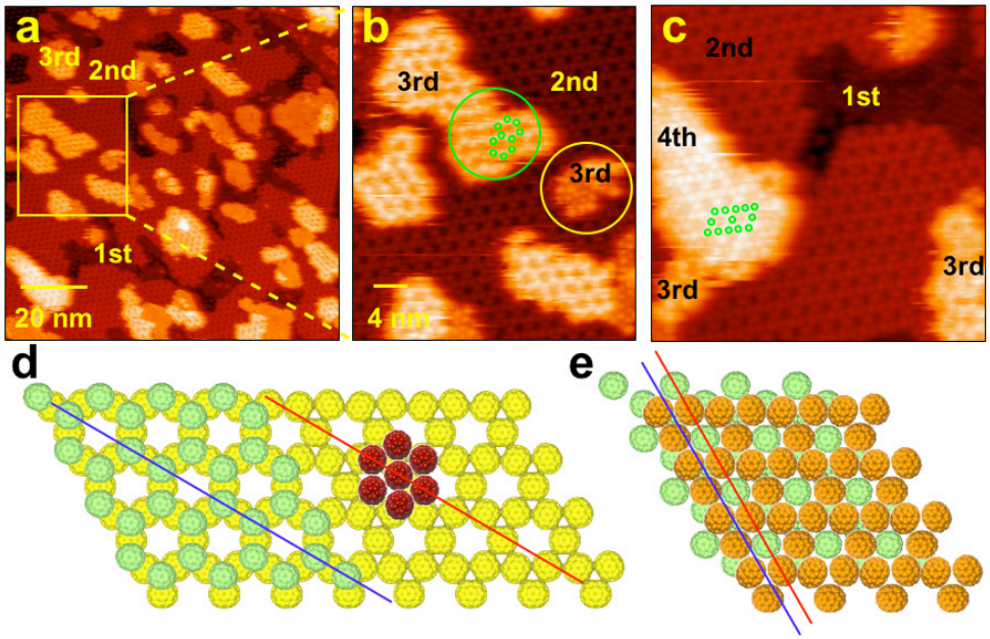

Figure 5.8 Third and fourth layer C_{70} on top of honeycomb TiOPc (a) Large scale STM image with each layer marked (b) Magnified STM image of third layer C_{70}, green dots superimposed show the honeycomb third layer structure, and inside the yellow circle shows the close packed third layer. (c) STM image of fourth layer C_{70}, green dots superimposed show the "kagome" structure. (d) Structural model of third layer honeycomb C_{70} structure (light green) and close packed third layer (maroon) (e) Structural model of fourth layer kagome C_{70} (orange).

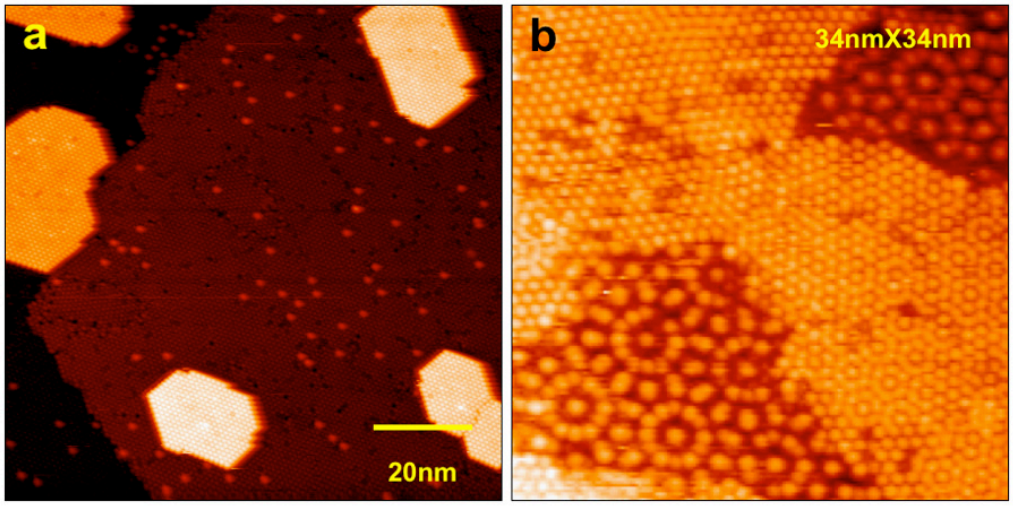

Figure 5.9 Multilayer C70 on top of honeycomb TiOPc template (a) Large STM image shows multilayer (over fourth layer) C70 with close packed structure, and quasi-hexagonal C70 islands on top. (b) STM image shows surface reconstruction of C70 top layer.

The fourth layer C_{70} can be observed occasionally in a small fractional area over the surface with a kagome structure similar to the second layer C_{70} with a lateral shift in between. A molecular packing model is presented in Fig. 5.8e with orange C_{70}. C_{70} in this layer are imperfectly registered with the base TiOPc structure, which is sketched in Fig. 5.10.

When the C_{70} thickness exceeds four layers, C_{70} molecules resume a regular bulk-like growth habit, as shown in Fig. 5.9a. The close-packed structure and limited 10-20 nm C_{70} domains are preferred for thick C_{70} adlayers. An example is shown in Fig. 5.9a where the quasi-hexagonal shape of the top C_{70} islands indicates a near equilibrium growth. Grain boundaries, dislocations, and even reconstructions are observed, as shown in Fig 5.9b, indicating that these molecular films are responding to internal stress.

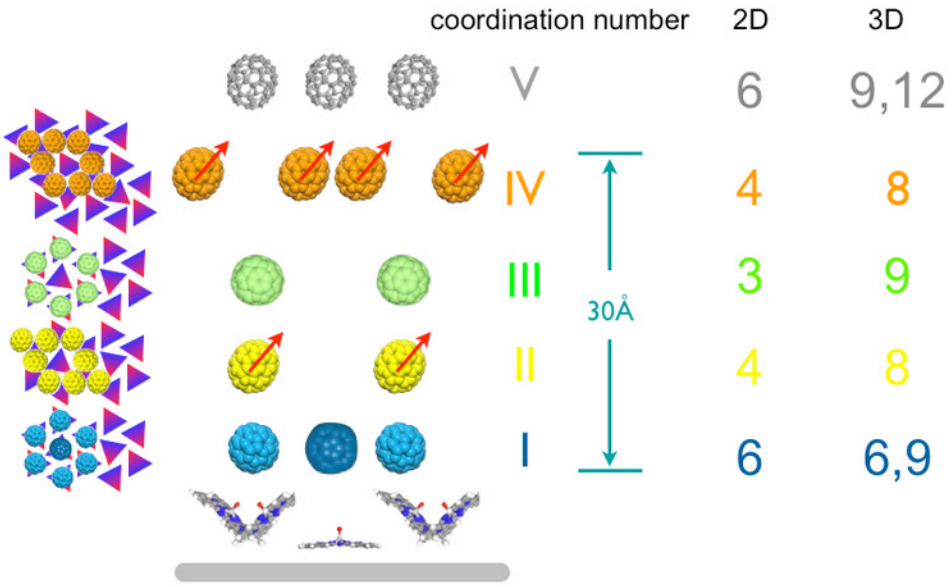

Figure 5.10 Schematic illustration of C_{70} layer-by-layer growth on top of honeycomb TiOPc, from left to right: registration of C_{70} in each layer with TiOPc honeycomb structure; side view of C_{70} multilayer; coordination number of C_{70} in plane and in 3-dimension in each layer.

5.2 Summary

In summary, we have shown that the introduction of a dipole buffer layer on the Ag(111) provides a means for controlling the structure and electronic properties of hetero-molecular interfaces. A lattice of vertical dipole moments (ca. 2 Debye in magnitude) influences the structural arrangement for at least four layers of C_{70} molecules, as illustrated in Fig. 5.10. The 2D and 3D coordination numbers for each C_{70} layer are determined, along with registration between C_{70} layers and the underlying TiOPc. First- layer C_{70} adopt a close-packed arrangement that is very robust due to the strong dipole-induced dipole interactions between C_{70}-TiOPc and C_{70}-C_{70}. The redistributed charge on the *first layer* C_{70} renders only the bridge sites between neighboring "C_{70}-on-frame" (equivalent to the bridge sites of frame TiOPc) favorable for second layer C_{70} adsorption. This leads to the formation of the interesting kagome structure. The third layer C_{70} molecules sit on the hollow sites of three nearest neighboring C_{70}'s in the second layer kagome structures, maximizing the coordination number. C_{70} in this layer retain registration with the base TiOPc honeycomb. The fourth layer C_{70} repeats the "kagome" structure as the second layer but with a lateral shift. As shown in the structural model (Fig. 5.8e), the smallest repeat unit, i.e. trigons with three C_{70} molecules in different rotational orientations by 120°, fills into the pores of the honeycomb structure in the third layer, and caps the 3D empty tube structure, as shown in Fig.5.10. The close packing growth mode is finally resumed by continuous deposition of C_{70}. The side view of this growth process is illustrated in Fig. 5.10.

C_{70} present a greater variety of molecular configurations and related properties than those of C_{60} because of the ellipsoid shape with lower symmetry and higher dipole polarizability. Except for the prominent structural difference we described above, C_{70} is also proven to have higher mobility on top of other organic layers as well as easy to stack along the vertical direction[39,119,181,182]. All these properties make them promising material in many applications, such as photovoltaic cells, in which vertical segregation of component materials is desired[175], and molecular sensors, in which 3D pore structures are highly wanted[183]. Our studies emphasize the importance of template selection and suggest a pathway of nanoarchitecture control in pursuing suitable molecular self-assembly structures for applications. Using a pre-deposited organic layer as growth template should offer a general method to generate novel surface supported structures[134,184,185].

Chapter 6 The Electronic Landscape in Binary Molecular Films

In previous chapters, we discussed the chemical morphologies of heterostructures formed in C_{60}-TiOPc and C_{70}-TiOPc systems. By tuning the deposition conditions and selecting different fullerene molecules, distinct hetero-interface structures could be realized. In this chapter, we characterize the nanoscale electronic properties of C_{60} –TiOPc heterointerfaces. A goal of this work is to determine the spatial variation in the electronic band alignment, particularly across domain boundaries. We choose this system because the formed interfaces are molecular abrupt, enabling us to correlate structural information (molecular packing and orientation) with electronic features.

6.1 Electronic Structure of TiOPc Adsorbed on Ag(111)

6.1.1 Bias Voltage Dependent Imaging

Bias voltage-dependent STM imaging is the simplest method to obtain spectroscopic information on nanoscale variations in electronic structure[186-188]. This method involves obtaining constant-current scanning tunneling microscopy images at different applied bias voltages and comparing the results. Assuming the scanning tip has nearly constant density of states in the vicinity of the Fermi level, for a positive (negative) applied sample bias voltage, the unoccupied (occupied) states of the investigated sample can be detected[71]. Although the tip DOS can be modified during experiments by sample-to-tip transfer of adsorbates[189], bias-voltage-dependent STM

measurements have provided useful spectroscopic information, especially with opposite bias[190].

An example of bias-dependent imaging is provided by the TiOPc honeycomb monolayer structure. Fig. 6.1 compares two 14×14 nm^2 STM images acquired with opposite biases at exactly the same surface area. Fig. 6.1a, acquired with 0.7 V sample bias, shows the unoccupied states of TiOPc; Figure 6.1b, acquired with -0.7 V sample bias, shows the corresponding occupied states.

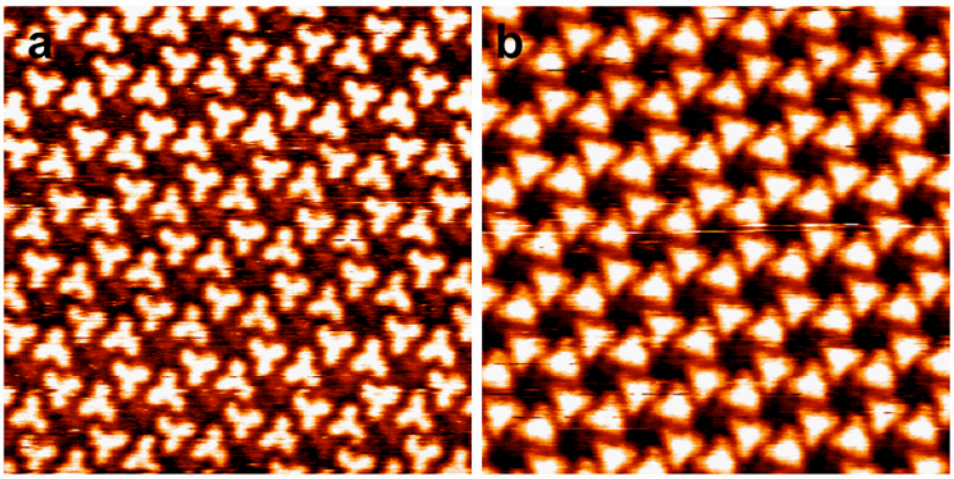

Figure 6.1 STM images (14nm $\times$ 14nm) of TiOPc honeycomb structure obtained at the same surface area successively (a) Image acquired at positive sample bias of V= 0.7 V reveals the location of unoccupied states. (b) Image acquired at negative sample bias of V= -0.7 V reveals tunneling from occupied states. Both images acquired with a constant 0.06 nA current.

An individual TiOPc molecule appears as a triangular feature in both STM images. As discussed in Chapter 3, the three lobes correspond to the two uppermost phenyl rings and the oxygen atom of a tilted molecule. The three lobes appear almost identical under positive sample bias voltage, while one lobe is significantly brighter under the negative sample bias. This difference can be understood by considering

TiOPc's molecular orbitals[191]. The TiOPc HOMO orbital has a pronounced electron distribution on the oxygen atom, leading to the bright protrusion in Fig. 6.1b.

Moreover, we note that the bias voltage must have a magnitude of at least $|V|>0.4$ V in order to achieve molecularly resolved images of the TiOPc monolayer. STM images acquired with bias voltages $|V|<0.4$ V do not exhibit clear molecular features. Evidently, resonant tunneling through the TiOPc orbitals enhances molecular resolution. This could also signify stronger tip perturbation of the film due to the closer tip-sample distance at reduced voltages.

6.1.2 *z(V)* Spectroscopy

Scanning tunneling spectroscopy (z-V) measurements were performed on TiOPc monolayers. For the hexagonal TiOPc structure (Fig. 6.2), an occupied state resonance is observed at -1.5 eV and attributed to the HOMO contribution. An empty state resonance appears at 1.9 eV, which is attributed to the LUMO correspondingly. Spectroscopic measurements at lower energies (-1.0 eV~1.0 eV) cannot be conducted with the z-V method, as described in Chapter 2. Electronic states in this lower energy range are however not excluded for this molecular semiconductor.

The transport gap of hexagonal TiOPc structure on Ag(111), measured as the difference between the STM-determined values for the HOMO and LUMO levels, is thus estimated to be 3.4 eV. This value is consistent with transport gaps measured for other MPc's under the UHV condition, such as VOPc and SnPc on Au(111)[141,192]. This transport gap is somewhat larger than the 2 eV value determined for TiOPc under ambient condition[193]. However, Teda *et al.* observed that TiOPc films under UHV exhibit n-type semiconducting behavior while a clear conversion to p-type was

observed when the film was exposed to oxygen[194]. This explains the different electronic structures obtained under different environmental conditions.

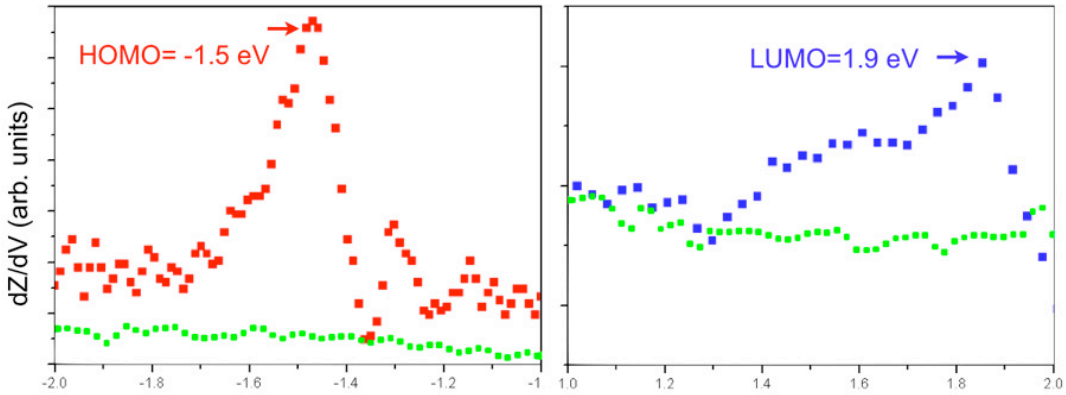

Figure 6.2 *z(V)* spectra for occupied state (left) and unoccupied state (right) of TiOPc/Ag(111) hexagonal structure (red curves); the green curves represent the states of TiOPc/Ag(111) honeycomb structure. Data acquired with a constant current of 0.05 nA, -0.8V sample bias.

We next compare z-V spectra for the TiOPc monolayers. In Fig. 6.2a, the occupied states from the hexagonal and honeycomb monolayers are shown with red and green traces, respectively. As discussed above, the prominent peak for the hexagonal monolayer is identified as the HOMO state. However, the green curve taken over TiOPc honeycomb structure appears featureless. The same situation applies to the unoccupied states of TiOPc. Fig. 2b shows a pronounced LUMO feature for the hexagonal phase, but no clear LUMO feature is observed for the honeycomb phase. We emphasize that the honeycomb monolayer is very stable, and the tunneling junction was quite stable during the z-V measurements. We attribute these spectroscopic differences to the differences in monolayer structure. The honeycomb structure, where no HOMO/LUMO features are evident, involves more highly tilted TiOPc pairs. Evidently, this geometry does not support resonance tunneling, perhaps because of the stronger intermolecular electronic coupling relative

to the hexagonal phase. This is consistent with better conductivity for herringbone stacking crystal than π stacking crystal of the same molecule[146,147,195-197]. This difference may also be connected with a larger charge transfer from the Ag(111) substrate to the honeycomb TiOPc.

6.2 Electronic Structure of C_{60} Adsorbed on Ag(111)

The electronic properties of C_{60} have been studied extensively, and this stable fullerene can serve as an internal reference for the present measurements of energy level alignment. In general, C_{60} films are stable and thus highly amenable to proximal probe spectroscopy, even under room temperature conditions. This allows us to sense slight changes in C_{60} local environment, i.e. molecular neighborhood and the distance between fullerene and Ag(111) surface from the peak position changing. The stability of the tunneling junction supports the more invasive *I(V)* measurements in addition to the *z(V)* measurements that are usually applied on other softer materials at room temperature[198-200].

We first review scanning tunneling spectra (STS) of C_{60} in the close packed islands on Ag(111). The electronic properties of C_{60} adsorbed on Ag(111) are extensively studied[135,201-206]. The LUMO-derived resonance is shifted to the Fermi level due to the reported $0.8e^-$ charge transfer from the Ag substrate to C_{60}. The HOMO-derived feature, on the other hand, does not shift significantly. The transport (HOMO-LUMO) gap thus amounts to ~1.8 eV, as reported by STS and UPS measurements[135,199,203].

This gap value is much smaller than that of a free gas phase C_{60}, which is estimated to be 4.9 eV[135]. This decrease is associated with the polarization energy due

to screening from the six nearest neighboring C_{60} molecules and the Ag substrate, which can be quantified with a simple equations[199]:

$$Epol = N \times f(\alpha) = \frac{Ne^2\alpha}{2R^4} \tag{6.1}$$

where N denotes the coordination number of the molecules, α is the static polarizability, and R is the nearest neighbor distance.

The screening from the substrate can be quantified as:

$$E_{sc} = \frac{e^2}{2D} \tag{6.2}$$

where D represents the distance between the charged molecule and its image charge under the metal surface.

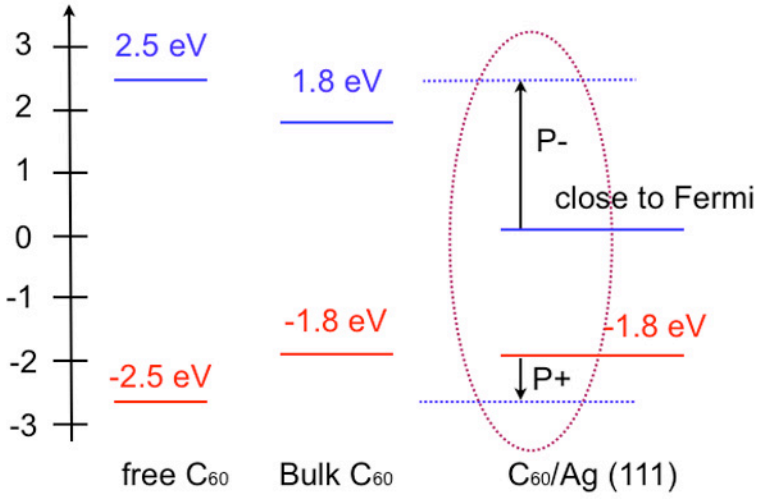

Figure 6.3 Schematic illustration of HOMO-LUMO gap reduction of C_{60} in different chemical environments.

With R=10 Å, α=85 Å^3,[207] and assuming the height of adsorbed C_{60} on Ag(111) as 4 ± 1 Å(measured from the STM images), we estimate a screening energy of 1.8 ± 0.4 eV from Ag to a single C_{60} in its close-packed island. Thus, the theoretical

band gap of C_{60} on Ag(111) is calculated as follow, which is consistent with the experimental results:

$$\Delta E_{transport} = \Delta E_{gasphase} - \Delta E_{pol} - \Delta E_{sc} = \Delta E_{gasphase} - \frac{6e^2\alpha}{2R^4} - \frac{e^2}{2D} = 4.9 - 1.2 - 1.8 = 1.9eV$$

A schematic diagram of polarization energy on C_{60} in different environments is presented in Fig. 6.3.

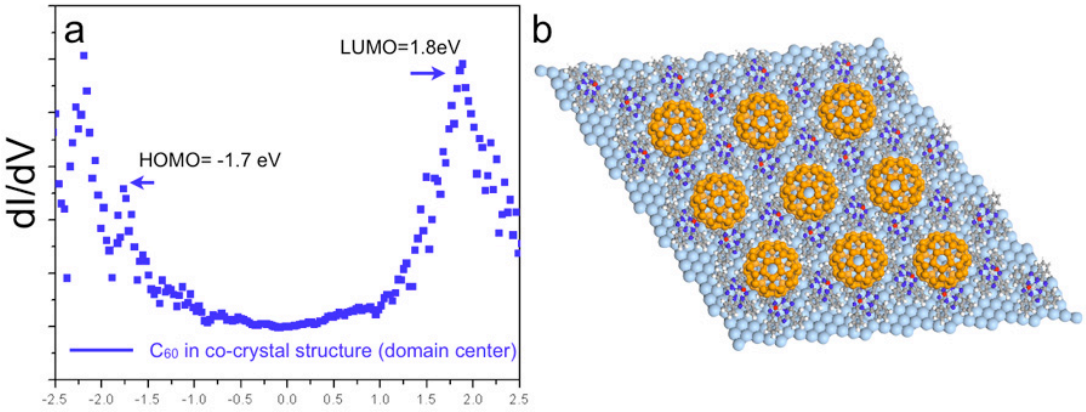

Figure 6.4 Left: I(V) spectra of C_{60} in C_{60}/TiOPc co-crystal structure (I=0.05 nA, V=0.6 V) Right: Structural model of C_{60}/TiOPc co-crystal structure, where one C_{60} molecule is surrounded by six nearest neighbor TiOPc.

We now turn to the co-crystalline phase of C_{60} and TiOPc on Ag(111). As discussed in Chapter 4, in this structure each C_{60} is surrounded by six nearest neighbor TiOPc molecules, as shown in Fig. 6.4b. The nearest neighbor separation of C_{60} molecules within this phase is 2.1 nm, significantly expanded from the 1.0 nm spacing observed in the hexagonal close-packed C_{60} films described above. The I(V) curve , taken over C_{60} in this co-crystal domain, is shown in Fig 6.4a. The LUMO and HOMO positions are measured as 1.8 eV and -1.7 eV, respectively. The HOMO-LUMO gap is 3.5 eV, about 1.7 eV larger than that of pure C_{60} on Ag.

The transport gap of the TiOPc-C_{60} co-crystal phase must reflect the local molecular environment. The dominant energetic stabilization of C_{60} in the co-crystal structure remains the metal-C_{60} interaction. The chemical interaction between C_{60} and TiOPc involves dispersion (induced polarization) forces. For these aromatic molecules, π-π interaction, especially between the co-facial molecular planes, contribute most to mutual polarizations[203]. The relative orientation of C_{60} and TiOPc molecules in the co-crystal is not co-facial though. The surrounding TiOPc molecules are not expected to provide substantial polarization energy to the central C_{60}. We thus only consider the polarization energy contributed by the silver surface. As measured by STM topography, C_{60} molecules in the co-crystalline phase are 1.0 Å higher than C_{60} in the close packed islands in the same STM image (Fig.6.5). We thus estimate that C_{60}'s within the co-crystal phase are positioned 5.0 Å above the Ag(111) surface. Substituting this value into Eqn. 6.2, we get a stabilizing energy of 1.4 eV from substrate screening effect. The transport gap is then expected to be 4.9 eV (gas phase)-1.4 eV (screening from Ag)=3.5 eV. This value is in good agreement with the observed transport gap of C_{60} in the co-crystal structure.

We have determined transport gaps of 1.8 eV (close-packed C_{60} domains) and 3.5 eV (co-crystal C_{60}-TiOPc domains) from STS measurements conducted well inside the domains. A very important issue, from a technological perspective, is the possible spatial variations of the transport gap, particularly near the domain boundary. To investigate spatial variations in the transport gap, we performed STS measurements on co-crystalline domains at points in the domain interior (marked blue) and along the domain boundary (marked Red), as shown in Fig. 6.6b. The resulting I(V) spectra,

presented in Fig. 6.6a, are the average of measurements (10~15 traces) performed at interior (blue) and boundary (red) of a domain. These measurements determine that the LUMO peak of the "boundary-C_{60}", positioned at 2.0eV, is shifted 0.2 eV higher in energy relative to the domain interior. Additionally, a new occupied state appears at -1.4 eV. The energetic difference between these features, 3.4 eV, is comparable to the transport gap determined in the co-crystalline domain interior.

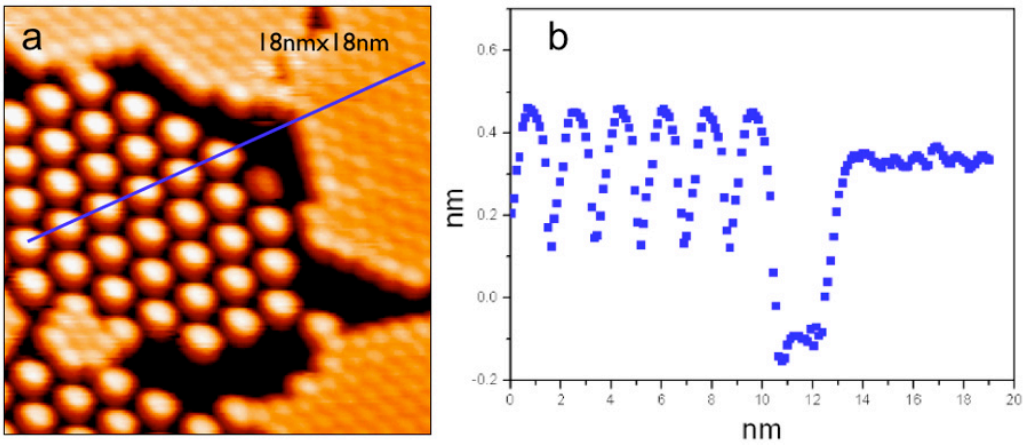

Figure 6.5 STM image of co-crystal C_{60} coexist with close packed C_{60} (a) and line profile (b) along the blue solid line.

We now discuss the physical origin of the -1.4 eV state found at the edge of co-crystalline domains. It is unlikely that this new state represents simply a shift in the co-crystalline domain HOMO due to a different polarization energy. The C_{60} height does not change and thus the polarization from the Ag(111) is unchanged. Significantly, the TiOPc molecular packing around these "domain-boundary-C_{60}" is somewhat more disordered than around the "domain-interior-C_{60}" and involves fewer nearest TiOPc neighbors. These missing 1~2 TiOPc neighbors permits other TiOPc neighbors to adjust their configurations (tilting angle and orientation rotation with respect to C_{60}). The domain boundaries may support more co-facial C_{60}-TiOPc

arrangements than the interior domain boundary. Such geometries would provide more polarization energy and may lead to hybridization states, which account for the -1.4 eV feature.

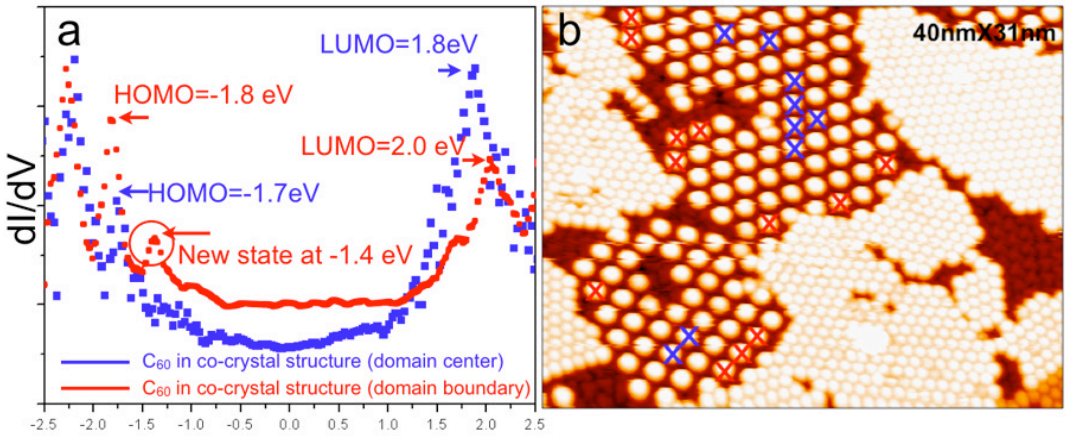

Figure 6.6 STS measurements on C_{60} in different environments. (I=0.05 nA, V=0.6 V) Blue: C_{60} in co-crystal structure domain center, corresponding to blue X in (b) Red: C_{60} in co-crystal structure domain boundaries, corresponding to red X in (b).

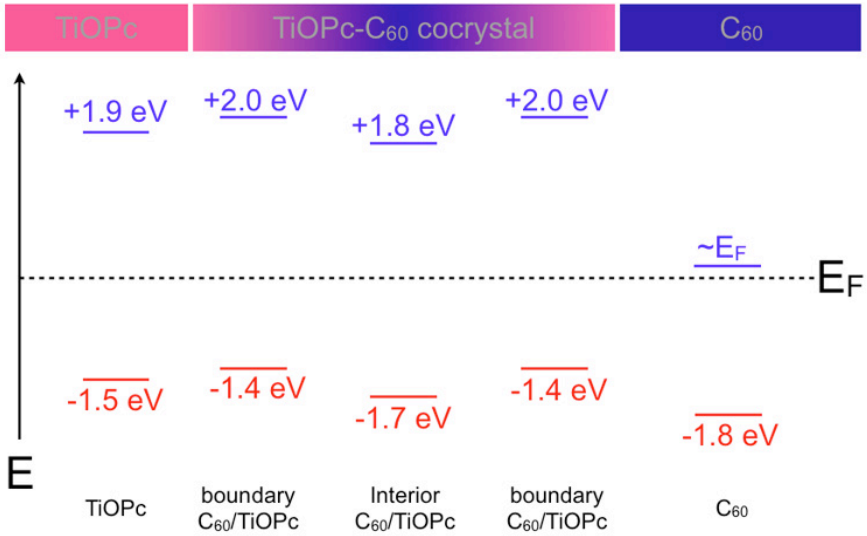

Figure 6.7 Schematic energy level alignments on TiOPc-C_{60} interfaces.

We now summarize the energy alignment of the C_{60}-TiOPc hetero-structures in Fig. 6.7. Here, we assume that the energy bands for the pure TiOPc domains do not

vary with position. This simple energy diagram suggests the boundary of TiOPc-C_{60} co-crystal structure puts an energy barrier at a value of ~0.1 eV for electron transport. Without this barrier, the photo-generated excitons should be dissociated at the interface of TiOPc/TiOPc-C_{60} and electrons should transfer to the acceptor C_{60} domain. This 0.1 eV barrier effect may be probed further via the spatially resolved work function measurements. Although this work is done within monolayers supported on Ag(111), real devices require thicker films up to 100 nm. It is almost inevitable to form such kind of co-crystal structures on donor-acceptor heterojunctions, an energy barrier at the interface would change the simple picture of band alignment between donor and acceptor materials and thus impede effective electron transport. It is thus important to identify the physical origins so that methods for barrier control can be developed for better performance of OPV cells.

Chapter 7 Summary and Outlook

The donor-acceptor molecular film architectures by selecting TiOPc and fullerene (C_{60}, C_{70}) as model systems were investigated with STM/STS. Especially, I measured the orientation and separation of donor/acceptor molecules along the domain boundaries, and correlated the structural information (from STM) with the electronic information (from STS). The main goal of this research is to optimize the growth of donor-acceptor films so that the charge transport on the interfaces is improved.

Several general observations are outlined and future investigations of interest are proposed as following:

(1) The heterointerfacial architecture between two organic materials is driven by a combination of thermodynamic and kinetic factors. In most cases, thermodynamic control has been the more common approach to design desired nanostructures. However, I have demonstrated in this thesis that by tuning the growth conditions and choosing different component materials, a delicate balance between intermolecular interaction and adsorbate-substrate interaction can be modulated. We can thus employ a kinetic route to access surface structures that are thermodynamically metastable (hexagonal and triangular network structures of TiOPc) or stable (co-crystal structure of $TiOPc_{(2)}C_{60(1)}$) structures.

This assembly route is different from direct supramolecular bonding, such as hydrogen and halogen bonds. A highly anisotropic intermolecular interaction plays an important role in selecting the final structures. Based on these observations, it would be of interest to investigate other binary systems, such as tin phthalocyanine (SnPc)

/C_{60}, copper phthalocyanine (CuPc) /phenyl-C_{61}-butyric acid methyl ester (PCBM).

SnPc is structurally similar to TiOPc, while PCBM is similar to C_{60}. A common property of SnPc and PCBM is that they both have a very high critical nucleation density at room temperature due to a repulsive intermolecular interaction[148,208,209]. This ensures a homogeneous 2D gas filling on the surface terrace without pre-nucleation. Assuming weak SnPc-C_{60}, CuPc-PCBM interaction, sequentially adsorbed second molecular species with stronger intermolecular attraction is expected to segregate into small domains.

(2) Stacking fault type dislocations in molecular films have been observed for several other molecular systems in addition to TiOPc, such as chlorine zinc phthalocyanine ($ZnPcCl_8$) with periodicity at ~5nm[210,211], anthracene carboxylic acid (AnCA) with periodicity at ca. 14nm. We have demonstrated here that using the molecular dislocations as nanotemplate for sequential molecular deposition, a pattern of nanophase-segregated C_{60} and TiOPc domains with characteristic domain size of 7 nm is obtained. For chemical self-assembly, patterns with this 10 nm lengthscale have been achieved with bimolecular and polymeric spacers. Still, there remain significant limitations in applicable materials and in pattern fidelity. Sequential deposition of fullerene molecules onto such stacking faults structures to test their template effects would be interesting future experiments.

(3) The distinct growth mode of C_{70} multilayers on top of TiOPc honeycomb structure suggests a promising method to construct novel 3D pore structures. The key point of this method is to find a template with distinct electrostatic properties, resulting favorable and unfavorable adsorption sites for the guest molecules. On the

other hand, the guest molecule should be chosen to possess high polarizability, and a proper molecular shape that favors vertical stacking.

(4) Local electronic properties of C_{60} and C_{70} in different molecular environments are studied with *z(V)* and I(V) measurements. Basic understandings of how to control chemical morphology along the donor-acceptor interface and how this morphology influences electronic properties are achieved.

STS measurement is an invaluable technique to probe electronic structure variations at nanoscale corresponding to the STM-characterized film chemical morphology. Many experiments have been carried out on exploring the local electronic properties. Most of them are concerned with "clean systems" such as single molecular spectroscopy, or homogeneous molecular structures (single component and single-phase systems)[115,192,199,212-214]. Practically, electronic structures along and across donor-acceptor domain boundaries are more important in the way they affect energy alignment for exciton dissociation and charge transport. We started this study by measuring I(V) spectra across TiOPc-C_{60} model heterojunctions. Different electronic states are identified on the TiOPc-C_{60} co-crystal domain boundary, with LUMO level shift (0.2 eV higher) and emergence of a new HOMO state. This results in an energy level alignment unfavorable for the electron transport from donor material (TiOPc) to acceptor (C_{60}) due to an energy barrier of ~0.1 eV across the donor-acceptor interface. Possible origins could be hybridization between TiOPc and C_{60} orbitals or stronger mutually polarization effects due to the different relative orientations on the boundaries. Our observations suggest a very likely reason that impedes the efficiency of current OPV cells, since co-crystal is an inevitable

phenomenon in multicomponent cells. The barrier on the co-crystal interfaces will have a huge effect in effective charge transport, and methods to lower or eliminate this barrier need to be identified. This effect may be sensed more directly via spatially resolved work function measurements by Scanning Kelvin probe, which are currently been undertaken by us.

Another practical issue of STS is the limitation in probing buried structure of 3-D donor-acceptor interfaces that are directly relevant for photovoltaic devices. Ambient Kelvin Probe measurements on films with characterized device thickness and structures will provide excellent and practical information further correlating morphology and electronic structures of OPV cells.

Moreover, room temperature STS measurements can only be performed effectively with $|V_{bias}| > 1V$ due to unstable tunneling junction at lower absolute bias voltages. Performing spectroscopy measurements at lower temperatures, where the tunneling junction will be more stable, will allow us to extend the voltage range for spectroscopy within 100 mV of the Fermi level.

Bibliography:

(1) Shaheen, S. E.; Radspinner, R.; Peyghambarian, N.; Jabbour, G. E. *Applied Physics Letters* **2001**, *79*, 2996-2998.

(2) Sariciftci, N. S.; Smilowitz, L.; Heeger, A. J.; Wudl, F. *Science* **1992**, *258*, 1474-1476.

(3) Gratzel, M. *Nature* **2001**, *414*, 338-344.

(4) Hagfeldt, A.; Gratzel, M. *Accounts of Chemical Research* **2000**, *33*, 269-277.

(5) Peumans, P.; Yakimov, A.; Forrest, S. R. *Journal of Applied Physics* **2004**, *95*, 2938-2938.

(6) Li, X. Y.; Wang, H. X.; Wu, H. X. In *Functional Phthalocyanine Molecular Materials*; Vol. 135, p 229-273.

(7) Kojima, T.; Honda, T.; Ohkubo, K.; Shiro, M.; Kusukawa, T.; Fukuda, T.; Kobayashi, N.; Fukuzumi, S. *Angewandte Chemie-International Edition* **2008**, *47*, 6712-6716.

(8) Jin, Z.; Masuda, H.; Yamanaka, N.; Minami, M.; Nakamura, T.; Nishikitani, Y. *Journal of Physical Chemistry C* **2009**, *113*, 2618-2623.

(9) Imahori, H.; Umeyama, T.; Ito, S. *Accounts of Chemical Research* **2009**, *42*, 1809-1818.

(10) Padinger, F.; Rittberger, R. S.; Sariciftci, N. S. *Advanced Functional Materials* **2003**, *13*, 85-88.

(11) Schwartz, B. J. *Annual Review of Physical Chemistry* **2003**, *54*, 141-172.

(12) Moons, E. *Journal of Physics-Condensed Matter* **2002**, *14*, 12235-12260.

(13) Coakley, K. M.; McGehee, M. D. *Chemistry of Materials* **2004**, *16*, 4533-4542.

(14) Liu, A.; Zhao, S.; Rim, S. B.; Wu, J.; Konemann, M.; Erk, P.; Peumans, P. *Advanced Materials* **2008**, *20*, 1065-+.

(15) Gregg, B. A.; Hanna, M. C. *Journal of Applied Physics* **2003**, *93*, 3605-3614.

(16) Wolf, M. S. a. H. C. *Organic Molecular Solids*; Wiley-VCH, 2007.

(17) Forrest, S. R. *Mrs Bulletin* **2005**, *30*, 28-32.

(18) Hoppe, H.; Sariciftci, N. S. *Journal of Materials Research* **2004**, *19*, 1924-1945.

(19) Bauert, T.; Merz, L.; Bandera, D.; Parschau, M.; Siegel, J. S.; Ernst, K. H. *Journal of the American Chemical Society* **2009**, *131*, 3460-+.

(20) Bernstein, J. *Chemical Communications* **2005**, 5007-5012.

(21) Bonifazi, D.; Kiebele, A.; Stohr, M.; Cheng, F. Y.; Jung, T.; Diederich, F.; Spillmann, H. *Advanced Functional Materials* **2007**, *17*, 1051-1062.

(22) Perdigao, L. M. A.; Perkins, E. W.; Ma, J.; Staniec, P. A.; Rogers, B. L.; Champness, N. R.; Beton, P. H. *Journal of Physical Chemistry B* **2006**, *110*, 12539-12542.

(23) Nath, K. G.; Ivasenko, O.; Miwa, J. A.; Dang, H.; Wuest, J. D.; Nanci, A.; Perepichka, D. F.; Rosei, F. *Journal of the American Chemical Society* **2006**, *128*, 4212-4213.

(24) Furukawa, S.; Uji-i, H.; Tahara, K.; Ichikawa, T.; Sonoda, M.; De Schryver, F. C.; Tobe, Y.; De Feyter, S. *Journal of the American Chemical Society* **2006**, *128*, 3502-3503.

(25) Stohr, M.; Wahl, M.; Galka, C. H.; Riehm, T.; Jung, T. A.; Gade, L. H. *Angewandte Chemie-International Edition* **2005**, *44*, 7394-7398.

(26) De Feyter, S.; Miura, A.; Yao, S.; Chen, Z.; Wurthner, F.; Jonkheijm, P.; Schenning, A.; Meijer, E. W.; De Schryver, F. C. *Nano Letters* **2005**, *5*, 77-81.

(27) De Feyter, S.; De Schryver, F. C. *Chemical Society Reviews* **2003**, *32*, 393-393.

(28) Gottarelli, G.; Masiero, S.; Mezzina, E.; Pieraccini, S.; Rabe, J. P.; Samori, P.; Spada, G. P. *Chemistry-a European Journal* **2000**, *6*, 3242-3248.

(29) Samori, P.; Francke, V.; Mullen, K.; Rabe, J. P. *Chemistry-a European Journal* **1999**, *5*, 2312-2317.

(30) Yokoyama, T.; Yokoyama, S.; Kamikado, T.; Okuno, Y.; Mashiko, S. *Nature* **2001**, *413*, 619-621.

(31) Mena-Osteritz, E.; Bauerle, P. *Advanced Materials* **2006**, *18*, 447-+.

(32) Uji-i, H.; Miura, A.; Schenning, A.; Meijer, E. W.; Chen, Z. J.; Wurthner, F.; De Schryver, F. C.; Van der Auweraer, M.; De Feyter, S. *Chemphyschem* **2005**, *6*, 2389-2395.

(33) Liddell, P. A.; Sumida, J. P.; Macpherson, A. N.; Noss, L.; Seely, G. R.; Clark, K. N.; Moore, A. L.; Moore, T. A.; Gust, D. *Photochemistry and Photobiology* **1994**, *60*, 537-541.

(34) Theobald, J. A.; Oxtoby, N. S.; Phillips, M. A.; Champness, N. R.; Beton, P. H. *Nature* **2003**, *424*, 1029-1031.

(35) Samori, P.; Engelkamp, H.; de Witte, P.; Rowan, A. E.; Nolte, R. J. M.; Rabe, J. P. *Angewandte Chemie-International Edition* **2001**, *40*, 2348-+.

(36) Samori, P.; Cacialli, F.; Anderson, H. L.; Rowan, A. E. *Advanced Materials* **2006**, *18*, 1235-1238.

(37) Semenov, A.; Spatz, J. P.; Moller, M.; Lehn, J. M.; Sell, B.; Schubert, D.; Weidl, C. H.; Schubert, U. S. *Angewandte Chemie-International Edition* **1999**, *38*, 2547-2550.

(38) Ziener, U.; Lehn, J. M.; Mourran, A.; Moller, M. *Chemistry-a European Journal* **2002**, *8*, 951-957.

(39) Wang, Y. B.; Lin, Z. Y. *Journal of the American Chemical Society* **2003**, *125*, 6072-6073.

(40) Dmitriev, A.; Spillmann, H.; Lin, N.; Barth, J. V.; Kern, K. *Angewandte Chemie-International Edition* **2003**, *42*, 2670-2673.

(41) Lin, N.; Stepanow, S.; Vidal, F.; Barth, J. V.; Kern, K. *Chemical Communications* **2005**, 1681-1683.

(42) Alam, M. S.; Stromsdorfer, S.; Dremov, V.; Muller, P.; Kortus, J.; Ruben, M.; Lehn, J. M. *Angewandte Chemie-International Edition* **2005**, *44*, 7896-7900.

(43) Kurth, D. G.; Severin, N.; Rabe, J. P. *Angewandte Chemie-International Edition* **2002**, *41*, 3681-3683.

(44) Pirondini, L.; Stendardo, A. G.; Geremia, S.; Campagnolo, M.; Samori, P.; Rabe, J. P.; Fokkens, R.; Dalcanale, E. *Angewandte Chemie-International Edition* **2003**, *42*, 1384-1387.

(45) Barth, J. V.; Costantini, G.; Kern, K. *Nature* **2005**, *437*, 671-679.

(46) Girifalco, L. A. *Journal of Physical Chemistry* **1992**, *96*, 858-861.

(47) Wei, Y. Y.

(48) Ishii, H.; Sugiyama, K.; Ito, E.; Seki, K. *Advanced Materials* **1999**, *11*, 605-+.

(49) Braun, S.; Salaneck, W. R.; Fahlman, M. *Advanced Materials* **2009**, *21*, 1450-1472.

(50) Kaji, H.; Shimoyama, Y. *Thin Solid Films* **2002**, *408*, 245-251.

(51) Brumbach, M.; Placencia, D.; Armstrong, N. R. *Journal of Physical Chemistry C* **2008**, *112*, 3142-3151.

(52) Gao, W. Y.; Kahn, A. *Organic Electronics* **2002**, *3*, 53-63.

(53) Fukagawa, H.; Kera, S.; Kataoka, T.; Hosoumi, S.; Watanabe, Y.; Kudo, K.; Ueno, N. *Advanced Materials* **2007**, *19*, 665-+.

(54) Bruner, E. L.; Koch, N.; Span, A. R.; Bernasek, S. L.; Kahn, A.; Schwartz, J. *Journal of the American Chemical Society* **2002**, *124*, 3192-3193.

(55) Brumbach, M.; Veneman, P. A.; Marrikar, F. S.; Schulmeyer, T.; Simmonds, A.; Xia, W.; Lee, P.; Armstrong, N. R. *Langmuir* **2007**, *23*, 11089-11099.

(56) Alloway, D. M.; Hofmann, M.; Smith, D. L.; Gruhn, N. E.; Graham, A. L.; Colorado, R.; Wysocki, V. H.; Lee, T. R.; Lee, P. A.; Armstrong, N. R. *Journal of Physical Chemistry B* **2003**, *107*, 11690-11699.

(57) Mannsfeld, S. C. B.; Fritz, T. *Physical Review B* **2005**, *71*.

(58) Guldi, D. M. *Chemical Communications* **2000**, 321-327.

(59) Guldi, D. M.; Prato, M. *Accounts of Chemical Research* **2000**, *33*, 695-703.

(60) Vilmercati, P.; Castellarin-Cudia, C.; Gebauer, R.; Ghosh, P.; Lizzit, S.; Petaccia, L.; Cepek, C.; Larciprete, R.; Verdini, A.; Floreano, L.; Morgante, A.; Goldoni, A. *Journal of the American Chemical Society* **2009**, *131*, 644-652.

(61) Pfuetzner, S.; Meiss, J.; Petrich, A.; Riede, M.; Leo, K. *Applied Physics Letters* **2009**, *94*.

(62) O'Hanlon, J. F. *A user's guide to vacuum technology*; Wiley, 1980.

(63) Levlin, M.; Laakso, A. *Applied Surface Science* **2001**, *171*, 257-264.

(64) Baski, A. A.; Fuchs, H. *Surface Science* **1994**, *313*, 275-288.

(65) Hara, M.; Sasabe, H.; Yamada, A.; Garito, A. F. *Japanese Journal of Applied Physics Part 2-Letters* **1989**, *28*, L306-L308.

(66) Koma, A. *Progress in Crystal Growth and Characterization of Materials* **1995**, *30*, 129-152.

(67) Forrest, S. R.; Zhang, Y. *Physical Review B* **1994**, *49*, 11297-11308.

(68) Forrest, S. R.; Burrows, P. E.; Haskal, E. I.; So, F. F. *Physical Review B* **1994**, *49*, 11309-11321.

(69) Xu, B.; Tao, C. G.; Williams, E. D.; Reutt-Robey, J. E. *Journal of the American Chemical Society* **2006**, *128*, 8493-8499.

(70) Xu, B.; Varughese, B.; Evans, D.; Reutt-Robey, J. *Journal of Physical Chemistry B* **2006**, *110*, 1271-1276.
(71) Binnig, G.; Rohrer, H. *Helvetica Physica Acta* **1982**, *55*, 726-735.
(72) Chen, C. J. *Introduction to Scanning Tunneling Microscopy*; Oxford University Press, 1993.
(73) Wiesendanger, R. G., H. J. *Introduction to Scanning Tunneling Microscopy*; Springer-Verlag, 1996.
(74) Bonnell, D. *Scanning Probe Microscopy and Spectroscopy: Theory, Techiniques, and Applications*; Wiley-VCH: New York, 2001.
(75) H.-J. Guentherodt, R. W. *Scanning Tunneling Microscopy*; Springer, 1993, 1995,1996; Vol. Vol. I, II, and III.
(76) J. Stroscio, W. J. K. *Scanning Tunneling Microscopy*; Academic Press, 1993.
(77) Samuely, T. *STM Study of Self-assembly Phthalocyanine Derivatives and Their Hosting Properties*; University of Basel, 2008.
(78) Harrison, W. A. *Physical Review* **1961**, *123*, 85-&.
(79) Tersoff, J.; Hamann, D. R. *Physical Review B* **1985**, *31*, 805-813.
(80) Chen, C. J. *Physical Review Letters* **1990**, *65*, 448-451.
(81) Chen, C. J. *Journal of Vacuum Science & Technology a-Vacuum Surfaces and Films* **1991**, *9*, 44-50.
(82) Baro, A. M.; Miranda, R.; Alaman, J.; Garcia, N.; Binnig, G.; Rohrer, H.; Gerber, C.; Carrascosa, J. L. *Nature* **1985**, *315*, 253-254.
(83) Gimzewski, J. K.; Stoll, E.; Schlittler, R. R. *Surface Science* **1987**, *181*, 267-277.
(84) Lundqvist, B. I.; Gunnarsson, O.; Hjelmberg, H.; Norskov, J. K. *Surface Science* **1979**, *89*, 196-225.
(85) Lu, X. H.; Grobis, M.; Khoo, K. H.; Louie, S. G.; Crommie, M. F. *Physical Review B* **2004**, *70*.
(86) Bocquet, M. L.; Sautet, P. *Surface Science* **1996**, *360*, 128-136.
(87) Kroger, J.; Jensen, H.; Berndt, R.; Rurali, R.; Lorente, N. *Chemical Physics Letters* **2007**, *438*, 249-253.
(88) Jung, T. A.; Schlittler, R. R.; Gimzewski, J. K. *Nature* **1997**, *386*, 696-698.
(89) Gimzewski, J. K.; Jung, T. A.; Cuberes, M. T.; Schlittler, R. R. *Surface Science* **1997**, *386*, 101-114.
(90) Moresco, F.; Meyer, G.; Rieder, K. H.; Ping, H.; Tang, H.; Joachim, C. *Surface Science* **2002**, *499*, 94-102.
(91) Gimzewski, J. K.; Joachim, C.; Schlittler, R. R.; Langlais, V.; Tang, H.; Johannsen, I. *Science* **1998**, *281*, 531-533.
(92) Buchner, F.; Warnick, K. G.; Wolfle, T.; Gorling, A.; Steinruck, H. P.; Hieringer, W.; Marbach, H. *Journal of Physical Chemistry C* **2009**, *113*, 16450-16457.
(93) Cyr, D. M.; Venkataraman, B.; Flynn, G. W.; Black, A.; Whitesides, G. M. *Journal of Physical Chemistry* **1996**, *100*, 13747-13759.

(94) Rosei, F.; Schunack, M.; Naitoh, Y.; Jiang, P.; Gourdon, A.; Laegsgaard, E.; Stensgaard, I.; Joachim, C.; Besenbacher, F. *Progress in Surface Science* **2003**, *71*, 95-146.

(95) Heinz, R.; Rabe, J. P. *Langmuir* **1995**, *11*, 506-511.

(96) Cyr, D. M.; Venkataraman, B.; Flynn, G. W. *Chemistry of Materials* **1996**, *8*, 1600-1615.

(97) Mayer, D.; Dretschkow, T.; Ataka, K.; Wandlowski, T. *Journal of Electroanalytical Chemistry* **2002**, *524*, 20-35.

(98) Oura, K. *Surface Science: An Introduction*; Springer-Verlag, 2003.

(99) Jin, W., *Scanning Tunneling Microscopy/Spectroscopu Studies of Binary Organic Films*; University of Maryland, 2009.

(100) Warren J. Hehre, L. R., Paul v.R. Schleyer and John A. Pople *Ab initio Molecular Orbital Theory*; John Wiley& Sons: New York, 1986.

(101) Kroto, H. W.; Heath, J. R.; Obrien, S. C.; Curl, R. F.; Smalley, R. E. *Nature* **1985**, *318*, 162-163.

(102) Ruoff, K. M. K. a. R. S. *Fullerenes: chemistry, physics, and technolgoy*; John Wiley & Sons, Inc., 2000.

(103) Kratschmer, W.; Lamb, L. D.; Fostiropoulos, K.; Huffman, D. R. *Nature* **1990**, *347*, 354-358.

(104) Hardie, R. J.; Godfrey, P. D.; Raston, C. L. *Chemistry-a European Journal* **1999**, *5*, 1828-1833.

(105) Tzeng, C. T.; Lo, W. S.; Yuh, J. Y.; Chu, R. Y.; Tsuei, K. D. *Physical Review B* **2000**, *61*, 2263-2272.

(106) Jones, D. E. H. *Nature* **1996**, *381*, 384-384.

(107) Altman, E. I.; Colton, R. J. *Physical Review B* **1993**, *48*, 18244-18249.

(108) Altman, E. I.; Colton, R. J. *Surface Science* **1993**, *295*, 13-33.

(109) Zhang, X.; Yin, F.; Palmer, R. E.; Guo, Q. *Surface Science* **2008**, *602*, 885-892.

(110) Schull, G.; Berndt, R. *Physical Review Letters* **2007**, *99*.

(111) Sakurai, T.; Wang, X. D.; Xue, Q. K.; Hasegawa, Y.; Hashizume, T.; Shinohara, H. *Progress in Surface Science* **1996**, *51*, 263-408.

(112) Rogero, C.; Pascual, J. I.; Gomez-Herrero, J.; Baro, A. M. *Journal of Chemical Physics* **2002**, *116*, 832-836.

(113) Modesti, S.; Cerasari, S.; Rudolf, P. *Physical Review Letters* **1993**, *71*, 2469-2472.

(114) Gimzewski, J. K.; Modesti, S.; David, T.; Schlittler, R. R. *Journal of Vacuum Science & Technology B* **1994**, *12*, 1942-1946.

(115) Feng, M.; Zhao, J.; Petek, H. *Science* **2008**, *320*, 359-362.

(116) Giudice, E.; Magnano, E.; Rusponi, S.; Boragno, C.; Valbusa, U. *Surface Science* **1998**, *405*, L561-L565.

(117) Pai, W. W.; Hsu, C. L.; Chiang, C. R.; Chang, Y.; Lin, K. C. *Surface Science* **2002**, *519*, L605-L610.

(118) Pai, W. W.; Hsu, C. L.; Lin, K. C.; Sin, L. Y.; Tang, T. B. *Applied Surface Science* **2005**, *241*, 194-198.

(119) Kiebele, A.; Bonifazi, D.; Cheng, F. Y.; Stohr, M.; Diederich, F.; Jung, T.; Spillmann, H. *Chemphyschem* **2006**, *7*, 1462-1470.

(120) Katsonis, N.; Marchenko, A.; Fichou, D. *Advanced Materials* **2004**, *16*, 309-+.

(121) Stasevich, T. J.; Tao, C. G.; Cullen, W. G.; Williams, E. D.; Einstein, T. L. *Physical Review Letters* **2009**, *102*.

(122) Tao, C. G.; Stasevich, T. J.; Cullen, W. G.; Einstein, T. L.; Williams, E. D. *Nano Letters* **2007**, *7*, 1495-1499.

(123) Lambin, P.; Lucas, A. A.; Vigneron, J. P. *Physical Review B* **1992**, *46*, 1794-1803.

(124) Kuk, Y.; Kim, D. K.; Suh, Y. D.; Park, K. H.; Noh, H. P.; Oh, S. J.; Kim, S. K. *Physical Review Letters* **1993**, *70*, 1948-1951.

(125) Brinkmann, M.; Wittmann, J. C.; Barthel, M.; Hanack, M.; Chaumont, C. *Chemistry of Materials* **2002**, *14*, 904-914.

(126) Tsuzuki, T.; Shirota, Y.; Rostalski, J.; Meissner, D. *Solar Energy Materials and Solar Cells* **2000**, *61*, 1-8.

(127) Kong, X. H.; Yang, Y. L.; Lei, S. B.; Wang, C. *Surface Science* **2008**, *602*, 684-692.

(128) Chan, K. Y.; Tou, T. Y.; Teo, B. S. *Microelectronics Journal* **2006**, *37*, 930-937.

(129) Kang, S. J.; Joung, Y. H. *Applied Surface Science* **2007**, *253*, 7330-7335.

(130) Kiguchi, M.; Yoshikawa, G.; Saiki, K. *Journal of Applied Physics* **2003**, *94*, 4866-4870.

(131) Liu, Z. J.; Shen, Y. G. *Surface Science* **2005**, *595*, 20-29.

(132) Hoster, H. E.; Roos, M.; Breitruck, A.; Meier, C.; Tonigold, K.; Waldmann, T.; Ziener, U.; Lantifester, K.; Behm, R. J. *Langmuir* **2007**, *23*, 11570-11579.

(133) Roos, M.; Hoster, H. E.; Breitruck, A.; Behm, R. J. *Physical Chemistry Chemical Physics* **2007**, *9*, 5672-5679.

(134) Kafer, D.; Ruppel, L.; Witte, G. *Physical Review B* **2007**, *75*.

(135) Ohno, T. R.; Chen, Y.; Harvey, S. E.; Kroll, G. H.; Weaver, J. H.; Haufler, R. E.; Smalley, R. E. *Physical Review B* **1991**, *44*, 13747-13755.

(136) Sakurai, T.; Wang, X. D.; Hashizume, T.; Yurov, V.; Shinohara, H.; Pickering, H. W. *Applied Surface Science* **1995**, *87-8*, 405-413.

(137) Wang, L. L.; Cheng, H. P. *Physical Review B* **2004**, *69*.

(138) Swan, A. K.; Shi, Z. P.; Wendelken, J. F.; Zhang, Z. Y. *Surface Science* **1997**, *391*, L1205-L1211.

(139) Tromp, R. M.; Hannon, J. B. *Surface Review and Letters* **2002**, *9*, 1565-1593.

(140) Zhou, J.; Chen, D. A. *Surface Science* **2003**, *527*, 183-197.

(141) Barlow, D. E.; Hipps, K. W. *Journal of Physical Chemistry B* **2000**, *104*, 5993-6000.

(142) Hunter, C. A.; Sanders, J. K. M. *Journal of the American Chemical Society* **1990**, *112*, 5525-5534.

(143) Liu, X. D.; Kaiser, V.; Wuttig, M.; Michely, T. *Journal of Crystal Growth* **2004**, *269*, 542-549.

(144) Park, Y. H.; Yang, K.; Kim, Y. H.; Kwon, S. K. *Bulletin of the Korean Chemical Society* **2007**, *28*, 1358-1362.

(145) Verlaak, S.; Steudel, S.; Heremans, P.; Janssen, D.; Deleuze, M. S. *Physical Review B* **2003**, *68*.

(146) Liu, D. J.; Selinger, R. L. B.; Weeks, J. D. *Journal of Chemical Physics* **1996**, *105*, 4751-4760.

(147) Chi, X. L.; Li, D. W.; Zhang, H. Q.; Chen, Y. S.; Garcia, V.; Garcia, C.; Siegrist, T. *Organic Electronics* **2008**, *9*, 234-240.

(148) Stadler, C.; Hansen, S.; Kroger, I.; Kumpf, C.; Umbach, E. *Nature Physics* **2009**, *5*, 153-158.

(149) Wei, Y. *Unpublished data*.

(150) Wang, K.; Wu, Y. S.; Wang, G. T.; Wang, R. X.; Jiang, X. K.; Fu, H. B.; Li, Z. T. *Tetrahedron* **2009**, *65*, 7718-7729.

(151) Placencia, D.; Wang, W. N.; Shallcross, R. C.; Nebesny, K. W.; Brumbach, M.; Armstrong, N. R. *Advanced Functional Materials* **2009**, *19*, 1913-1921.

(152) Nanjo, M.; Cyr, P. W.; Liu, K.; Sargent, E. H.; Manners, I. *Advanced Functional Materials* **2008**, *18*, 470-477.

(153) Chua, L. L.; Zaumseil, J.; Chang, J. F.; Ou, E. C. W.; Ho, P. K. H.; Sirringhaus, H.; Friend, R. H. *Nature* **2005**, *434*, 194-199.

(154) Xue, J. G.; Rand, B. P.; Uchida, S.; Forrest, S. R. *Advanced Materials* **2005**, *17*, 66-+.

(155) Muccini, M. *Nature Materials* **2006**, *5*, 605-613.

(156) Deutsch, D.; Natan, A.; Shapira, Y.; Kronik, L. *Journal of the American Chemical Society* **2007**, *129*, 2989-2997.

(157) Yang, F.; Sun, K.; Forrest, S. R. *Advanced Materials* **2007**, *19*, 4166-+.

(158) Merz, L.; Parschau, M.; Zoppi, L.; Baldridge, K. K.; Siegel, J. S.; Ernst, K. H. *Angewandte Chemie-International Edition* **2009**, *48*, 1966-1969.

(159) Wei, Y. Y.; Robey, S. W.; Reutt-Robey, J. E. *Journal of Physical Chemistry C* **2008**, *112*, 18537-18542.

(160) Bonifazi, D.; Spillmann, H.; Kiebele, A.; de Wild, M.; Seiler, P.; Cheng, F. Y.; Guntherodt, H. J.; Jung, T.; Diederich, F. *Angewandte Chemie-International Edition* **2004**, *43*, 4759-4763.

(161) Nishiyama, F.; Yokoyama, T.; Kamikado, T.; Yokoyama, S.; Mashiko, S.; Sakaguchi, K.; Kikuchi, K. *Advanced Materials* **2007**, *19*, 117-+.

(162) Sanchez, L.; Otero, R.; Maria Gallego, J.; Miranda, R.; Martin, N. *Chem Rev* **2009**, *109*, 2081-2091.

(163) Fendrich, M.; Wagner, T.; Stohr, M.; Moller, R. *Physical Review B* **2006**, *73*.

(164) Huang, H.; Chen, W.; Chen, S.; Qi, D. C.; Gao, X. Y.; Wee, A. T. S. *Applied Physics Letters* **2009**, *94*.

(165) Stohr, M.; Wagner, T.; Gabriel, M.; Weyers, B.; Moller, R. *Advanced Functional Materials* **2001**, *11*, 175-178.

(166) Barth, J. V.; Brune, H.; Ertl, G.; Behm, R. J. *Physical Review B* **1990**, *42*, 9307-9318.

(167) Hamilton, J. C.; Foiles, S. M. *Physical Review Letters* **1995**, *75*, 882-885.

(168) Ling, W. L.; Hamilton, J. C.; Thurmer, K.; Thayer, G. E.; de la Figuera, J.; Hwang, R. Q.; Carter, C. B.; Bartelt, N. C.; McCarty, K. F. *Surface Science* **2006**, *600*, 1735-1757.

(169) Diaconescu, B.; Nenchev, G.; Jones, J.; Pohl, K. *Microscopy Research and Technique* **2007**, *70*, 547-553.

(170) Fruchart, O.; Klaua, M.; Barthel, J.; Kirschner, J. *Physical Review Letters* **1999**, *83*, 2769-2772.

(171) de la Figuera, J.; Pohl, K.; Schmid, A. K.; Bartelt, N. C.; Hrbek, J.; Hwang, R. Q. *Surface Science* **1999**, *433*, 93-98.

(172) Stroscio, J. A.; Pierce, D. T.; Dragoset, R. A.; First, P. N. *Journal of Vacuum Science & Technology a-Vacuum Surfaces and Films* **1992**, *10*, 1981-1985.

(173) Budevski, E.; Staikov, G.; J. Lorenz, W. *Electrochemical phase formation and growth*; VCH, 1996.

(174) Cyganik, P.; Buck, M.; Wilton-Ely, J.; Woll, C. *Journal of Physical Chemistry B* **2005**, *109*, 10902-10908.

(175) Sakai, J.; Taima, T.; Yamanari, T.; Saito, K. *Solar Energy Materials and Solar Cells* **2009**, *93*, 1149-1153.

(176) Graja, A.; Farges, J. P. *Advanced Materials for Optics and Electronics* **1998**, *8*, 215-228.

(177) Saito, S.; Oshiyama, A. *Physical Review B* **1991**, *44*, 11532-11535.

(178) Pardini, T.; Cepek, C.; Larciprete, R.; Sangaletti, L.; Pagliara, S.; Gotter, R.; Floreano, L.; Verdini, A.; Morgante, A.; Parmigiani, F.; Goldoni, A. *Journal of Chemical Physics* **2005**, *122*.

(179) Pardini, T.; Cepek, C.; Larciprete, R.; Sangaletti, L.; Pagliara, S.; Gotter, R.; Floreano, L.; Verdini, A.; Morgante, A.; Parmigiani, F.; Goldoni, A. *Surface Science* **2003**, *532*, 892-897.

(180) Goldoni, A.; Cepek, C.; Larciprete, R.; Sangaletti, L.; Pagliara, S.; Floreano, L.; Gotter, R.; Verdini, A.; Morgante, A.; Luo, Y.; Nyberg, M. *Journal of Chemical Physics* **2002**, *116*, 7685-7690.

(181) Perdigao, L. M. A.; Saywell, A.; Fontes, G. N.; Staniec, P. A.; Goretzki, G.; Phillips, A. G.; Champness, N. R.; Beton, P. H. *Chemistry-a European Journal* **2008**, *14*, 7600-7607.

(182) Silly, F.; Shaw, A. Q.; Porfyrakis, K.; Briggs, G. A. D.; Castell, M. R. *Applied Physics Letters* **2007**, *91*.

(183) Mintova, S.; Bein, T. *Microporous and Mesoporous Materials* **2001**, *50*, 159-166.

(184) Liu, X.; Zhan, Y.; Braun, S.; Li, F.; Fahlman, M. *Physical Review B* **2009**, *80*.

(185) Textor, M.; Ruiz, L.; Hofer, R.; Rossi, A.; Feldman, K.; Hahner, G.; Spencer, N. D. *Langmuir* **2000**, *16*, 3257-3271.

(186) Tromp, R. M.; Hamers, R. J.; Demuth, J. E. *Physical Review B* **1986**, *34*, 1388-1391.

(187) Hamers, R. J.; Tromp, R. M.; Demuth, J. E. *Physical Review B* **1986**, *34*, 5343-5357.

(188) Feenstra, R. M.; Stroscio, J. A. *Physical Review Letters* **1987**, *59*, 2173-2176.

(189) Schofield, S. R.; Saraireh, S. A.; Smith, P. V.; Radny, M. W.; King, B. V. *Journal of the American Chemical Society* **2007**, *129*, 11402-11407.

(190) Lei, S. B.; De Feyter, S. In *Stm and Afm Studies On* 2008; Vol. 285, p 269-312.

(191) Kera, S.; Okudaira, K. K.; Harada, Y.; Ueno, N. *Japanese Journal of Applied Physics Part 1-Regular Papers Short Notes & Review Papers* **2001**, *40*, 783-787.

(192) Gopakumar, T. G.; Meiss, J.; Pouladsaz, D.; Hietschold, M. *Journal of Physical Chemistry C* **2008**, *112*, 2529-2537.

(193) Kong, X. H.; Wang, M.; Lei, S. B.; Yang, Y. L.; Wang, C. *Journal of Materials Chemistry* **2006**, *16*, 4265-4269.

(194) Tada, H.; Touda, H.; Takada, M.; Matsushige, K. *Applied Physics Letters* **2000**, *76*, 873-875.

(195) Hunter, C. A.; Meah, M. N.; Sanders, J. K. M. *Journal of the American Chemical Society* **1990**, *112*, 5773-5780.

(196) Moon, H.; Jahng, W. S.; Curtis, M. D. *Journal of Materials Chemistry* **2008**, *18*, 4856-4863.

(197) Anthony, J. E. *Angewandte Chemie-International Edition* **2008**, *47*, 452-483.

(198) Alvarado, S. F.; Seidler, P. F.; Lidzey, D. G.; Bradley, D. D. C. *Physical Review Letters* **1998**, *81*, 1082-1085.

(199) Dougherty, D. B.; Jin, W.; Cullen, W. G.; Dutton, G.; Reutt-Robey, J. E.; Robey, S. W. *Physical Review B* **2008**, *77*.

(200) Kemerink, M.; Alvarado, S. F.; Muller, P.; Koenraad, P. M.; Salemink, H. W. M.; Wolter, J. H.; Janssen, R. A. J. *Physical Review B* **2004**, *70*.

(201) Baran, J. D.; Larsson, J. A.; Woolley, R. A. J.; Cong, Y.; Moriarty, P. J.; Cafolla, A. A.; Schulte, K.; Dhanak, V. R. *Physical Review B*, *81*.

(202) Li, H. I.; Pussi, K.; Hanna, K. J.; Wang, L. L.; Johnson, D. D.; Cheng, H. P.; Shin, H.; Curtarolo, S.; Moritz, W.; Smerdon, J. A.; McGrath, R.; Diehl, R. D. *Physical Review Letters* **2009**, *103*.

(203) Torrente, I. F.; Franke, K. J.; Pascual, J. I. *Journal of Physics-Condensed Matter* **2008**, *20*.

(204) Veenstra, S. C.; Heeres, A.; Hadziioannou, G.; Sawatzky, G. A.; Jonkman, H. T. *Applied Physics a-Materials Science & Processing* **2002**, *75*, 661-666.

(205) Wang, L. L.; Cheng, H. P. *Physical Review B* **2007**, *75*.

(206) Zerweck, U.; Loppacher, C.; Otto, T.; Grafstrom, S.; Eng, L. M. *Nanotechnology* **2007**, *18*.

(207) M. S. Dresselhaus, G. D., and P.C. Ecklund *Science of fullerenes and Carbon Nanotubes* Academic: San Diego, 1996.

(208) Wang, Y.; Alcami, M.; Martin, F. *Chemphyschem* **2008**, *9*, 1030-1035.

(209) Ecija, D.; Otero, R.; Sanchez, L.; Gallego, J. M.; Wang, Y.; Alcami, M.; Martin, F.; Martin, N.; Miranda, R. *Angewandte Chemie-International Edition* **2007**, *46*, 7874-7877.

(210) Oison, V.; Koudia, M.; Abel, M.; Porte, L. *Physical Review B* **2007**, *75*.

(211) Amsalem, P.; Giovanelli, L.; Themlin, J. M.; Koudia, M.; Abel, M.; Oison, V.; Ksari, Y.; Mossoyan, M.; Porte, L. *Surface Science* **2007**, *601*, 4185-4188.

(212) Stiufiuc, R.; Perdigao, L. M. A.; Grandidier, B.; Deresmes, D.; Allan, G.; Delerue, C.; Stievenard, D.; Beton, P. H.; Erwin, S. C.; Sassi, M.; Oison, V.; Debierre, J. M. *Physical Review B*, *81*.

(213) Zaitsev, N. L.; Nechaev, I. A.; Chulkov, E. V. *Journal of Experimental and Theoretical Physics*, *110*, 114-120.

(214) Temirov, R.; Soubatch, S.; Luican, A.; Tautz, F. S. *Nature* **2006**, *444*, 350-353.